

Acceleration of Subtractive Non-contrast-enhanced Magnetic Resonance Angiography



Hao Li

Emmanuel College

Department of Radiology

University of Cambridge

This thesis is submitted for the degree of Doctor of Philosophy

January 2020

Declaration

This thesis is the result of my own work and includes nothing which is the outcome of work done in collaboration except as declared in the Preface and specified in the text. It is not substantially the same as any that I have submitted, or, is being concurrently submitted for a degree or diploma or other qualification at the University of Cambridge or any other University or similar institution except as declared in the Preface and specified in the text. I further state that no substantial part of my thesis has already been submitted, or, is being concurrently submitted for any such degree, diploma or other qualification at the University of Cambridge or any other University or similar institution except as declared in the Preface and specified in the text. It does not exceed the prescribed word limit for the relevant Degree Committee.

Acknowledgement

First and foremost, I would like to express my sincere appreciation to my supervisors, Professor David J Lomas and Dr. Andrew N Priest, for their knowledge, support and generosity in giving me the opportunity to carry out this research.

Professor Lomas first offered me the opportunity to start this PhD journey in Cambridge and provided me guidance in my research. His insightful comments helped me throughout the duration of my research and writing of this thesis. With his support, I have been able to concentrate on my PhD and present my work at conferences.

I am extremely grateful to Dr. Priest for providing me tremendous help during my PhD period. He helped me solve so many unexpected problems in my experiments and answered all my questions with his excellent expertise and great patience. He encouraged and guided me to be professional and do the right thing in challenging times. This work would not have been possible without his support. I am truly fortunate to gain the experience and guidance from him during the past three years and the coming two years.

I would like to express my appreciation to Dr. Martin J Graves for providing me with much valuable advice in my research and paper writings. I would also like to thank Dr. Ferdia A Gallagher for his support, and I am fortunate to continue working with him as a research associate for the next two years.

I would like to extend my appreciation to all the current and past members of the Department of Radiology at Cambridge. It has been my great pleasure to work with you during my PhD study.

In particular, I would like to thank Shuo Wang for his expertise in image analysis and mathematics, especially relating to Chapter 4 of this thesis. We had many pleasant collaborations and enlightening discussions.

I would like to acknowledge Nadeem Shaida and Akash Prashar for performing the subjective assessment in the studies of Chapters 6 and 7. Also, thanks to Nadeem for reviewing all the images from my volunteer examinations for the governance reporting.

Thanks to Ilse Patterson and Fulvio Zaccagna for doing consent for my volunteers. I am grateful for Ilse and the other radiographers at the MRIS unit for their help in accommodating my requests for scans.

Thanks to Leonardo Rundo for his valuable suggestions in my thesis. We have worked together over many late nights and forged a good friendship. Thanks to Yuan Huang for his expertise in statistics. Thanks to Lorena Escudero-Sanchez for her kind encouragement during my thesis writing period. Thanks to the support staff of the department for providing excellent administration and coordination.

I would like to express my special thanks to all the 29 volunteers involved in my studies. I know your time is valuable and lying in the scanner for one hour without any movement is not a pleasant experience. Your generous help is much appreciated.

I would like to show my gratitude to Ziwu Zhou from UCLA, who provided me the original Split Bregman reconstruction code and important help in developing the reconstruction algorithm in Chapter 6. I would also like to acknowledge Michael W. Weiner (UCSF) for providing the Poisson-disk pattern generation code, Tao Zhang (Stanford University) for providing the coil compression code, Ricardo Otazo (New York University) for providing the channel combination code, and Michael Lustig (UC Berkeley) for providing the L1-SPIRiT code and the BART toolbox.

I would like to acknowledge the China Scholarship Council and Cambridge Trust for funding my PhD. I am thankful to Emmanuel College for providing excellent daily life supports.

I would like to offer my special appreciation to my best friends at Cambridge, particularly my lovely housemates: Guandong Bai, Jun Ma, Xiaoxiao Sun, Fan Yang and Yunjia Zhang. Because of you, the life in our “Yingtao Tun” family was always full of happiness and laughter. Thanks to Yingfeng Ji, Hanjing Kong, Tony Fu and many other friends for always being there, sharing my joy and sorrow and giving me support during my hard times. Thanks to all of you for making so many ordinary moments extraordinary. You are the biggest treasure I have received at Cambridge.

The last words go to my parents. I always knew that you believed in me and wanted the best for me, and I want to thank you for your unconditional support. I also feel sorry for being absent for so long in the past three years, missing a few important festivals, which I will compensate in my future.

Abstract

Although contrast-enhanced magnetic resonance angiography (CE-MRA) is widely established as a clinical examination for the diagnosis of human vascular diseases, non-contrast-enhanced MRA (NCE-MRA) techniques have drawn increasing attention in recent years. NCE-MRA is based on the intrinsic physical properties of blood and does not require the injection of any exogenous contrast agents. Subtractive NCE-MRA is a class of techniques that acquires two image sets with different vascular signal intensity, which are later subtracted to generate angiograms.

The long acquisition time is an important drawback of NCE-MRA techniques, which not only limits the clinical acceptance of these techniques but also renders them sensitive to artefacts from patient motion. Another problem for subtractive NCE-MRA is the unwanted residual background signal caused by different static background signal levels on the two raw image sets. This thesis aims at improving subtractive NCE-MRA techniques by addressing both these limitations, with a particular focus on three-dimensional (3D) femoral artery fresh blood imaging (FBI).

The structure of the thesis is as follows:

Chapter 1 describes the anatomy and physiology of the vascular system, including the characteristics of arteries and veins, and the MR properties and flow characteristics of blood. These characteristics are the foundation of NCE-MRA technique development.

Chapter 2 introduces commonly used diagnostic angiographic methods, particularly CE-MRA and NCE-MRA. Current NCE-MRA techniques are reviewed and categorised into different types. Their principles, implementations and limitations are summarised.

Chapter 3 describes imaging acceleration theories including compressed sensing (CS), parallel imaging (PI) and partial Fourier (PF). The Split Bregman algorithm is described as an efficient CS reconstruction method. The SPIRiT reconstruction for PI and homodyne detection for PF are also introduced and combined with Split Bregman to form the basis of the reconstruction strategy for undersampled MR datasets. Four image quality metrics are presented for evaluating the quality of reconstructed images.

In Chapter 4, an intensity correction method is proposed to improve background suppression for subtractive NCE-MRA techniques. Residual signals of background tissues are removed by

performing a weighted subtraction, in which the weighting factor is obtained by a robust regression method. Image sparsity can also be increased and thereby potentially benefit CS reconstruction in the following chapters.

Chapter 5 investigates the optimal k -space sampling patterns for the 3D accelerated femoral artery FBI sequence. A variable density Poisson-disk with a fully sampled centre region and missing partial Fourier fractions is employed for k -space undersampling in the k_y - k_z plane. Several key parameters in sampling pattern design, such as partial Fourier sampling ratios, fully sampled centre region size and density decay factor, are evaluated and optimised.

Chapter 6 introduces several reconstruction strategies for accelerated subtractive NCE-MRA. A new reconstruction method, k -space subtraction with phase and intensity correction (KSPIC), is developed. By performing subtraction in k -space, KSPIC can exploit the sparsity of subtracted angiogram data and potentially improve the reconstruction performance. A phase correction procedure is used to restore the polarity of negative signals caused by subtraction. The intensity correction method proposed in Chapter 4 is also incorporated in KSPIC as it improves background suppression and thereby sparsity.

The highly accelerated technique can be used not only to reduce the acquisition time, but also to enable imaging with increased resolution with no time penalty. A time-efficient high-resolution FBI technique is proposed in Chapter 7. By employing KSPIC and modifying the flow-compensation/spoiled gradients, the image matrix size can be increased from 256×256 to up to 512×512 without prolonging the acquisition time.

Chapter 8 summarises the overall achievements and limitations of this thesis, as well as outlines potential future research directions.

Contents

| | |
|--|-----------|
| Chapter 1. Vascular anatomy and physiology | 1 |
| 1.1 Anatomy of the vascular system..... | 1 |
| 1.2 Physiology of circulation | 3 |
| 1.2.1 Composition and MR properties of blood | 3 |
| 1.2.2 Blood flow | 4 |
| 1.2.3 Peripheral arterial disease..... | 7 |
| 1.3 Summary | 7 |
| Chapter 2. Angiography techniques | 9 |
| 2.1 Vascular imaging techniques..... | 9 |
| 2.2 CE-MRA versus NCE-MRA..... | 12 |
| 2.2.1 CE-MRA..... | 12 |
| 2.2.2 Renaissance of NCE-MRA..... | 15 |
| 2.3 Review of NCE-MRA techniques | 16 |
| 2.3.1 Inflow-based techniques..... | 16 |
| 2.3.2 Techniques based on flow within the imaging volume..... | 19 |
| 2.3.3 Flow-independent NCE-MRA..... | 24 |
| 2.3.4 Limitations of NCE-MRA techniques..... | 24 |
| 2.4 Fresh blood imaging | 26 |
| 2.4.1 Conventional FBI..... | 27 |
| 2.4.2 FBI with flow-spoiled gradient pulses | 28 |
| 2.4.3 FBI with variable flip angles | 28 |
| 2.4.4 Applications..... | 29 |
| 2.5 Summary | 29 |
| Chapter 3. Acceleration theory and compressed sensing reconstruction algorithm..... | 31 |
| 3.1 Overview of MRI acceleration | 31 |
| 3.1.1 MRI speed..... | 31 |

| | |
|--|-----------|
| 3.1.2 Efforts in MRI acceleration | 31 |
| 3.1.3 Acceleration for NCE-MRA..... | 32 |
| 3.2 Compressed sensing..... | 33 |
| 3.2.1 Basic idea of compressed sensing..... | 33 |
| 3.2.2 Requirements of compressed sensing | 34 |
| 3.2.3 Problem formulation of compressed sensing..... | 36 |
| 3.3 Split Bregman algorithm..... | 38 |
| 3.3.1 Bregman iteration..... | 38 |
| 3.3.2 Split Bregman | 40 |
| 3.4 Parallel imaging and partial Fourier sampling | 42 |
| 3.4.1 Parallel imaging | 42 |
| 3.4.2 SPIRiT | 43 |
| 3.4.3 L1-SPIRiT | 44 |
| 3.4.4 Partial Fourier sampling | 47 |
| 3.5 Quantitative evaluation metrics | 48 |
| 3.5.1 PSNR..... | 49 |
| 3.5.2 SSIM..... | 49 |
| 3.5.3 CNR of artery-to-background..... | 50 |
| 3.5.4 Sharpness | 52 |
| 3.6 Summary | 54 |
| Chapter 4. Improved background suppression using robust regression based weighted subtraction | 56 |
| 4.1 Introduction | 56 |
| 4.2 Theory | 57 |
| 4.2.1 Characteristics of residual signal | 57 |
| 4.2.2 Robust regression..... | 61 |
| 4.2.3 Weight function | 62 |

| | |
|--|-----------|
| 4.3 Methods..... | 66 |
| 4.3.1 Study population and imaging protocols..... | 66 |
| 4.3.2 Model parameters..... | 66 |
| 4.3.3 Image assessment..... | 67 |
| 4.4 Results..... | 71 |
| 4.4.1 Signal level of static tissues on BBIs and DBIs..... | 71 |
| 4.4.2 Example images..... | 71 |
| 4.4.3 Quantitative analysis..... | 73 |
| 4.5 Discussion..... | 76 |
| 4.6 Conclusion..... | 79 |
| Chapter 5. Optimisation of Poisson-disk sampling pattern for highly accelerated femoral NCE-MRA | 80 |
| 5.1 Introduction..... | 80 |
| 5.2 Sampling Pattern Design for 3D Accelerated MRI..... | 80 |
| 5.2.1 Requirements of PI, PF and CS..... | 80 |
| 5.2.2 Variable density Poisson-disk..... | 81 |
| 5.3 Optimisation of Sampling Pattern Parameters..... | 82 |
| 1.1.1 Density decay factor..... | 83 |
| 5.3.2 Fully sampled central region..... | 83 |
| 5.3.3 Partial Fourier ratio(s)..... | 83 |
| 5.4 Methods..... | 83 |
| 5.4.1 Data acquisition..... | 83 |
| 5.4.2 Image assessment..... | 84 |
| 5.4.3 Pattern optimisation..... | 84 |
| 5.5 Results..... | 85 |
| 5.5.1 Optimisation of density decay factor..... | 85 |
| 5.5.2 Optimisation of fully sampled central region size..... | 86 |

| | |
|--|-----------|
| 5.5.3 Optimisation of fully sampled central region shape | 87 |
| 5.5.4 Optimisation of PF ratio in the k_y dimension..... | 88 |
| 5.5.5 Optimisation of PF ratio in the k_z dimension..... | 89 |
| 5.5.6 Summary of optimised parameters | 89 |
| 5.5.7 Comparison of optimised patterns and non-optimised patterns | 90 |
| 5.6 Discussion | 93 |
| 5.7 Conclusion..... | 95 |
| Chapter 6. Reconstruction for highly accelerated subtractive NCE-MRA using k-space subtraction with phase and intensity correction | 96 |
| 6.1 Introduction | 96 |
| 6.2 Reconstruction strategies for subtractive NCE-MRA..... | 98 |
| 6.2.1 Independent reconstruction with magnitude subtraction afterwards (MS) | 98 |
| 6.2.2 K -space subtraction prior to reconstruction (KS) | 98 |
| 6.2.3 Combined reconstruction with magnitude subtraction (CMS)..... | 98 |
| 6.2.4 K -space subtraction with phase correction (KSPC)..... | 99 |
| 6.2.5 K -space subtraction with phase and intensity correction (KSPIC)..... | 100 |
| 6.2.6 Summary of reconstruction strategies | 101 |
| 6.3 Methods..... | 102 |
| 6.3.1 Subjects and imaging protocols | 102 |
| 6.3.2 CS reconstruction..... | 103 |
| 6.3.3 Coil compression and coil combination | 103 |
| 6.3.4 Central region of k -space..... | 104 |
| 6.3.5 Image assessment..... | 104 |
| 6.3.6 Statistics analysis | 106 |
| 6.4 Results | 108 |
| 6.4.1 Retrospective simulation | 108 |
| 6.4.2 Prospective acquisition..... | 113 |

| | |
|--|------------|
| 6.4.3 Phase correction | 117 |
| 6.4.4 Coil compression and coil combination | 121 |
| 6.4.5 Fast partial reconstruction and iteration numbers | 122 |
| 6.5 Discussion | 123 |
| 6.6 Conclusion | 125 |
| Chapter 7. High-resolution fresh blood imaging with compressed sensing..... | 127 |
| 7.1 Introduction | 127 |
| 7.2 Method | 128 |
| 7.2.1 Sequence design of high-resolution FBI | 128 |
| 7.2.2 Subjects and imaging protocols | 130 |
| 7.2.3 Image evaluation..... | 131 |
| 7.3 Results | 132 |
| 7.3.1 Example images | 132 |
| 7.3.2 Quantitative evaluation..... | 134 |
| 7.3.3 Effect of flow-compensation/spoiled gradients | 135 |
| 7.3.4 Effect of z-spoiler..... | 136 |
| 7.4 Discussion | 137 |
| 7.5 Conclusion..... | 139 |
| Chapter 8. Final remarks and future work | 140 |
| 8.1 Summary | 140 |
| 8.2 Limitations and future work | 141 |
| 8.2.1 Patient examinations | 141 |
| 8.2.2 Application in other body areas | 141 |
| 8.2.3 Application in other subtractive imaging techniques..... | 143 |
| 8.2.4 Future direction of CS | 143 |
| 8.2.5 Future direction of FBI..... | 144 |
| 8.3 Conclusion..... | 144 |

List of Figures

| | |
|---|----|
| Figure 1.1 The main arteries (A) and veins (B) in the human circulatory system. | 1 |
| Figure 1.2 Typical velocity waveforms of popliteal arteries and carotid arteries, and the time relationship between the ECG R wave and waveforms..... | 6 |
| Figure 1.3 The velocity waveforms of calf arteries from two patients with stenosis (A) and occlusion (B) in one leg. | 7 |
| Figure 2.1 Typical images of carotid arteries obtained by (A) DSA, (B) ultrasonography, (C) CTA and (D) CE-MRA..... | 10 |
| Figure 2.2 CE angiograms acquired from a volunteer demonstrating the lower iliac and leg arteries..... | 14 |
| Figure 2.3 The mechanism of TOF effect is illustrated with a model containing an artery (red) and a vein (blue). | 17 |
| Figure 2.4 Example images of 2D TOF of carotid arteries (A) and 3D TOF of intracranial arteries (axial MIP) (B)..... | 18 |
| Figure 2.5 Spin-phase effects on moving (red curve) and stationary (blue curve) spins under a pair of bipolar gradients..... | 20 |
| Figure 2.6 Schematic diagram of FSD pulse sequence..... | 22 |
| Figure 2.7 Example FSD images of lower legs..... | 23 |
| Figure 2.8 (a) Sequence diagram of ECG-synchronised 3D half-Fourier FSE..... | 27 |
| Figure 2.9 Sequence diagram of FBI using the original readout gradients (a) and flow-spoiled gradients (b). | 28 |
| Figure 3.1 A heuristic procedure of incoherent sampling and CS reconstruction..... | 34 |
| Figure 3.2 Typical MRI sampling patterns. | 36 |
| Figure 3.3 Compressed sensing sampling process with the undersampling matrix R and the Fourier transform F | 36 |
| Figure 3.4 Compressed sensing sampling process with the undersampling matrix R , the Fourier transform F and a sparsifying transform Φ | 37 |
| Figure 3.5 The Bregman distance associated with a convex function $J \cdot$ between the point u and v . $p \in \partial J(v)$ is the sub-gradient of $J \cdot$ at v | 39 |

| | |
|---|----|
| Figure 3.6 Flow chart summarizing the process of the homodyne algorithm for partial Fourier sampling reconstruction. | 48 |
| Figure 3.7 Diagram of the process of mask generation. | 51 |
| Figure 3.8 Flow chart of the sharpness evaluation process. | 53 |
| Figure 3.9 The sigmoid function for four different values of the sharpness parameter s | 54 |
| Figure 4.1 The scatter plot of the DBI and BBI SI for each pixel in one single slice (A) and the corresponding bright-artery (B) and dark-artery slice (C). | 57 |
| Figure 4.2 Two examples of thoracic 3D DANTE-bSSFP (A and B, both arteries and veins) and femoral 3D FBI (C and D, arteries only). | 59 |
| Figure 4.3 Weight maps of (A) OLS, (B) cRR, (C) RRDA and (D) improved RRDA ($\alpha=0.25$) when the current regression line is $y=x$ | 63 |
| Figure 4.4 Signal level of background tissues in BBIs and DBIs in thoracic FSD (A), iliac FSD (B) and femoral FBI (C). | 71 |
| Figure 4.5 Example MIPs and the corresponding scatter plot of thoracic 3D DANTE-bSSFP (A–E), iliac 3D iMSDE-FSE (F–J) and femoral 3D FBI (K–O). | 73 |
| Figure 4.6 Bland-Altman plots and boxplots comparing the regression results of OLS, cRR and RRDA. | 75 |
| Figure 4.7 Comparison of the tissue-to-artery/vein SI ratios between RRDA and direct subtraction in thoracic FSD (A), iliac FSD (B) and femoral FBI (C). | 76 |
| Figure 5.1 Typical sampling patterns in the k_y - k_z plane for 3D MRI acquisitions. | 81 |
| Figure 5.2 A typical Poisson-disk sampling pattern for 3D accelerated imaging combining PI, CS and PF. | 82 |
| Figure 5.3 Sampling patterns with varying density decay factor (10 \times) (A) and corresponding quantitative measurements with AFs of 6 \times , 10 \times and 14 \times (B). | 85 |
| Figure 5.4 Sampling patterns with varying sizes of the fully sampled central region (A) and corresponding quantitative measurements with AFs of 6 \times , 10 \times and 14 \times (B). | 86 |
| Figure 5.5 Sampling patterns with different shapes of fully sampled central region (varying ratios of length to width) (10 \times) (A) and corresponding quantitative measurements with AFs of 6 \times , 10 \times and 14 \times (B). | 87 |

| | |
|--|-----|
| Figure 5.6 Sampling patterns with varying PF ratios in the k_y dimension (10x) (A) and corresponding quantitative measurements with AFs of 6x, 10x and 14x (B)..... | 88 |
| Figure 5.7 Sampling patterns with varying PF ratios in the k_z dimension (10x) (A) and corresponding quantitative measurements with AFs of 6x, 10x and 14x (B)..... | 89 |
| Figure 5.8 Optimised (A) and non-optimised (B) sampling patterns and the corresponding example MIPs (left leg) of reconstructed images (C and D) with different AFs..... | 91 |
| Figure 5.9 Quantitative evaluation results of accelerations using optimised patterns and non-optimised patterns with different AFs. | 92 |
| Figure 6.1 Flow charts of (A) the magnitude subtraction reconstruction process, (B) the k -space subtraction reconstruction process and (C) the combined magnitude subtraction reconstruction. | 99 |
| Figure 6.2 Flow charts of (A) the KSPIC reconstruction process and (B) the weighting factor calculation procedure..... | 101 |
| Figure 6.3 Plots summarising quantitative evaluation of simulated acceleration. | 109 |
| Figure 6.4 Example images of retrospective simulated accelerations using different reconstructions. | 112 |
| Figure 6.5 Example MIP images of prospectively accelerated acquisitions from two healthy volunteers using AFs of 10x and 25x with KS, MS, CMS-IC and KSPIC..... | 115 |
| Figure 6.6 Plots summarising subjective image quality scores (1–4 scales) in terms of vessel delineation, noise and artefacts, and background and venous contamination on the images prospectively accelerated by 10x, 15x, 20x and 25x..... | 115 |
| Figure 6.7 Example MIPs of reconstructions using k -space subtraction with phase correction (KSPC, panel A) and without phase correction (KS, panel C)..... | 117 |
| Figure 6.8 Quantitative evaluation of KSPIC reconstructions using the central region acquired from different data sources for (A) SPIRiT kernel calculation, (B) weights calculation in adaptive channel combination, and (C) background phase reference in phase correction. ... | 118 |
| Figure 6.9 An example of reconstructed images using phase reference from BB (A and C) and DB (B and D) data..... | 119 |
| Figure 6.10 Evaluation of the phase correction region size..... | 120 |

| | |
|---|-----|
| Figure 6.11 The quantitative evaluation results (A, B and C) and reconstruction time (D) of coil compression and coil image combination with different virtual channel numbers..... | 121 |
| Figure 6.12 Example images reconstructed by 3D FFT (A), fast CS (B) and full CS (C). ... | 122 |
| Figure 7.1 Diagrams of the 3D FBI sequence with the standard resolution (A) and increased high resolution (B)..... | 128 |
| Figure 7.2 The timing of the FID signal and its refocused echo (red) and the primary spin echo (blue) relative to the readout gradient..... | 129 |
| Figure 7.3 Example MIP images with different resolutions from two healthy volunteers... | 133 |
| Figure 7.4 Box-plots of the subjective quality scores of FBI images with different resolutions in terms of the large vessel delineations (A) and small vessel delineations (B). The matrix sizes are the same in the x and y dimensions, increasing from 256 to 512. * denotes statistical significance between the high-resolution images and the standard-resolution images (256×256). (Wilcoxon signed-rank tests, $P<0.05$). | 134 |
| Figure 7.5 Box-plots of objective evaluation results of FBI images with different resolutions in terms of sharpness (A) and CNR of artery-to-background (B)..... | 135 |
| Figure 7.6 Importance of flow-compensation gradients in high-resolution FBI..... | 136 |
| Figure 7.7 Artefacts on high-resolution unsubtracted single-slice source images (bright-artery) with a matrix size of 384×384×80..... | 137 |
| Figure 8.1 High resolution whole leg examination with two stations (matrix size: 352×352×80). | 142 |

List of Tables

| | |
|--|-----|
| Table 1.1 The comparison between system arteries and veins..... | 2 |
| Table 1.2 T_1 , T_2 , and T_2^* corrected for inhomogeneities of the static magnetic field (B_0) of arterial and venous blood at 1.5 Tesla and 23 °C..... | 4 |
| Table 1.3 Peak velocities of typical vessels | 5 |
| Table 2.1 Comparisons between different vascular imaging techniques..... | 11 |
| Table 3.1 A Split Bregman algorithm for the CS optimisation problem | 41 |
| Table 3.2 L1-SPIRiT reconstruction solved by Split Bregman and POCS..... | 46 |
| Table 4.1 The weight functions and characteristics of different regression methods | 65 |
| Table 4.2 Parameters used for thoracic FSD, iliac FSD and femoral FBI. | 69 |
| Table 4.3 Comparison of mean regression coefficients calculated by different regression methods versus the reference values. | 74 |
| Table 5.1 The optimal value ranges by AF for the sampling pattern design (matrix size: 224×224×80)..... | 90 |
| Table 5.2 The parameters by AF for optimised and non-optimised sampling patterns in Chapter 5 (matrix size: 224×224×80)..... | 93 |
| Table 6.1 Reconstruction methods included in this study..... | 101 |
| Table 6.2 Parameters used in retrospective and prospective studies. | 107 |
| Table 6.3 Quantitative analysis results (mean ± standard deviation) of KS, MS, CMS and KSPC. Images were retrospectively accelerated by 4×, 12× and 20× from 10 volunteer datasets. .. | 110 |
| Table 6.4 Quantitative analysis results (mean ± standard deviation) of MS-IC, CMS-IC and KSPIC. Images were retrospectively accelerated by 4×, 12× and 20× from 10 volunteer datasets. | 111 |
| Table 6.5 Subjective scores (mean ± standard deviation) of images prospectively accelerated by 10×, 15×, 20× and 25× from 10 volunteer datasets..... | 116 |
| Table 6.6 Comparison of mean intensity correction coefficients calculated based on images reconstructed by FFT, fast CS and full CS. | 123 |

List of Publications

Published Journal Articles:

1. **Hao Li**, Andrew Priest, Ilse Patterson, Martin J Graves, and David J Lomas, Subtractive Non-Contrast-Enhanced Magnetic Resonance Imaging of Lower Limb Veins using Multiple Flow-Dependent Preparation Strategies, *Magnetic Resonance in Medicine*, 2019;81:1769–1783.
2. Wenjian Huang, **Hao Li**, Rui Wang, Xiaodong Zhang, Xiaoying Wang, and Jue Zhang. A Self-Supervised Strategy for Fully Automatic Segmentation of Renal Dynamic Contrast-Enhanced Magnetic Resonance Images, *Medical Physics*, 2019, 46(10): 4417:4418.
3. Bo Li, **Hao Li**, and Li Dong. Quantitative Comparisons Between Relaxation Enhanced Compressed Sensing 3D MERGE and Conventional 3D MERGE for Vessel Wall Imaging in Equal Scan Time: Preliminary Studies, *Science China-Life Sciences* 2019: 1-9.

Papers in Progress:

1. **Hao Li**, Shuo Wang, Martin J Graves, David J Lomas and Andrew Priest. Subtractive NCE-MRA: Improved Background Suppression Using Robust Regression Based Weighted Subtraction, *Magnetic Resonance in Medicine*, under revision.
2. **Hao Li**, Martin J Graves, David J Lomas and Andrew Priest. Highly Accelerated Subtractive NCE-MRA using Advanced k -space Subtraction and Magnitude Subtraction Reconstruction Methods, *Magnetic Resonance in Medicine*, in preparation.
3. **Hao Li**, Martin J Graves, David J Lomas and Andrew Priest. Subtractive Peripheral NCE-MRA with Increased Spatial Resolution Using Compressed Sensing, in preparation.

Selected Conference Presentations:

1. **Hao Li**, Shuo Wang, Andrew Priest, Martin J Graves and David J Lomas., An Optimised Subtraction Approach for Subtractive NCE-MRA Techniques Based on Robust Regression using The Deviation Angle, SMRA, 2018 (**Best Presentation Award**).
2. **Hao Li**, Andrew Priest, Martin J Graves, and David J Lomas. Highly Accelerated NCE-MRA Using k -space Subtraction with Phase and Intensity Correction: Improved Reconstruction Accuracy and Background Suppression, SMRA, 2019 (**Oral Presentation**).
3. **Hao Li**, Andrew Priest, Martin J Graves, and David J Lomas. Highly Accelerated

Subtractive NCE-MRA using Advanced k-space Subtraction and Magnitude Subtraction Reconstruction Methods, ISMRM 2020 (**Oral Presentation**).

4. **Hao Li**, Andrew Priest, Martin J Graves, and David J Lomas. Optimisation of Poisson-disk Sampling Pattern for Highly Accelerated Femoral NCE-MRA, ISMRM 2020.
5. **Hao Li**, Shuo Wang, Andrew Priest, Martin J Graves and David J Lomas. Background Tissue Suppression for Subtractive NCE-MRA Techniques Based on Robust Regression Using the Deviation Angle, ISMRM 2019:7231.
6. **Hao Li**, Andrew Priest, Martin J Graves, and David J Lomas. Highly Accelerated NCE-MRA: Phase Correction to Remove Background Artefacts for Complex Subtraction, ISMRM 2019:3534.
7. **Hao Li**, Andrew Priest, Martin J Graves, and David J Lomas. Highly Accelerated NCE-MRA Using Complex Subtraction with Intensity Correction: Improved Reconstruction Accuracy and Background Tissue Suppression, ISMRM 2019:834.
8. **Hao Li**, Shuo Wang, Andrew Priest, Martin J Graves and David J Lomas., An Optimised Subtraction Approach for Subtractive NCE-MRA Techniques Based on Principal Component Analysis, ISMRM 2018: 922 (**Oral Presentation**).
9. **Hao Li**, Andrew Priest, Martin J Graves, and David J Lomas., Triple Accelerated NCE-MRA with Optimised Sampling Patterns, ISMRM 2018: 2983.

List of Abbreviations and Acronyms

| | |
|--------|--|
| 2D | Two-dimensional |
| 3D | Three-dimensional |
| ACS | Autocalibration signal |
| AF | Acceleration factor |
| ASL | Arterial spin labelling |
| BB | Bright-blood |
| BBIs | Bright-blood images |
| bSSFP | Balanced steady-state free precession |
| CE-MRA | Contrast-enhanced magnetic resonance angiography |
| CMS | Combined magnitude subtraction |
| CMS-IC | Combined magnitude subtraction with intensity correction |
| CNR | Contrast-to-noise ratio |
| cRR | Conventional robust regression |
| CTA | Computed tomography angiography |
| DANTE | Delay alternating with nutation for tailored excitation |
| DB | Dark-blood |
| DBIs | Dark-blood images |
| DIR | Dual inversion-recovery |
| DSA | Digital subtraction angiography |
| ECG | Electrocardiograph |
| EPI | Echo-planar imaging |
| ETL | Echo train length |
| FBI | Fresh blood imaging |
| FID | Free induction decay |
| FLASH | Fast low angle shot |
| FOV | Field-of-view |
| FSD | Flow-sensitive dephasing |
| FSE | Fast spin-echo |
| GBCAs | Gadolinium-based contrast agents |
| Gd | Gadolinium |
| IFIR | Inflow inversion-recovery |

| | |
|---------|--|
| iMSDE | Improved motion-sensitised driven-equilibrium |
| IRLS | Iteratively reweighted least squares |
| KS | Conventional k -space subtraction |
| KSPC | K -space subtraction with phase correction |
| KSPIC | K -space subtraction with phase and intensity correction |
| MIP | Maximum intensity projection |
| MRA | Magnetic resonance angiography |
| MRI | Magnetic resonance imaging |
| MS | Conventional magnitude subtraction |
| ms | millisecond |
| MSDE | Motion-sensitised driven-equilibrium |
| MS-IC | Conventional magnitude subtraction with intensity correction |
| NCE-MRA | Non-contrast-enhanced magnetic resonance angiography |
| NMSE | Normalised mean square error |
| OLS | Ordinary least-squares regression |
| PAD | Peripheral arterial disease |
| PC | Phase-contrast |
| PCA | Principal component analysis |
| PF | Partial Fourier |
| PI | Parallel imaging |
| POCS | Projection over convex sets |
| PSNR | Peak signal-to-noise ratio |
| PVD | Peripheral vascular disease |
| QI | Quiescent interval |
| QISS | Quiescent inflow slice-selective |
| RF | Radio-frequency |
| RMSE | Root mean square error |
| RRDA | Robust regression based on deviation angle |
| RSS | Root-sum-of-squares |
| SPiRiT | Iterative self-consistent parallel imaging reconstruction |
| SSIM | Structural similarity |
| STIR | Spatially nonselective short-time inversion recovery |
| TE | Echo time |

| | |
|-----|--------------------|
| TI | Inversion time |
| TOF | Time-of-flight |
| TR | Repetition time |
| TV | Total variation |
| VS | Velocity-selective |

Chapter 1. Vascular anatomy and physiology

This chapter describes the anatomy and physiology of the vascular system, which is the foundation of MR angiography technique development.

1.1 Anatomy of the vascular system

Blood vessels are the channels or conduits through which blood is transported to body tissues. The vessels make up two circulatory systems that begin and end at the heart. One of them is the pulmonary circulation, which is a short loop that transports deoxygenated blood from the heart to the lungs and returns oxygenated blood back to the heart. The other is the systemic circulation, which carries blood from the heart to all the other body tissues and back again. Based on their structure and function, blood vessels can be classified as arteries, capillaries and veins.

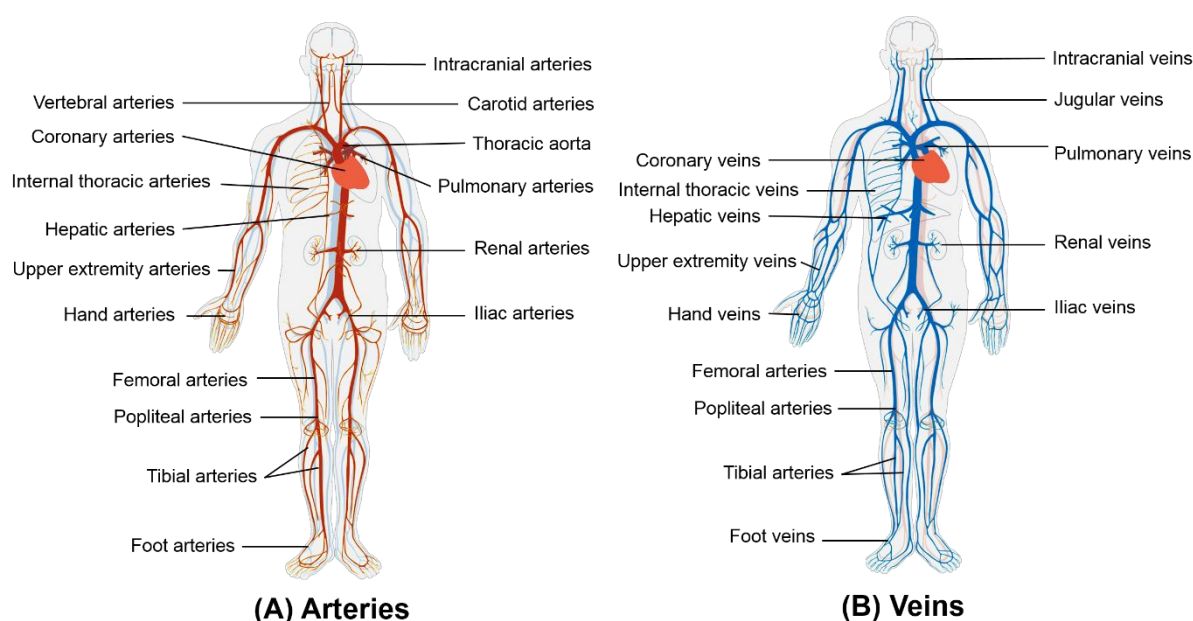


Figure 1.1 The main arteries (A) and veins (B) in the human circulatory system. (Reproduced from Wikipedia: <https://en.wikipedia.org/wiki/Artery> and <https://en.wikipedia.org/wiki/Vein>)

Arteries carry blood away from the heart and distribute it to the body (Fig. 1.1A). Systemic arteries carry blood from the heart to other parts of the body, while pulmonary arteries deliver deoxygenated blood to the lungs. Blood is pumped from the ventricles into large elastic arteries and then travels into smaller arteries called arterioles. Arterioles help regulate the blood pressure by the contraction of the vascular smooth muscle, and deliver blood to the capillaries.

The lower extremity arteries are the primary region of interest for this thesis. After emerging from the aorta, the common iliac arteries bifurcate into the internal and external iliac arteries, and the external iliac arteries lead into the femoral arteries. The femoral arteries extend and eventually become the popliteal arteries, which then bifurcate into the anterior and posterior tibial arteries, supplying the leg and foot with blood.

Veins return blood from the capillary beds to the heart (Fig. 1.1B). The blood enters venules, the smallest veins, after passing through the capillaries. Then, it flows into larger and larger veins progressively, and eventually reaches the heart. Systemic veins carry blood from body tissues to the right atrium. This blood has a reduced oxygen level because the oxygen has been consumed during the metabolic activities in the tissue cells. In contrast, the pulmonary veins transport well-oxygenated blood from the lungs to the heart.

The artery wall consists of three layers. The outermost layer, the tunica externa, attaches the vessel to the surrounding tissue. Inside the tunica externa is the tunica media, which is made up of smooth muscle cells and elastic tissue. It provides support for the vessel and also helps to regulate blood flow and blood pressure by the ability to change diameter. The innermost layer, in direct contact with the blood flow, is the tunica intima. The walls of veins have a similar structure but have less smooth muscle and connective tissue, which makes them thinner and less rigid than arterial walls. Because of this, veins can hold more blood than arteries, and their volume varies considerably with hydration status. Venous valves, which are similar to the semilunar valves in the heart, exist in medium and large veins and help keep the blood flowing towards the heart.

Capillaries are the smallest and most numerous blood vessels. They connect arterioles and venules, and make up the microcirculation. The primary function of capillaries is to exchange water, oxygen, carbon dioxide, and other nutrients and waste products between the blood and tissue cells. Capillary distribution varies with the metabolic activity of different tissues. The metabolically active tissues such as kidney, liver and skeletal muscle have extensive capillary networks because they require an abundant supply of nutrients and oxygen. Other less active tissues, such as the connective tissue, have a less abundant supply of capillaries.

Table 1.1 summarises the differences between arteries and veins. These differences reflect the basic characteristics of arteries and veins and determine the suitable types of imaging techniques for them.

Table 1.1 The comparison between system arteries and veins

| | Arteries | Veins |
|-------------------------|--|---|
| Direction of blood flow | From the heart to various parts of the body | From various parts of the body to the heart |
| Flow speed and pattern | Fast and pulsatile | Peripherally slow, almost constant; Can be pulsatile or intermittent |
| Pressure | Higher blood pressure | Lower blood pressure |
| Location | Deeper in the body | Superficial and deep in the body |
| Oxygen concentration | Oxygenated blood (with the exception of the pulmonary artery and umbilical artery). | Deoxygenated blood (with the exception of pulmonary veins and umbilical vein). |
| Anatomy layer | Thick, elastic muscle layer that can handle high pressure of the blood flowing through the arteries. | Thin, elastic muscle layer with semilunar valves that prevent the blood from flowing in the opposite direction. |
| Size and volume | Fixed shape, less deformable | Variable size, more deformable |
| Lumen | Narrow, typically circular in cross-section | Wide, may vary widely in cross-sectional shape |
| Valves | No | Yes |

1.2 Physiology of circulation

1.2.1 Composition and MR properties of blood

Blood is composed of blood cells suspended in plasma. Plasma is over 95% water with some proteins, inorganic ions and organic substances. The primary blood cells are erythrocytes (red blood cells). Erythrocytes contain haemoglobin, which is an iron-containing protein that transports oxygen around the body. Haemoglobin can be saturated with oxygen molecules (oxyhaemoglobin) or desaturated with oxygen molecules (deoxyhaemoglobin). Oxyhaemoglobin is weakly diamagnetic as the iron atom has no unpaired electrons. Deoxyhaemoglobin has four unpaired electrons per iron atom and is strongly paramagnetic. In arterial blood, over 95% of haemoglobin is in the oxyhaemoglobin state, while venous blood

contains less oxyhaemoglobin (around 70% but varies depending on body region and metabolic activity in relation to blood flow).

The T_1 and T_2 relaxation times of blood are longer than most biological tissues but smaller than water. Arterial and venous blood have similar T_1 values, but arterial blood has a larger T_2 value as it has a higher ratio of oxyhaemoglobin compared with venous blood. The exact values depend on haematocrit level, oxygenation and temperature. Table 1.2 summarises the values of T_1 , T_2 and T_2^* (corrected for inhomogeneities of the static magnetic B_0 field) values of arterial and venous blood measured at a magnetic field strength of 1.5 Tesla and a temperatures of 23 °C¹. The relaxation characteristics of blood can be used as a source of contrast mechanisms in flow-independent non-contrast-enhanced magnetic resonance angiography (NCE-MRA) techniques, which will be described in Chapter 2.

Table 1.2 T_1 , T_2 , and T_2^* corrected for inhomogeneities of the static magnetic field (B_0) of arterial and venous blood at 1.5 Tesla and 23 °C

| | T_1 | T_2 | Corrected T_2^* |
|----------------|------------------|-----------------|-------------------|
| Arterial blood | 1435 ± 48 ms | 254 ± 26 ms | 254 ± 32 ms |
| Venous blood | 1434 ± 53 ms | 181 ± 23 ms | 42 ± 2.8 ms |

1.2.2 Blood flow

The flow characteristics of blood are another source of contrast for NCE-MRA techniques. The velocity and the appearance of the velocity waveform is a crucial factor in the design of the flow-based NCE-MRA techniques.

Like all fluids, blood flows from a region with high pressure to a lower pressure area, which means from arteries to capillaries to veins. Arteries experience high pressure values and large variations over the cardiac cycle as they experience the direct action of the beating heart². Very little pressure remains by the time blood leaves the capillaries and enters the venules. Blood flow through the veins is not the direct result of ventricular contraction. Instead, venous return can depend on skeletal muscle contraction, respiratory movements, and constriction of smooth muscle in venous walls. Peak flow velocities of typical vessels in different body areas are shown in Table 1.3.

Table 1.3 Peak velocities of typical vessels

| Vessel | Peak velocity (cm/sec) |
|------------------------------------|------------------------|
| Thoracic aorta | 150–175 |
| Abdominal aorta and iliac arteries | 100–150 |
| Femoral artery | 80–110 |
| Popliteal artery | 45–80 |
| Intracranial arteries | 30–70 |
| Vena cava | 10–45 |
| Large veins | 10–20 |

The blood flow is pulsatile in most arteries and some veins close to the heart. The appearance of the velocity waveform of an artery depends on vessel wall compliance and flow resistance³. For lower extremity arteries, the high-resistance muscle beds lead to a triphasic appearance of their velocity waveforms shown as Figure 1.2. The profile includes a period of flow reversal, and the diastolic flow is relatively stationary. In contrast, carotid arteries have relatively higher diastolic flow because of the low resistance of the organ they perfuse.

The electrocardiograph (ECG) in Figure 1.2 shows the electrical events taking place in the heart. The P-wave represents atrial depolarisation, the QRS complex represents ventricular depolarisation, and the T-wave represents ventricular repolarisation. In MRI, ECG activity is used to provide a gating or triggering mechanism for synchronisation of the imaging acquisition to the cardiac cycle. Peak systolic flow in arteries typically occurs 150–200 milliseconds following the R wave of ECG tracings. The delay between ventricular contraction and peak systolic flow increases as the pulse wave moves distally toward the extremities^{4,5}.

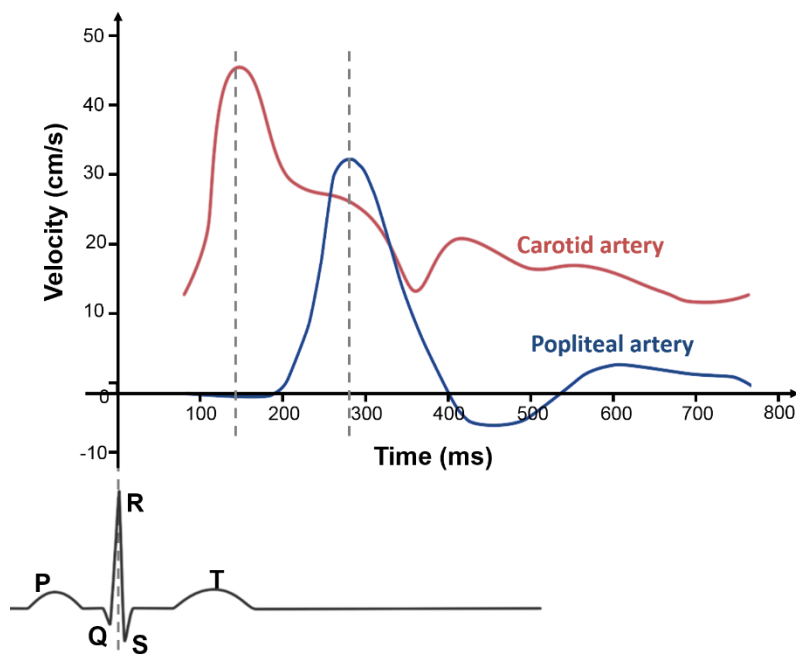


Figure 1.2 Typical velocity waveforms of popliteal arteries and carotid arteries, and the time relationship between the ECG R wave and waveforms. The waveform of femoral arteries demonstrates a typical triphasic profile including a period of flow reversal, while the carotid arterial flow waveform is elevated from the baseline. The delay between peak flow and the R wave for popliteal arteries is longer than that for carotid arteries.

Vascular diseases can lead to disruption of the pulsatile pattern. In diabetic patients with calcified, attenuated, or stenotic vessels, the triphasic appearance can be dampened and become monophasic with a stretched systolic flow pattern^{5,6}. Blood flow in arteries with narrow lumens, together with flow pulsatility, can also result in the periodic generation of complex fast flow and turbulence⁷. Flow may also be substantially diminished in post-stenotic vessel segments⁸. Figure 1.3 shows the velocity waveforms of calf arteries from two patients with stenosis or occlusion in one of their legs. It can be observed that while the arterial waveform in one leg is typically triphasic, the arterial waveform in the other leg is dampened or even stagnant.

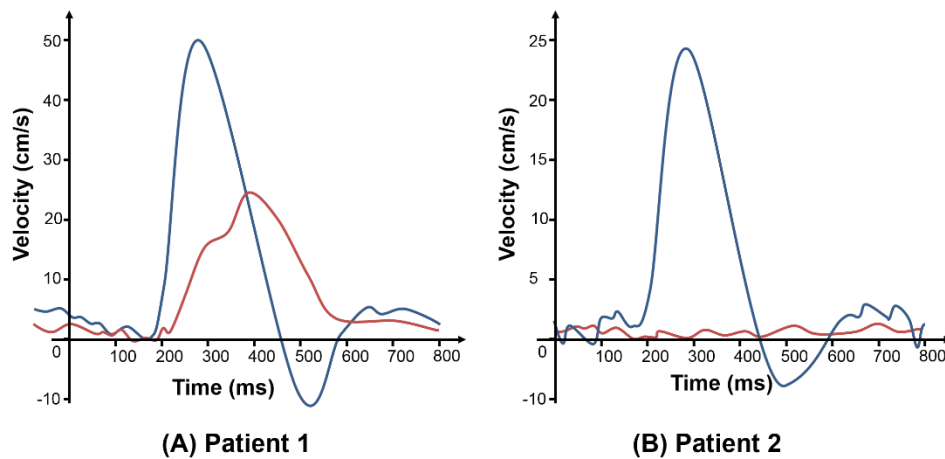


Figure 1.3 The velocity waveforms of calf arteries from two patients with stenosis (A) and occlusion (B) in one leg. The blue curves denote the healthy femoral artery, and the red curves denote the stenosed or occluded artery. The triphasic waveform is dampened (A) or even become stagnant (B).

1.2.3 Peripheral arterial disease

Peripheral vascular disease (PVD) involves damage to or blockage in the peripheral arteries and veins. The main forms that PVD may take include blood clots (for example, deep vein thrombosis), swelling (inflammation), or narrowing (stenosis) and blockage (occlusion) of the blood vessels.

When PVD affects only the arteries and not the veins, it is called peripheral arterial disease (PAD). PAD normally refers to an abnormal narrowing of arteries that restricts blood supply to leg muscles. More than 90% of PADs are caused by atherosclerosis ⁹, in which lipid deposits (plaques) build up in the wall of the arteries, narrowing their lumens and reducing blood flow. PAD also increases the risk of developing other complications, such as ischemia, myocardial infarction and stroke ¹⁰. Nowadays, PAD has become one of the leading causes of morbidity and mortality in the western world ¹¹. The incidence of PAD varies in the general population from 3–10% in people younger than 70 years to 15–20% in people older than 70 years ^{12,13}.

1.3 Summary

In summary, the anatomy and physiology of the vascular system was described in this chapter. The characteristics of arteries and veins were summarised and compared, which are important for designing the suitable imaging techniques for them. The properties of blood were described, such as the MR properties and flow characteristics. These properties are exploited by NCE-

MRA techniques to generate angiograms. Finally, peripheral vascular diseases were briefly described.

Chapter 2. Angiography techniques

This chapter initially presents commonly used diagnostic angiographic methods, along with their advantages and disadvantages. The state of the art NCE-MRA techniques will be introduced. Current NCE-MRA techniques will be categorised into three different types, and their principles, implementations and limitations will be summarised. As the main technique used in the following chapters, fresh blood imaging will be introduced in detail.

2.1 Vascular imaging techniques

Common vascular imaging techniques include digital subtraction angiography (DSA), ultrasonography, computed tomography angiography (CTA) and magnetic resonance angiography (MRA).

DSA is a type of X-ray fluoroscopy technique. Images are produced by subtracting a mask image, acquired prior to the arrival of the contrast medium, from the image obtained after the contrast medium has been introduced. DSA has high spatial and temporal resolution, but it exposes the patient to ionising radiation. Moreover, it requires the injection of iodinated contrast media, often via an intravascular catheter, which is invasive and potentially nephrotoxic.

Ultrasonography can provide both anatomic and hemodynamic information about blood vessels and flow. The structure of vessels and the direction, velocity, and patterns of blood flow can be displayed. Ultrasonography has many advantages as it is non-invasive, inexpensive, quick, easily portable and avoids ionising radiation. Moreover, Doppler ultrasound can provide a real-time display with high temporal resolution. However, ultrasound is unable to penetrate into deeper structures or pass through a tissue-gas or tissue-bone boundary.

CTA is also commonly used in routine clinical practice. It combines the use of X-rays with computerised image reconstruction, and provides rapid acquisition of high quality images that display the anatomical detail of blood vessels more precisely. Compared with other two-dimensional (2D) imaging techniques, CTA is able to display vessels from an unlimited number of angles, and from both inside and outside the vessel wall. The main disadvantage is that CTA also involves exposure to ionising radiation and requires a carefully timed injection of iodinated contrast media.

MRA uses magnetic fields and radiofrequency (RF) to visualise blood vessels inside the body. It is considered relatively safe as it avoids both ionising radiation and, depending on the technique, the potential complications of exogenous contrast material. Moreover, MRA can combine anatomic depiction with functional assessment, such as flow quantification in terms of velocity and direction. Despite the drawbacks of a long acquisition time, relatively high cost and inability to scan patients with contraindications such as some active or passive implants, MRA is used routinely and with expanding indications as a diagnostic tool for the evaluation of vascular disease.

MRA can be performed with or without the use of an exogenous contrast agent. Contrast-enhanced MRA (CE-MRA) requires the injection of a contrast agent, typically a gadolinium (Gd) chelate, while NCE-MRA is based on blood flow or the physical properties of blood.

Figure 2.1 shows typical images of DSA, ultrasonography, CTA and CE-MRA. Table 2.1 compares different characteristics of these vascular imaging techniques.

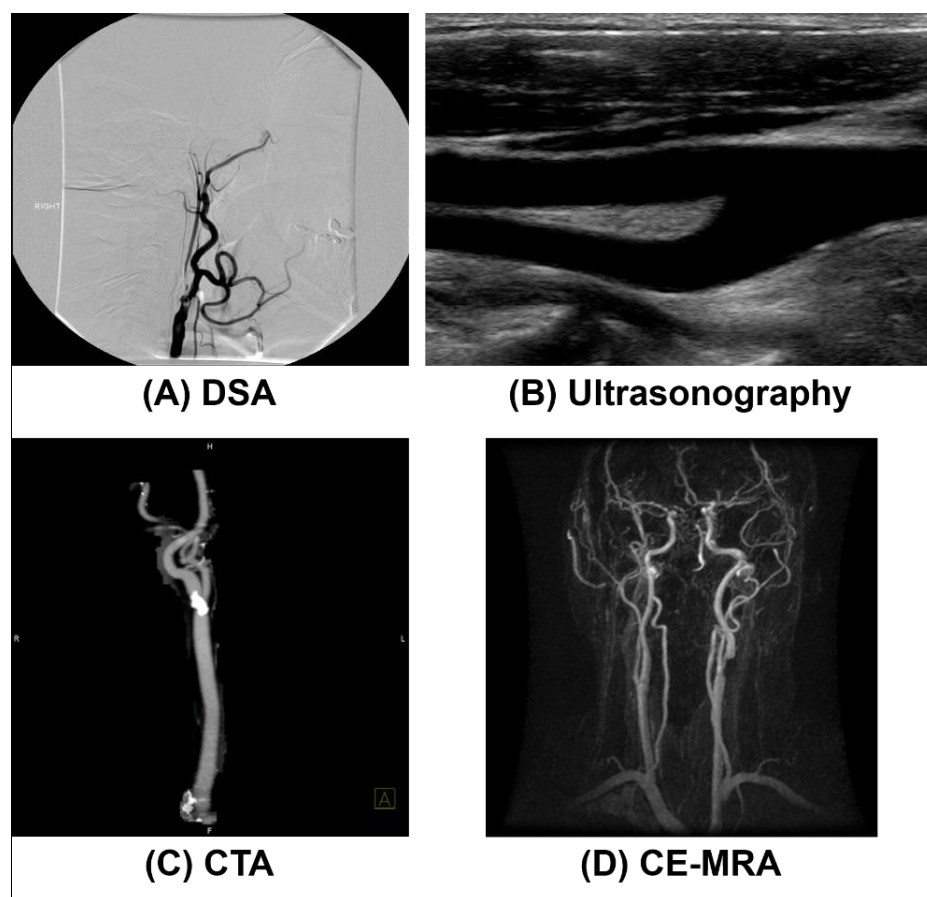


Figure 2.1 Typical images of carotid arteries obtained by (A) DSA, (B) ultrasonography, (C) CTA and (D) CE-MRA. Images courtesy of Martin J Graves.

Table 2.1 Comparisons between different vascular imaging techniques

| | Invasiveness | Ionising radiation | Contrast agent | Spatial resolution | 3D acquisition | Time-resolved | Hemodynamic information | Extravascular information | Cost | Examination time | Availability and portability |
|---------|--------------|--------------------|--------------------------|--------------------|----------------|---------------|-------------------------|---------------------------|-----------|------------------|------------------------------|
| DSA | high | yes | iodinated contrast media | very high | no | yes | yes | no | very high | short | low |
| US | none | no | none | high | no | yes | yes | yes | low | short | high |
| CTA | low | yes | iodinated contrast media | high | yes | not typically | no | yes | medium | short | low |
| CE-MRA | low | no | Gd chelates | medium | yes | possible | possible | possible | high | long | low |
| NCE-MRA | none | | none | | | | | | | | |

2.2 CE-MRA versus NCE-MRA

2.2.1 CE-MRA

CE-MRA was firstly proposed by Prince in 1994 ¹⁴. Due to its excellent image quality, speed and robustness, CE-MRA has been widely adopted for routine clinical practice.

CE-MRA is based on the rapid transient shortening of the blood's T_1 relaxation time due to the paramagnetism exhibited by Gd-containing contrast agents. The Gd-based contrast agents can reduce the T_1 value of blood to approximately 50 milliseconds, which is much shorter than that of the surrounding tissues. The contrast agent is injected into the venous circulation through a peripheral vein, either with an automatic injector or manually. Lower-extremity MRA is typically associated with the highest contrast dose protocols of all MR imaging techniques, often requiring a dose of 0.1 mmol/kg of Gd-chelate (at 1.5 T) to be injected ¹⁵.

Once the contrast bolus arrives in the vessel of interest, a rapid T_1 weighted spoiled gradient-echo pulse sequence is typically performed with a short TR to achieve high blood signal and low background signal, and a short echo time (TE) to minimise the flow-induced dephasing effect. The blood enhancement is maximised by timing the arrival of the contrast agent such that the period of maximum arterial concentration corresponds to the centre of k -space acquisition. Timing the contrast bolus is critical for acquiring first-pass images of diagnostic quality, which can be achieved by either test bolus timing or fluoroscopic triggering.

Test bolus timing uses a small (1–2 mL) test dose of contrast agent, which is injected at the same rate as for the actual CE MRA acquisition. A series of rapidly acquired 2D images are then obtained every 1–2 seconds. The time course for passage of the test bolus is determined by visual observation or signal intensity analysis.

In fluoroscopic triggering, the full bolus of contrast is administered while a 2D "fluoroscopic" image of the vessel of interest is acquired continuously using a rapid gradient-echo sequence. The CE-MRA acquisition begins as soon as the arrival of the bolus is detected by the imaging radiographer based on the signal increase on the image. The detection can also be conducted by automatic methods, which identify the arrival of the bolus when a specified signal threshold is exceeded.

The post-processing technique with the maximum intensity projection (MIP) enables different views of the three-dimensional (3D) data set. Sequential images can also be obtained over the same area, which allows not only visualising vessel structure but also assessing temporal dynamics. Figure 2.2 presents a reconstructed MIP of a CE-MRA study of the lower iliac and leg arteries.

Time-resolved CE-MRA sequences can also be used to obtain a series of images displaying the passage of the contrast bolus ¹⁶. These techniques employ fast imaging sequences to repeatedly acquire views of the imaging volume as contrast agent passes through the regional circulation. The view-sharing technique ¹⁷ is used to improve the temporal and spatial resolution by sampling the centre of k -space at higher frequency than the peripheral segments. Typical vendor-specific implementations of time-resolved CE-MRA include TRICKS ¹⁸ and DISCO ¹⁹ in GE systems, TWIST ¹⁶ in Siemens systems and 4D-TRAK ²⁰ in Philips systems.

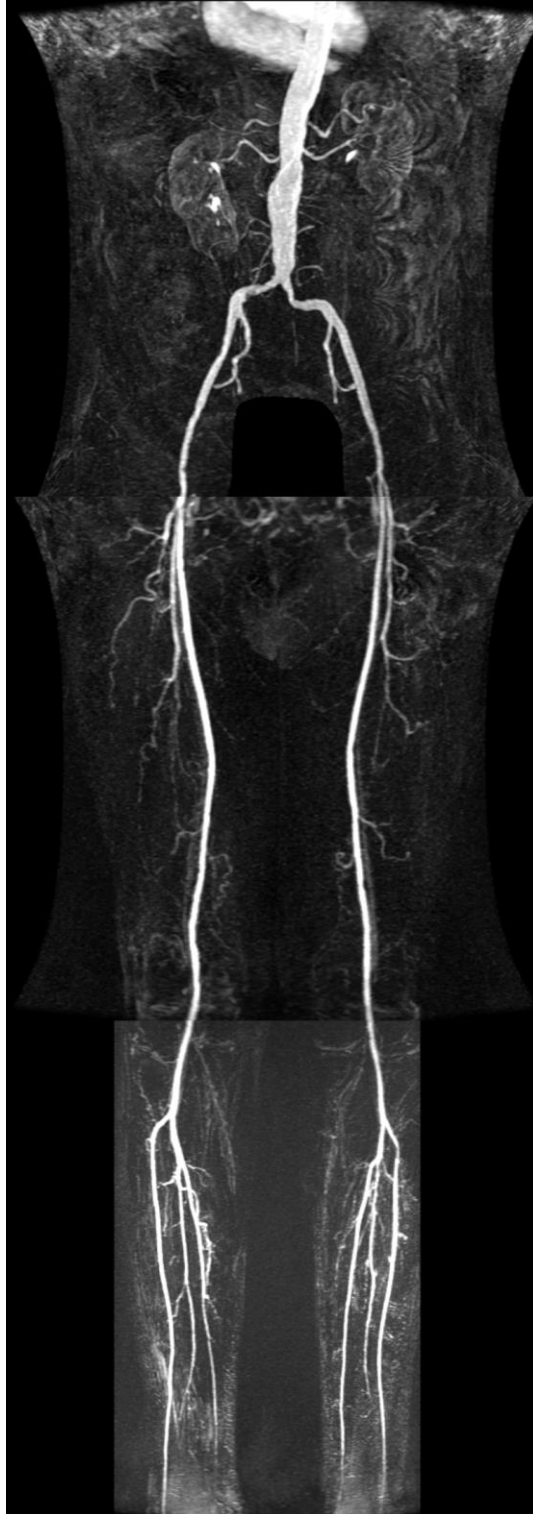


Figure 2.2 CE angiograms acquired from a volunteer demonstrating the lower iliac and leg arteries. The images are MIPs of three acquisitions.

2.2.2 Renaissance of NCE-MRA

Before the development of CE-MRA techniques, NCE-MRA techniques such as traditional time-of-flight (TOF) and phase-contrast (PC) MRA were developed and applied in various applications. However, the widespread use of these early NCE-MRA techniques was limited by prolonged acquisition times and flow-related artefacts that favoured CE-MRA ¹⁵.

Technical advancements in MR hardware and software have contributed to renewed interest in NCE-MRA. The use of higher field strengths, stronger and faster gradients, multi-channel receiver coil arrays and the application of image acceleration techniques have greatly reduced the acquisition times and improved image quality. These significant advances have made some NCE-MRA methods clinically practical. More importantly, CE-MRA has some limitations that have drawn increasing attention.

Firstly, the safety of Gd-based contrast agents (GBCAs) has become a concerning issue. The association between high doses of GBCAs and nephrogenic systemic fibrosis in patients with renal failure was first reported in 2006 ²¹. More recently, in 2014, Kanda *et al.* reported convincing evidence that linked increased MRI signal intensity in deep nuclei of the brain with repeated administration of GBCAs ²². Gd deposition has been confirmed in brain tissue by several following publications, regardless of renal or hepatobiliary dysfunction ^{23–28}. This has led to warning notices by the Food and Drug Administration ²⁹ and the suspension of linear Gd contrast agents by the European Medicines Agency ³⁰ in 2017. Such concerns have further increased interest in developing exogenous contrast-free alternative methods.

Another drawback of CE-MRA is its high dependence on accurate timing of the contrast agent bolus. Improper timing can result in missing the passage of the contrast bolus and inadequate vascular visualisation. Scanning too late also leads to venous contamination, which can obscure arterial anatomy ³¹. Timing of the bolus is particularly challenging in peripheral extremities, where test bolus examinations and bolus tracking techniques may be limited because small vessel opacification can be obscured by inflow effects ³².

Furthermore, CE-MRA is typically limited by dose to a single area of examination. It cannot be repeated immediately if the time of the peak bolus is misjudged, while NCE-MRA can be repeated in the case of technical error ³³.

Finally, situations may occur where NCE-MRA is preferred due to difficulties gaining intravenous access or contraindications for contrast materials. For example, an intravenous catheter may be difficult to place in patients who are obese or with occluded, fragile or small veins, and intravenous contrast agents are usually not given to pregnant patients due to increased risk of harm to the foetus

34.

2.3 Review of NCE-MRA techniques

According to their different imaging principles, current NCE-MRA techniques can be divided into three categories, including techniques based on the inflow of blood out of the imaging volume (inflow-based techniques), techniques based on blood flow within the imaging volume and flow-independent techniques. This section will introduce the state-of-art of NCE-MRA techniques and summarise their advantages and disadvantages.

2.3.1 Inflow-based techniques

Inflow-based techniques belong to an early class of NCE-MRA techniques, which rely on the inflow effect of blood. In these techniques, static tissues within the image plane are suppressed by using suppression imaging pulses or preparation modules. Inflowing blood spins entering the image plane arrive with fresh longitudinal magnetisation, generating high signal intensity.

TOF

TOF^{35–37}, developed in the late 1980s, was the dominant NCE-MRA method for the following two decades. Although now largely supplanted in body MR imaging by other techniques, it remains one of the most important methods for cerebral MRA.

TOF is a typical inflow-based technique. It employs repeated RF excitation pulses to saturate the signal from stationary tissue, causing their longitudinal magnetisation to approach a low steady-state value, resulting in suppressed background signal. In contrast, inflowing blood spins, which have not experienced the excitation pulses, will have high signal intensity (Figure 2.3). The typically short TR and large flip angles assure sufficient background suppression. The venous inflow signal can be suppressed by adding a slice-selective distal saturation band, illustrated by the hatched area in Figure 2.3.

TOF MRA can be implemented with 2D or 3D sampling, depending on the target vascular territory. 3D TOF MRA of the intracranial arteries is the single most widely used MRA technique ³⁸. 2D TOF MRA is preferred for imaging vessels with perpendicular flow and relatively fast velocity, such as carotid arteries ³⁹ and peripheral vasculature ⁴⁰. Figure 2.4 shows typical images of 2D and 3D TOF.

The main limitation of 3D TOF is the saturation of protons in vessels within the imaging section or slab where flow lies within the plane of imaging. This problem can be largely solved by using the tilted optimised non-saturating technique (TONE) ⁴¹, which progressively increases flip angles through the slab to compensate for the saturation of blood flowing into the slab. Another solution is multiple overlapping thin slab acquisition (MOTSA) ^{42,43}, which acquires the image volume as multiple thin 3D slabs instead of a single volume 3D acquisition. Other drawbacks of TOF include its relatively long scan time leading to motion artefacts and the signal degradation in vessels containing slow, turbulent or retrograde flow.

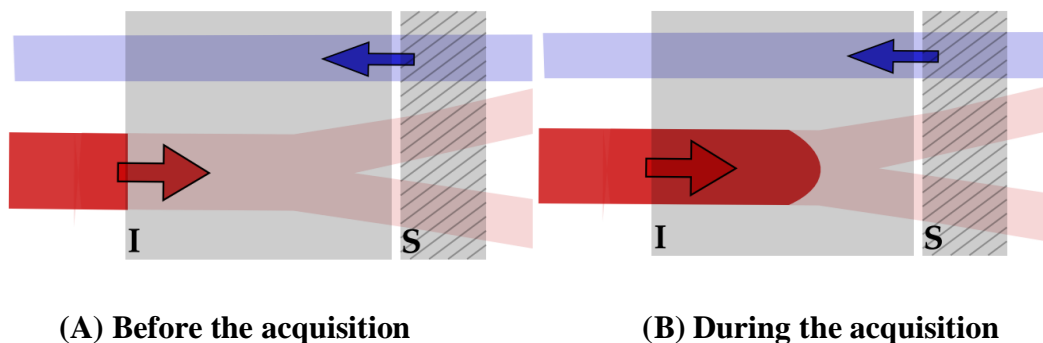


Figure 2.3 The mechanism of TOF effect is illustrated with a model containing an artery (red) and a vein (blue). The imaging (I) and the saturation (S) slab are pictured in grey and shaded grey, respectively. (A) The contrast situation before the inflow of unsaturated spins is shown, both arterial and venous blood, as well as the static tissue, is suppressed. (B) The inflowing arterial blood (bright red) leads to contrast generation, while the static tissue and the venous blood are still suppressed. Taken from ⁴⁴.

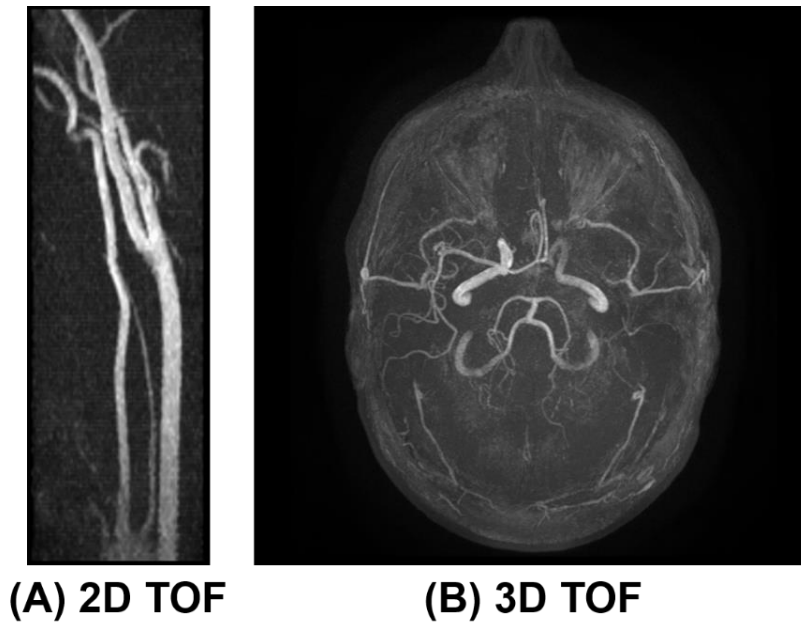


Figure 2.4 Example images of 2D TOF of carotid arteries (A) and 3D TOF of intracranial arteries (axial MIP) (B). Images courtesy of Andrew Priest.

IFIR and QISS

Inflow inversion-recovery (IFIR) and quiescent inflow slice-selective (QISS) are another two techniques that exploit the inflow enhancement effect.

IFIR employs slab-selective inversion pre-pulses followed by a substantial inversion time (TI). The TI not only nulls signal from background tissues, but also allows time for fresh (uninverted) arterial blood to flow into the imaging volume⁴⁵. IFIR is mostly applied to image the arterial vasculature with relatively fast flow, such as the renal and carotid arteries³³.

QISS applies a pair of closely spaced 90°-RF pulses to saturate static tissue and venous inflow respectively. Next comes a quiescent interval (QI) of a few hundred milliseconds, during which fresh inflowing blood enters the imaging slice. The sequence is ECG-gated to ensure that the QI spans the period of rapid systolic arterial flow, whereas the signal is acquired during diastole. QISS performs best when arteries are long and perpendicular to the plane of imaging. Therefore, it is mainly used for run-off studies in peripheral arteries⁴⁶.

The setting of TI or QI is the main problem of IFIR and QISS. For IFIR, a longer TI can provide greater inflow of spins into the anatomy of interest but can generally provide poorer blood-to-background contrast due to T_1 -recovery of background tissue signal ³³. For QISS, the QI needs to be adjusted according to the heart rhythm. Some patients may have a delayed onset or prolonged duration of systole ⁴⁶.

ASL

Arterial spin labelling (ASL) uses RF pulses to magnetically tag protons in arterial blood in arteries prior to their entry into an organ or capillary bed. When these labelled protons enter a new anatomic region, they can be used to produce an arteriogram due to their unique magnetisation states. ASL acquires two image sets in an alternated fashion: a tag image with upstream tagging of arterial blood and a control image without tagging. Subtraction of the two image sets renders the arteries bright upon a background of negligible signal. Representative ASL techniques based on the inflow effect include STAR ⁴⁷, FAIR ⁴⁸, STARFIRE ⁴⁹, and EPISTAR ⁵⁰.

ASL MRA removes the signal from stationary tissue via image subtraction, achieving complete background suppression. Compared with IFIR and QISS, ASL MRA has less dependency on TI/QI, and therefore can be applied for arteries with slow-flowing blood like those in the distal extremities ³³. A drawback of ASL is that it requires two data acquisitions, which doubles scan time and increases motion sensitivity which can lead to unwanted artefacts.

2.3.2 Techniques based on flow within the imaging volume

The spin-phase effect

Another kind of NCE-MRA technique exploits the spin-phase effects of blood flow within the imaging volume. The spin-phase effect refers to changes in the phase that protons undergo when they move within a gradient field. The spin-phase effects on moving and stationary spins from a pair of bipolar gradients are demonstrated in Figure 2.5. A stationary spin will experience no net phase shift, but a moving spin will have a net phase shift proportional to its velocity.

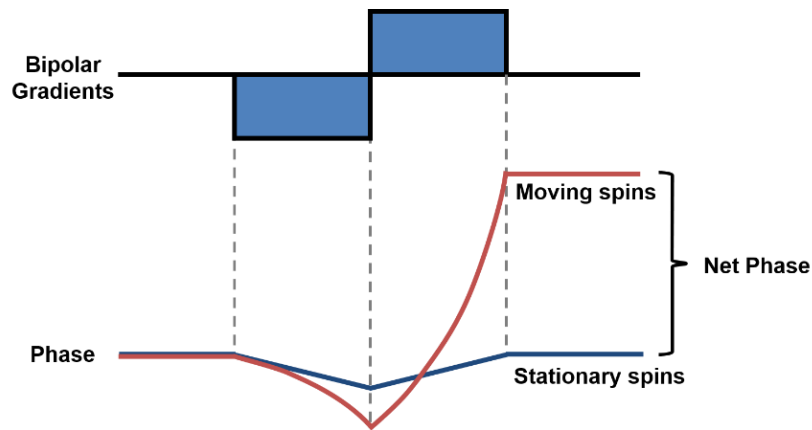


Figure 2.5 Spin-phase effects on moving (red curve) and stationary (blue curve) spins under a pair of bipolar gradients

PC-MRA

Conventional PC-MRA uses a pair of bipolar gradients shown in Figure 2.5 to create contrast in a phase image between flowing blood and stationary tissue ^{51,52}. It requires at least four acquisitions for 3D MRA, including one flow compensated gradient-echo dataset as the reference and three flow-encoded datasets acquired in the slice, phase and readout directions. Therefore, conventional PC-MRA has a long acquisition time, and its use as a routine angiographic method has greatly declined ⁵³. It is currently still used as a low-resolution scout sequence for identifying the location of the carotid arteries and for cardiac studies.

PC-MRA can also be used for quantitative measurement of flow velocities in three dimensions because the phase shift is proportional to its velocity. This method is used routinely in cardiac imaging for assessing pulmonary artery bulk flow and in the aorta for measuring cardiac output. The emerging technique of 4D PC imaging comprises 3D spatial encoding, 3D velocity encoding and time ⁵⁴. It affords a comprehensive evaluation of regional blood flow characteristics. The technique has been applied to the measurement of aortic pulse wave velocity ⁵⁵ and wall shear stress ⁵⁶ for the purposes of identifying potential emboli from high-risk atherosclerotic plaque ⁵⁷.

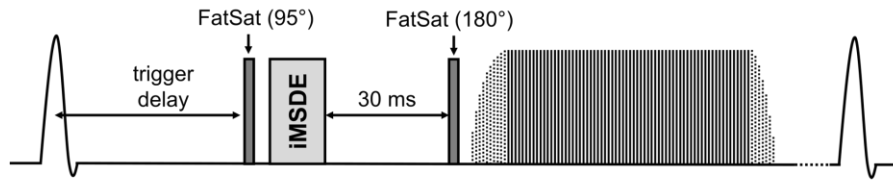
FSD and FBI

There are also subtraction-based NCE-MRA techniques utilising the spin-phase effect, such as Flow-sensitive Dephasing (FSD) ^{58–60} and Fresh Blood Imaging (FBI) ^{61,62}. Like ASL techniques,

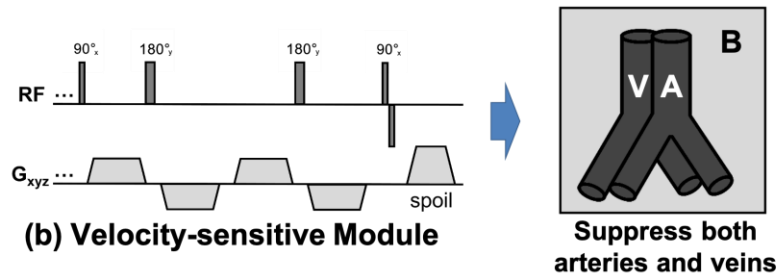
FSD and FBI generate angiographic images by selectively subtracting images with flowing blood suppressed (dark-blood images) from images in which it is not suppressed (bright-blood images).

Blood suppression in FSD is achieved by applying specially designed magnetisation preparations (Figure 2.6). Priest *et al.* used acceleration-sensitised (Figure 2.6(b)) or velocity-sensitised (Figure 2.6(c)) preparations to suppress the vascular signal flexibly, either in arteries alone or in arteries and veins together^{59,60}. Delay alternating with nutation for tailored excitation (DANTE) can also be used as an effective blood suppression module, but always for suppressing both arteries and veins⁶³. FSD techniques have been mainly applied in peripheral angiography, including vessels in the lower extremities^{58–60,64} and hand⁶⁵. Recent studies have also demonstrated the feasibility of imaging the thoracic central veins^{63,66}.

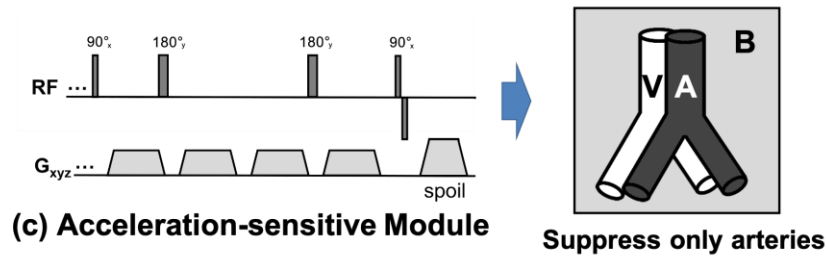
FSD allows flexible user-selective suppression of vascular signals, which enables the separation of arterial and venous signals. Figure 2.7 shows example FSD images of lower legs. Acceleration-sensitised and acceleration-sensitised iMSDE (improved motion-sensitised driven-equilibrium) preparation modules were used together with a 3D balanced steady-state free precession (bSSFP) sequence. Separate images of arteries (A) and veins (B) can be obtained in one single acquisition.



(a) Schematic overview of the sequence



(b) Velocity-sensitive Module

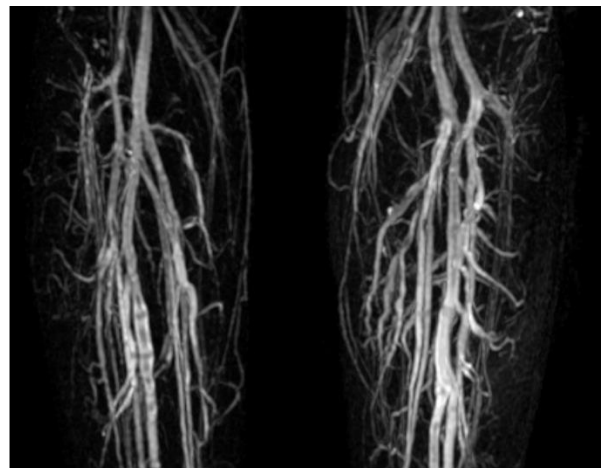


(c) Acceleration-sensitive Module

Figure 2.6 Schematic diagram of FSD pulse sequence. (a) Schematic overview of FSD. (b) The velocity-sensitised preparation module suppressing both arteries and veins. (c) The acceleration-sensitised iMSDE preparation module suppressing only arteries. Figures modified based on ⁶⁰.



(A) Arteries



(B) Veins

Figure 2.7 Example FSD images of lower legs. Specific angiographic images highlighting either arteries or veins can be generated by employing different types of iMSDE preparation modules together with selective image subtraction. Images courtesy of Andrew Priest.

In FBI, artery-suppressed and non-suppressed acquisitions are based on the differential flow between systole and diastole in vessels with pulsatile flow. Details of FBI will be described in section 2.4.

The main drawback is that both FBI and FSD require a long imaging time due to ECG-triggering and image subtraction, making them more prone to motion-induced image blurring, as well as image degrading motion artefacts. Moreover, abnormal flow patterns in patients with vascular disease can complicate the optimal acquisition of dark-blood and bright-blood contrasts in systole and diastole, *e.g.*, causing imperfect timing of the triggered acquisitions, which can also lead to image artefacts³³. Perfect triggering is also difficult for patients with cardiac arrhythmia⁶⁷.

Another problem of FBI and FSD is that the static background signal intensities from the two unsubtracted source image sets may not be exactly identical^{68,69}. This signal intensity difference can lead to residual background signal, obscuring the vascular signal of interest and affecting clinical diagnosis. This problem will be addressed in Chapter 4, in which an intensity correction technique is proposed to suppress residual background tissue.

Velocity-selective MRA

Velocity-selective (VS) angiography⁷⁰ uses a VS module which selectively excites magnetic spins based on their velocities. The VS inversion preparation is applied at the appropriate phase of the cardiac cycle to invert stationary tissues and venous blood while preserving arterial blood. After an inversion delay time chosen for optimal background suppression, artery visualisation over a large field-of-view (FOV) can be achieved. The VS inversion pulse can also be used to invert arterial blood and provide visualisation of veins⁷¹.

Compared to IFIR MRA that uses slab-selective inversion pulse, VS MRA is not limited by the inflow of arterial blood, which relaxes the requirement for a long TI and allows the display of a longer extent of vascular anatomy. Like FBI and FSD, VS-MRA also depends on the use of ECG-gating, and the image quality may be affected by imperfect triggering. Another possible drawback

of VS-MRA is the requirement to tune the velocity selective preparation for optimal arterial display³³.

2.3.3 Flow-independent NCE-MRA

Both the inflow effect and spin-phase effect are flow-dependent. These effects can be degraded in vessels with slow, recirculatory or stagnant flow. Flow-independent methods avoid this problem by exploiting intrinsic tissue parameters such as T_1 and T_2 to suppress background signals and generate vessel contrast.

Balanced steady-state free precession imaging (bSSFP) is the prevailing method for flow-independent NCE-MRA⁷². In bSSFP images tissues with large T_2/T_1 ratios are hyperintense while others having small ratios are relatively hypointense. Due to the large T_2/T_1 ratio of arterial and venous blood, both arteries and veins are well depicted. Flow-independent MRA using bSSFP can provide a good depiction of slow and static flow as well as small branch vessels. It is also particularly useful for depicting vessels with complex morphology, such as the coronary arteries³³. However, the sensitivity of bSSFP to B_0 field inhomogeneity makes the technique susceptible to off-resonance banding artefacts, unlike fast spin-echo (FSE)-based sequences⁷³.

The background tissue signal can be suppressed by incorporating bSSFP with magnetisation preparation modules. Magnetisation preparations applied include non-selective inversion-recovery for suppression of long T_1 fluids⁷⁴, T_2 preparation for muscle suppression⁷⁵, and chemically selective fat saturation or multi-echo Dixon methods for fat suppression⁷⁶. Subtraction-based bSSFP techniques have also been proposed for flow-independent MRA. For example, STARFIRE can provide improved suppression of unwanted signal from background tissue⁷⁷.

2.3.4 Limitations of NCE-MRA techniques

In summary, current NCE-MRA techniques have the common drawbacks as follows:

Long acquisition time

While the short repetition time (TR) of CE-MRA enables very fast imaging speed, most of the NCE-MRA methods have a much longer acquisition time, especially for those requiring more than one acquisition. The long acquisition time not only limits the clinical acceptance of these techniques,

but also renders them sensitive to artefacts from patient motion. The resolution that can be achieved is also limited by the long acquisition time.

Complex flow characteristics

The pulsatile pattern of blood flow can vary between different anatomical areas and between different subjects. Although the application of ECG gating can ensure the data is sampled in the same phase of the cardiac cycle, the complex and unpredictable flow patterns in some patients can cause some problems for flow-dependent NCE-MRA techniques. Common problems include:

a) Slow arterial flow

Inflow-based techniques, such as TOF and IFIR, preferred for imaging vessels with relatively fast flow. However, the blood flow in peripheral arteries and veins is sometimes slow or even stationary, which will degrade the blood signal suppression effect.

b) Pulsatile veins

The separation of arteries and veins in FSD and FBI is based on the fact that arterial flow is pulsatile while venous flow is constant. However, flow in the veins near the heart is also quite pulsatile. Therefore, techniques relying on slow constant venous flow only work well in the peripheries.

c) Complex flow patterns

Some complex flow patterns, such as recirculatory or stagnant flow, exist in vessels with a unique morphology, *e.g.* the carotid bifurcation. These complex patterns can cause artefacts in many flow-dependent techniques.

d) Abnormal flow patterns in patients

Examinations in patients are much more challenging than those in healthy volunteers as the flow patterns under pathological conditions may not follow the standard pattern and become disordered. For example, atherosclerosis involves a narrowing of the artery lumen, referred to as a stenosis, which together with flow pulsatility can result in the periodic generation of complex fast flow and turbulence ⁷. Flow may be substantially chaotic in post-stenotic vessel segments ⁸.

The flow in different locations can be affected by different ways. As shown in 1.2.2 and Figure 1.3, peripheral arteries with stenosis may have different peak flow timing and velocity compared to the other ‘healthy’ peripheral arteries. Abnormal flow patterns can degrade the inflow or spin phase effects, and can complicate the detection of systole and diastole in ECG-based techniques like FBI ³³.

Artefacts

Compared with contrast enhanced techniques NCE-MRA methods tend to have a higher incidence of different kinds of artefacts, such as motion artefacts caused by long acquisition times, and the artefacts caused by complex flow patterns. Specific artefact types may also exist in some NCE-MRA methods, including misregistration artefacts in methods requiring subtraction of different image sets, artefacts from saturation and dephasing of flowing spins in TOF, and the banding artefacts in regions of off-resonance in bSSFP.

Vessel orientation

Some flow-dependent techniques have requirements on the vessel orientations. For example, TOF and other inflow-based methods ideally require the plane of acquisition to be perpendicular to the blood vessels. For FSD, blood flow perpendicular to the flow-dephasing direction will not be suppressed ⁵⁹. Adding additional FSD modules with orthogonal flow-dephasing directions can improve the suppression but will decrease the signal-to-noise ratio due to T_2 decay ^{66,78}.

Parameter selection

Some flow-dependent approaches have challenging requirements for selecting and adjusting the acquisition parameters, which may complicate the operations and affect the robustness of the technique. For example, IFIR requires careful selection of the TI with respect to the flow velocity in the vessel of interest and the T_1 of stationary tissue. The QI in QISS MRA also need to be adjusted according to the heart rhythm because some patients may have a delayed onset or prolonged duration of systole.

2.4 Fresh blood imaging

Most of the NCE-MRA studies in this thesis will be based on the FBI technique. FBI, also named as ECG-gated half-Fourier FSE, derives from the gated subtraction angiography techniques

proposed in mid-1980s^{61,62}. FBI obtains MRA images by subtracting dark-blood images from bright-blood images. The dark-blood and bright-blood image acquisitions are based on the differential flow between systole and diastole in vessels containing pulsatile flow. In the FSE imaging sequence, the fast arterial flow during systole results in spin-dephasing and renders arteries dark. In contrast, arterial signal is preserved during diastole due to slow flow. Venous blood in general has relatively constant slow flow and is thus bright throughout the cardiac cycle.

2.4.1 Conventional FBI

The concept of FBI was first proposed by Miyazaki *et al.*⁷⁹. An ECG synchronised 3D half-Fourier FSE technique with an appropriate ECG delay time for every phase encoding was used for arterial image acquisition. Figure 2.8(a) shows the diagram of the 3D imaging sequence. A spatially nonselective short-time inversion recovery (STIR) pulse was applied for fat suppression and background signal attenuation. Systolic and diastolic acquisitions were acquired with different delay times. The two acquisitions were interleaved to minimise sensitivity to motion.

Prior to each 3D FBI acquisition, an ECG preparation scan using 2D half-Fourier FSE sequence was acquired in a single section with multiple phases (Figure 2.8(b)). The appropriate cardiac phase and ECG delay time could be then determined and used for the 3D FBI acquisition.

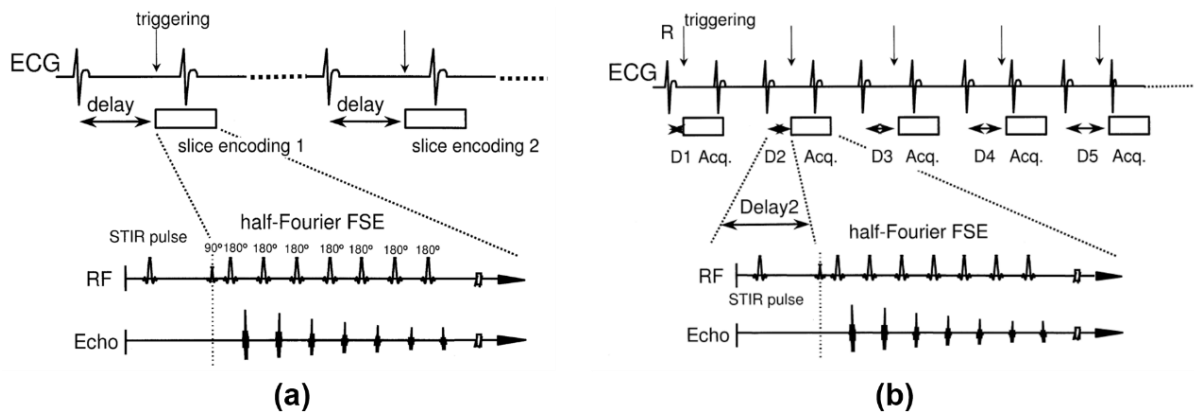


Figure 2.8 (a) Sequence diagram of ECG-synchronised 3D half-Fourier FSE. The 3D half-Fourier FSE sequence is ECG synchronised for each slice encoding to have the same cardiac phase in every slice partition. (b) Schematic diagram of ECG-prep, single slices in multiple phases. Various delay times are ECG triggered, followed by 2D half-Fourier FSE to obtain single-slice images in different phases. Taken from⁷⁹.

2.4.2 FBI with flow-spoiled gradient pulses

The arterial flow in peripheral vessels is much slower than large arteries such as thoracic and abdominal arteries, which results in bright-blood signal even during systole and makes it difficult to separate arteries from veins. The flow-spoiled fresh-blood imaging technique was therefore proposed in 2003⁸⁰, which creates better suppression of artery blood signal in systole by using readout flow-spoiled pulses in FBI. Figure 2.9 shows sequence diagrams of (a) the original readout gradient and (b) the readout gradient with flow-spoiled gradient pulses. The flow-spoiled gradient pulses cause the pulsatile flow blood to further dephase or become a flow void during systole but not during diastole as a result of reduced flow. The slow venous flow in both systole diastole and the stationary background tissues are not affected by the flow-spoiled gradient pulses. Therefore, subtraction of the diastolic and systolic images provides arterial images.

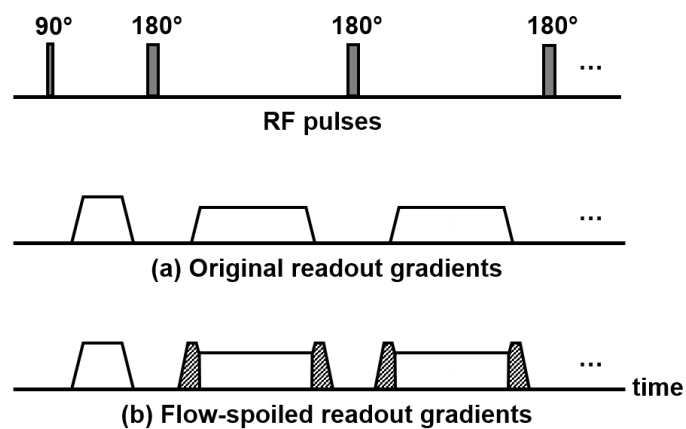


Figure 2.9 Sequence diagram of FBI using the original readout gradients (a) and flow-spoiled gradients (b).

2.4.3 FBI with variable flip angles

Another modified FBI technique using variable flip angles has also been proposed by Storey *et al.* in 2010⁸¹. It was reported that the flow sensitivity is governed largely by the flip angle of the refocusing pulses and to a lesser extent by the flow-spoiled gradients. High refocusing flip angles ($>160^\circ$) produce very bright signal in bright-artery images, but also refocus more signal in arteries with slow-flowing blood in dark-artery images. The subtraction angiogram has bright signal for large arteries but weak signal for small arteries. In contrast, low refocusing flip angles ($<120^\circ$) produce lower signal for large arteries in bright-artery images, but small arteries with slower

diastolic flow are less affected. The low refocusing angle accentuates the spin-effect, resulting in reduced arterial signal in dark-blood images, even in smaller arteries with slow-flowing blood. Therefore, a low refocusing flip angle produces a subtraction angiogram with better visualisation of distal branch arteries but results in signal loss in the main arteries.

A flow suppression technique using variable refocusing flip angles is implemented on GE's systems, which is called "adaptive refocus". For systolic acquisition, the first few refocusing pulses are reduced from 180° to a smaller value such as 105°, so that the flow sensitivity and the arterial suppression are improved. The refocusing flip angles for diastolic acquisition remain 180° to maximise the arterial signal for bright-artery images.

2.4.4 Applications

FBI is commercially available and can be used for imaging peripheral vascular disease in the distal lower extremities ³³. Its clinical usefulness has also been reported in aortic diseases, arterial occlusive diseases, and assessment for the vascularity of musculoskeletal neoplasm ^{82–84}.

Ono *et al.* have reported a new MR venography method utilizing the FBI technique ⁸⁵. MR venous images can be acquired by further subtraction of those subtracted arterial images from the systolic source images. Further clinical evaluation of this technique on 32 patients based on finding deep vein thrombosis compared with DSA provided 100% identification by two reviewers on all three stations with corresponding sensitivities of 100% and 99.6% ⁸⁶.

2.5 Summary

This chapter introduced the common angiographic techniques. DSA, ultrasonography and CTA are widely used for clinical evaluation of vascular anatomy and pathology, but they all have their respective shortcomings. MRI is another effective modality. While CE-MRA is more routinely used for clinical diagnosis, NCE-MRA techniques have drawn increasing attention as they can avoid the injection of exogenous contrast agents. Many NCE-MRA techniques have been developed based on different characteristics of blood, such as the flow-dephasing effect, inflow effect and T₁/T₂ properties. Their principles, applications and limitations were summarised in this chapter.

The following chapters focus mainly on subtractive NCE-MRA techniques, particularly FBI. As summarised in Sections 2.3.2 and 2.3.4, these techniques have some limitations, among which is residual background signal following subtraction caused by inconsistent background signal intensities on source images. This will be investigated in Chapter 4 and the related improvements facilitate addressing the main problem of long acquisition times dealt with in Chapter 5 and 6.

Chapter 3. Acceleration theory and compressed sensing reconstruction algorithm

This chapter describes the theory of compressed sensing. The split Bregman algorithm, which will be employed in the following chapters, is introduced as an efficient compressed sensing reconstruction method. Another two routinely used acceleration techniques, parallel imaging and partial Fourier sampling are also described, together with how to combine them with compressed sensing. A new L1-SPIRiT reconstruction algorithm is developed, which is based on the split Bregman and POCS method. Finally, four quantitative metrics for evaluating the quality of reconstructed images are presented, including two commonly used metrics and two new metrics developed specifically for the studies in this thesis.

3.1 Overview of MRI acceleration

3.1.1 MRI speed

MRI has a relatively slow imaging speed compared to other imaging modalities, which has become a major obstacle for the incorporation of body MRI into routine clinical practice⁸⁷. The low imaging efficiency leads to high economic cost and limits the number of patients. It is also challenging for patients to perform long breath-holds or remain still for imaging certain body parts⁸⁸. More importantly, long acquisition times cause technical challenges including limited spatiotemporal resolution and volumetric coverage, and sensitivity to respiratory or cardiac motion⁸⁷. The low temporal resolution increases the difficulty of capturing rapid motion or rapid changes in contrast over time. It also increases the susceptibility to motion-related artefacts, limiting the imaging of moving body parts, such as for cardiac and abdominal imaging⁸⁹.

3.1.2 Efforts in MRI acceleration

Much effort has been applied to improving imaging speed since the initial introduction of MRI. Over the years, the examination times of MRI have been dramatically reduced by the improvement of hardware and innovations in acquisition and reconstruction strategies.

Increased gradient amplitudes and slew rates can minimise the gradient waveform durations, enabling faster collection of data ⁹⁰. The emergence of rapid imaging sequences, such as FSE imaging ⁹¹, fast low angle shot (FLASH) imaging ⁹² and echo-planar imaging (EPI) ⁹³ have greatly increased imaging speed and motivated many new applications of MRI ⁸⁷.

However, we are currently at the point where the improvements in hardware and sequence design have come to practical limitations due to the fundamental physical and physiological effects ⁹⁴. For example, very fast gradient switching can induce electric fields in the human body, leading to muscle and nerve stimulation ⁹⁵. Faster sequence repetition and higher magnetic field strengths can lead to an increased RF energy deposition in tissues, resulting in patient heating ⁹⁶.

These fundamental limitations have encouraged researchers to look for new strategies to reduce the amount of acquired data in k -space based on the inherent redundancies in acquired MR image data. The underlying information may be extracted from less data than traditionally considered necessary according to the Nyquist criterion. Typical techniques are parallel imaging (PI), partial Fourier (PF) sampling and compressed sensing (CS). Other acceleration techniques exploiting other sources of redundancy are also emerging, such as k - t methods that take advantage of the sparsity of a dynamic time series ^{97–100}.

3.1.3 Acceleration for NCE-MRA

The NCE-MRA techniques addressed by this thesis have an especially strong potential for acceleration. As described in Chapter 2.3.4, most of the NCE-MRA methods have very long acquisition times.

Meanwhile, MR angiography exhibits a high degree of sparsity, which is visible even in the image domain ^{94,101}. Only the vessels have a bright signal, and background tissues are suppressed. The sparsity can be further improved by using sparsifying transforms. The intrinsic high sparsity is very beneficial for both PI and CS, potentially enabling angiograms to be accelerated by a large factor.

The acceleration of MRA using CS has become a hot topic since CS was proposed. CS has been applied to CE-MRA to reduce acquisition time and increase spatial and temporal resolution ^{102–104}. As a typical and widely used NCE-MRA technique, TOF-MRA has been addressed by a number of studies in terms of the acceleration based on CS ^{105–108}. The clinical performance of accelerated TOF has also been evaluated ^{109,110}. PC-MRA has been limited due to its long acquisition times. CS

can effectively accelerate PC-MRA ^{111–113}, particularly 4D flow ^{112,113}. Studies focusing on the CS acceleration of other NCE-MRA techniques include bSSFP ¹¹⁴ and ASL ¹¹⁵.

FBI is a typical NCE-MRA technique with high demand for acceleration. As an ECG-gated technique, data collection in FBI is limited to a relatively small portion of each cardiac cycle. Moreover, FBI requires two acquisitions for image subtraction, which not only doubles the acquisition time but also renders it sensitive to misregistration problems caused by motion. Therefore, PF sampling has been applied to FBI since it was proposed ⁷⁹. PI has also been routinely applied in the clinical protocol. More recently, CS has become available in NCE-MRA protocols including FBI by different vendors.

Since the source bright- and dark-blood images of subtractive NCE-MRA techniques like FBI contain many background tissues, the sparsity of angiograms can only be exploited by performing reconstruction on the subtracted data. The details of the reconstruction strategies for subtractive NCE-MRA will be described in Chapter 6.

3.2 Compressed sensing

3.2.1 Basic idea of compressed sensing

It has been well established that a wide range of signals are compressible to some degree, *i.e.* that they can be represented by only a few non-zero coefficients in a suitable basis or dictionary. Since the signal can be compressed by a post-processing operation, CS emerged from the question of whether we can simply measure the compressed information directly from a smaller number of measurements. Candès and Donoho *et al.* proved that if the undersampling scheme is incoherent, images can be accurately reconstructed by using a non-linear recovery process ^{116,117}

The application of CS in MRI has drawn great attention since it was first proposed by Lustig *et al.* in 2007 ¹⁰¹. The acquisition scheme of MRI is highly compatible with CS theory. MR images have a sparse representation in some transform domain (wavelet *etc.*). The MRI data is acquired in *k*-space, and the acquisition time is directly related to the number of sampling measurements. Therefore, the acquisition time can be efficiently reduced by performing an incoherent undersampling scheme.

Figure 3.1 is a heuristic example explaining how incoherent (random) sampling is performed on a one-dimensional (1D) sparse signal and how the incoherent artefact can be removed by the CS reconstruction.

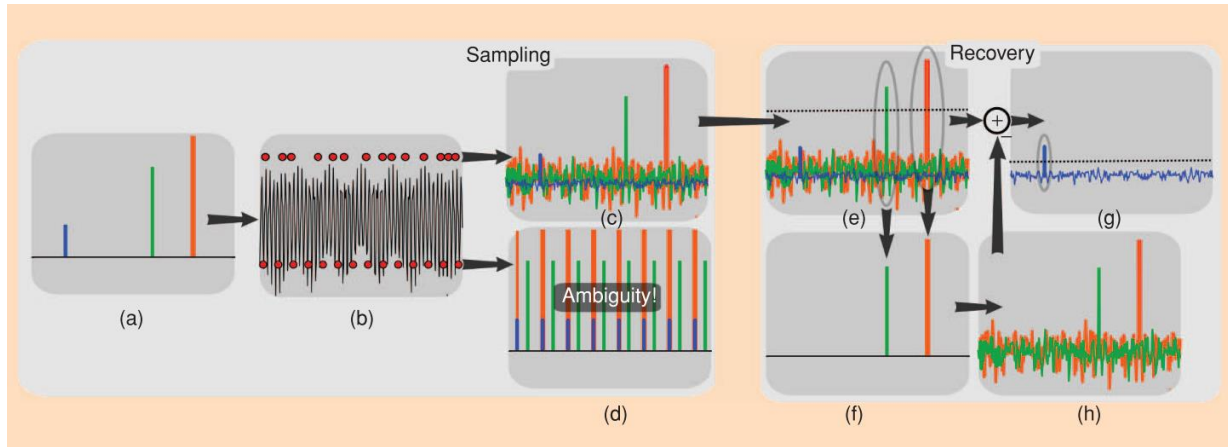


Figure 3.1 A heuristic procedure of incoherent sampling and CS reconstruction. A 1D sparse signal (a) is undersampled in its k -space domain (b). Equispaced undersampling generates signal ambiguity preventing recovery (d), while pseudo-random undersampling results in incoherent artefacts behaving like random noise (c). Some strong signal components can be detected by thresholding (e and f). The interference of these components can be then computed (h) and subtracted (g), enabling recovery of other weaker components. Taken from ¹¹⁸.

3.2.2 Requirements of compressed sensing

The successful application of CS has two basic requirements: the signal should be sparse in some transform domain(s), and the sampling matrix should be sufficiently incoherent.

Sparsity

An image is considered as sparse if it can be represented by a small number of non-zero coefficients, either in the image domain or in other sparsifying transform domains. The most commonly used sparsifying transforms for MRI are the discrete wavelet transform (DWT) and finite difference operations. Some advanced transforms have been proposed recently, such as the second-order total generalised variation (TGV) ¹¹⁹ and edge-guided compressed sensing (EdgeCS) ¹²⁰. The degree of sparsity is directly related to the maximal achievable acceleration factor (AF), and a high degree of sparsity is desired.

MR angiography is a typical example with high degree of sparsity, which is visible even in the image domain. Only the vessels have bright signal, and the background tissues are suppressed. The sparsity can be further improved by using sparsifying transforms.

Total variation

The first-order finite differences have been widely employed in CS reconstruction. The finite differences are often referred to as total variation (TV), which is the sum of the nearest neighbour differences that creates sparsity in an image I :

$$\text{TV}(I) = \sum_{i,j} \sqrt{\left|(\nabla_x I)_{i,j}\right|^2 + \left|(\nabla_y I)_{i,j}\right|^2} \quad (3.1)$$

TV minimisation is based on the assumption that the images are piecewise constant to some degree and exhibit a sparse representation after subtraction of adjacent pixels along the spatial dimensions¹²¹. The minimisation of TV can be regarded as attempting to find the ‘best’ edges in the image space⁹⁴ and thus is suitable for the problems where boundaries are the most important information¹⁰¹. MR angiograms show connected plateaus, clear boundaries and less complicated textures and should be ideal for the application of TV⁹⁴.

Sampling patterns

The aliasing interference in the sparse transform domain must be incoherent, *i.e.*, the undersampling artefacts must appear as noise-like patterns in the sparse domain. Sampling a completely random subset of k -space can guarantee a high degree of incoherence¹¹⁶. However, randomness in all dimensions of k -space is impractical, because the sampling trajectories along the readout direction need to be continuous and relatively smooth due to hardware and physiological considerations. Figure 3.2(a) and (b) shows random sampling patterns for 2D (k_x - k_y) and 3D (k_y - k_z) Cartesian acquisitions respectively. There is only freedom along the phase encoding direction for 2D imaging, but there are two dimensional degrees of freedom for 3D imaging. Figure 3.2(c) shows a typical pseudo-random Poisson-disk sampling pattern^{122,123} for 3D Cartesian acquisitions, which has been reported to improve image quality compared with purely random patterns (see Section 5.2.1). The detailed requirements in sampling pattern design will be discussed in Chapter 5.

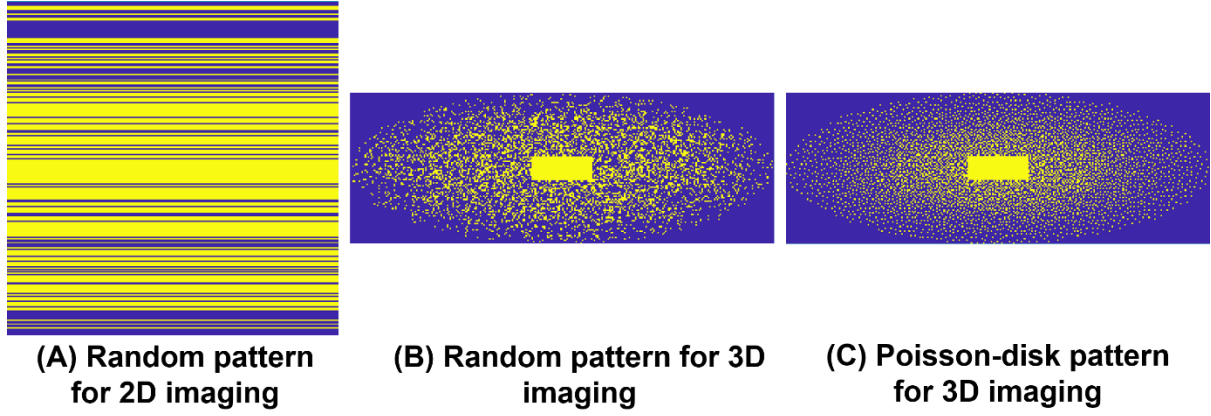


Figure 3.2 Typical MRI sampling patterns. (A) A random sampling pattern for 2D Cartesian acquisitions (k_x - k_y). (B) A random sampling pattern for 3D Cartesian acquisitions (k_y - k_z). (c) A pseudo-random Poisson-disk sampling pattern for 3D Cartesian acquisitions (k_y - k_z).

3.2.3 Problem formulation of compressed sensing

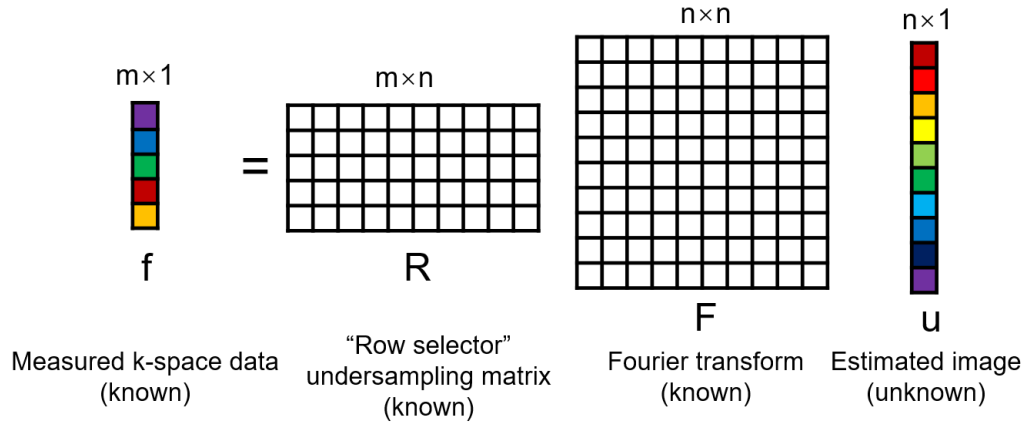


Figure 3.3 Compressed sensing sampling process with the undersampling matrix R and the Fourier transform F .

As shown in Figure 3.3, the compressed sensing problem can be mathematically expressed as a linear system of equations

$$f = RFu \quad (3.2)$$

where f is the measured k -space data ($m \times 1$), u is the image or image series to be reconstructed ($n \times 1$). A simplified 1D case is considered here. F is the Fourier transform operator ($n \times n$). The matrix R represents the undersampling matrix ($m \times n$), which is a “row selector” matrix comprising a subset of the rows of an identity matrix.

Ideally, u can be easily solved if $m = n$. However, as an undersampling matrix, $m \ll n$, which means the system is underdetermined, and there are infinitely many solutions.

According to the CS theory, if u is sparse, the problem can be solved by

$$\min \|u\|_1 \quad \text{s.t. } f = RFu \quad (3.3)$$

where $\|\cdot\|_1$ is the L1-norm, which calculates the degree of sparsity in the image by summing the absolute value of the pixels in the image.

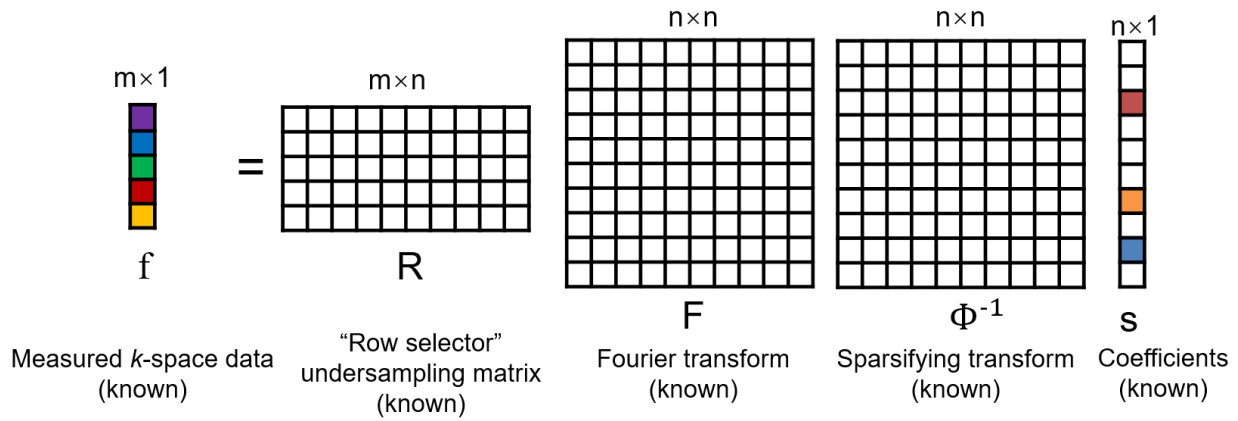


Figure 3.4 Compressed sensing sampling process with the undersampling matrix R , the Fourier transform F and a sparsifying transform Φ .

For MR images, u is not always sparse in the image domain but, as shown in Figure 3.4, we can find a sparsifying transform Φ , let $u = \Phi^{-1}s$,

$$f = RFu = RF\Phi^{-1}s \quad (3.4)$$

The problem can be solved by

$$\min_u \|\Phi u\|_1 \quad \text{s.t. } f = RFu \quad (3.5)$$

This constrained problem can be relaxed to an unconstrained Lagrange form using a quadratic penalty function:

$$u = \arg \min_u \|\Phi u\|_1 + \frac{\lambda}{2} \|RFu - f\|_2^2 \quad (3.6)$$

where $\|\cdot\|_2$ is the L2-norm calculating the least-squares difference.

The optimisation problem in this form can be solved with iterative algorithms such as conjugate gradient^{101,124,125}. The regularisation parameter λ controls the trade-off between the promotion of sparsity (L1-norm) and data consistency (L2-norm).

3.3 Split Bregman algorithm

3.3.1 Bregman iteration

For the unconstrained minimisation problem of equation 3.6, conventional algorithms can be expensive in time and computer memory¹²⁶. The Bregman Iterative Algorithm, introduced by Osher *et al.*¹²⁷, is an efficient algorithm that converges very quickly.

The Bregman iterative algorithm relies on the concept of “Bregman Distance”¹²⁸. The Bregman distance associated with a convex function $J(\cdot)$ between the point u and v is

$$D_f^p(u, v) = J(u) - J(v) - \langle p, u - v \rangle \quad (3.7)$$

where $p \in \partial J(v)$ is the sub-gradient in the subdifferential of $J(\cdot)$ at the point v . $D_f^p(u, v)$ is not a distance in the usual sense as it is not general symmetric, but it measures the closeness between u and v in the sense that $D_f^p(u, v) \geq 0$ and $D_f^p(u, v) \geq D_f^p(w, v)$ for a point w on the line segment connecting u and v . Figure 3.5 demonstrates the Bregman distance.

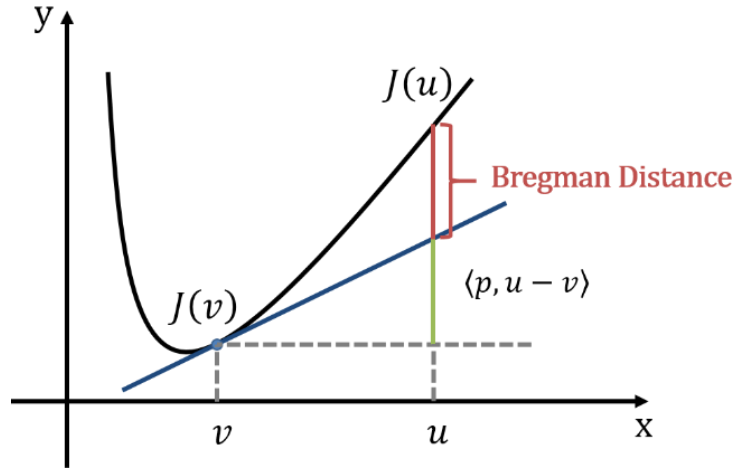


Figure 3.5 The Bregman distance associated with a convex function $J(\cdot)$ between the point u and v . $p \in \partial J(v)$ is the sub-gradient of $J(\cdot)$ at v .

Consider two convex energy functionals $J(\cdot)$ and $H(\cdot)$, and assume $H(\cdot)$ is differentiable, the associated unconstrained minimisation problem is

$$\min_u J(u) + \lambda H(u) \quad (3.8)$$

The Bregman iterative algorithm solves this problem by the following iterative procedure:

$$\begin{aligned} u^{k+1} &= \min_u D_f^{p^k}(u, u^k) + \lambda H(u) \\ &= \min_u J(u) - \langle p^k, u - u^k \rangle + \lambda H(u) \end{aligned} \quad (3.9)$$

$$p^{k+1} = p^k - \nabla H(u^{k+1}) \quad (3.10)$$

Consider the case $H(u) = \frac{1}{2} \|Au - b\|_2^2$, which is in the same form as the optimisation problem of CS (equation 3.6), the Bregman iteration is:

$$u^{k+1} = \min_u J(u) - \langle p^k, u - u^k \rangle + \frac{\lambda}{2} \|Au - b\|_2^2 \quad (3.11)$$

$$p^{k+1} = p^k - \lambda A^T (Au^{k+1} - b) \quad (3.12)$$

When A is linear, the unpleasant minimisation can be simplified to the following format according to ¹²⁹:

$$u^{k+1} = \min_u J(u) + \frac{\lambda}{2} \|Au - b^k\|_2^2 \quad (3.13)$$

$$b^{k+1} = b^k + b - Au^k \quad (3.14)$$

The term $b - Au^k$ can be regarded as the error or residual in the fidelity term. Therefore, the error is added back to the right-hand side of the equation during the iterative procedure, which is non-intuitive but effective.

3.3.2 Split Bregman

The optimisation problem can be solved efficiently by the Linearized Bregman Algorithm ^{129,130} or Fixed Point Continuation ¹³¹ when it is in the form of

$$\min_u \|u\|_1 + \frac{\lambda}{2} \|Au - b\|_2^2 \quad (3.15)$$

However, it is difficult for these algorithms to solve problems with an additional matrix in the L1-norm, such as the CS optimisation problem with a sparsifying transform (Φ in equation 3.6). Also, these schemes cannot solve optimisation problems involving multiple L1-regularisation terms.

The Split Bregman method proposed by Goldstein *et al.* ¹²⁶ can be used to solve the CS optimisation problem in the form of equation 3.6 ($\arg \min_u \|\Phi u\|_1 + \frac{\lambda}{2} \|RFu - f\|_2^2$). The L1 and L2 portions of the energy are “de-coupled” by rewriting equation 3.6 as:

$$\arg \min_u \|d\|_1 + \frac{\lambda}{2} \|RFu - f\|_2^2 \text{ such that } d = \Phi u \quad (3.16)$$

It can be converted into an unconstrained problem:

$$\arg \min_u \|d\|_1 + \frac{\lambda}{2} \|RFu - f\|_2^2 + \frac{\mu}{2} \|d - \Phi u\|_2^2 \quad (3.17)$$

By applying the Bregman iterative algorithm (equation 3.8 to 3.12) and the simplification (equation 3.13 and 3.14), the Split Bregman iteration is obtained:

$$(u^{k+1}, d^{k+1}) = \arg \min_u \|d\|_1 + \frac{\lambda}{2} \|RFu - f\|_2^2 + \frac{\mu}{2} \|d - \Phi u - b^k\|_2^2 \quad (3.18)$$

$$b^{k+1} = b^k + \Phi u^{k+1} - d^{k+1} \quad (3.19)$$

Because the L1 and L2 terms are now de-coupled, the minimisation of equation 3.18 can be performed iteratively with respect to u and d separately:

$$\text{Step 1: } u^{k+1} = \arg \min_u \frac{\lambda}{2} \|RFu - f\|_2^2 + \frac{\mu}{2} \|d - \Phi u - b^k\|_2^2 \quad (3.20)$$

$$\text{Step 2: } d^{k+1} = \arg \min_u \|d\|_1 + \frac{\mu}{2} \|d - \Phi u^{k+1} - b^k\|_2^2 \quad (3.21)$$

For Step 1, L2 norm is differentiable. By differentiating with respect to u and setting the result equal to zero, we get the update rule:

$$(\lambda F^T R^T R F + \mu \Phi^T \Phi) u^{k+1} = \lambda F^T R f + \mu \Phi^T (d^k - b^k) \quad (3.22)$$

Which can be written as:

$$u^{k+1} = F^{-1} K^{-1} F \cdot rhs^k \quad (3.23)$$

where $K = \lambda R^T R - \mu F \Phi^T \Phi F^{-1}$, $rhs^k = \lambda F^{-1} R f + \mu \Phi^T (d^k - b^k)$.

Step 2 does not have coupling between elements of d and can be solved by shrinkage operators¹²⁶:

$$d^{k+1} = \text{shrink} \left(\Phi u^{k+1} + b^k, \frac{1}{\mu} \right) \quad (3.24)$$

where $\text{shrink}(x, \gamma) = \frac{x}{|x|} \cdot \max(|x| - \gamma, 0)$.

To solve the constrained CS problem (equation 3.5), we need to replace f by f^k and use “double Bregman”. Firstly, the unconstrained problem is solved by performing “inner iterations”; then, the update rule is applied in the “outer iteration”. Putting all of these elements together, the Split Bregman algorithm for CS optimisation is shown in Table 3.1.

Table 3.1 A Split Bregman algorithm for the CS optimisation problem

| Split Bregman CS optimisation |
|---|
| <p>Inputs:</p> <p>f – k-space measurements</p> <p>R – undersampling matrix $f^{k+1} = f^k + f - RFu^{k+1}$</p> <p>$N$ – the number of inner iterations</p> <p>ε – stopping tolerance (estimated noise level)</p> |
| <p>Outputs:</p> <p>u^{k+1} – reconstructed image or image series</p> |
| <p>Algorithm:</p> <p>Initialise: $u^0 = F^{-1}f$, and $d^0 = b^0 = 0$</p> <p>While $\ RFu^k - f\ _2^2 > \varepsilon^2$</p> <p>For $i = 1$ to N</p> $u^{k+1} = F^{-1}K^{-1}F \cdot rhs^k$ $d^{k+1} = \text{shrink}\left(\Phi u^{k+1} + b^k, \frac{1}{\mu}\right)$ $b^{k+1} = b^k + \Phi u^{k+1} - d^{k+1}$ <p>end</p> $f^{k+1} = f^k + f - RFu^{k+1}$ <p>end</p> |

3.4 Parallel imaging and partial Fourier sampling

Parallel imaging (PI) and Partial Fourier (PF) sampling are another two routinely used acceleration techniques. Because CS, PI and PF sampling exploit different redundancies of MR images, they can be combined together to enable higher achievable acceleration rates^{101,132}.

3.4.1 Parallel imaging

PI is an acceleration technique that utilises multiple receive coil elements to reduce scan time in MRI. The known spatial sensitivities of receiver coils allow a reduction in the phase-encoding steps

during image acquisition enabling undersampling of k -space data below the Nyquist limit. PI has been in the mainstream of clinical imaging and can routinely offer scan time reductions of at least a factor of two and often more ⁹⁴.

A variety of PI methods have been developed. Methods like SENSE ¹³³ and SMASH ¹³⁴ require explicit coil sensitivities to be known beforehand. SENSE (SENSitivity Encoding) are among the most widely used PI methods. It is performed in image space after reconstruction of data from the individual coils. Basically, SENSE measures coil sensitivities by a calibration step and use them to remove the aliasing patterns in the images by solving an inverse problem with a set of linear equations.

In practice, measuring coil sensitivities accurately is difficult because even small errors in the sensitivity estimation can be amplified and result in visible artefacts in reconstructed image ¹³⁵. Auto-calibrating methods, such as GRAPPA ¹³⁶, ARC ¹³⁷, and auto-SMASH ¹³⁸, avoid these difficulties by implicitly deriving sensitivity information from the auto-calibration signal (ACS) region, which is a fully sampled region of the k -space centre acquired during the acquisition. Unlike SENSE, GRAPPA/ARC functions in k -space before Fourier transformation. It defines one or more reconstruction kernels that fit the sampling geometry, calibrates them from the ACS region (calculate weighting factors for each coil), and then uses them to estimate the missing data points.

3.4.2 SPIRiT

SPIRiT (iterative self-consistent parallel imaging reconstruction) ¹³⁹, proposed by Lustig *et. al.*, is another auto-calibrating method. Similar to GRAPPA, SPIRiT estimates linear relationships between multiple channels from auto-calibration signals and enforce that relationship to synthesise data values for unacquired samples. SPIRiT describes the reconstruction as an inverse problem governed by data consistency constraints. The reconstruction is formulated as an optimisation problem, which yields the solution with the highest consistency between the calibration and acquisition data.

$$\min_x \|(G - I)x\|_2^2 \quad \text{s.t. } f = Rx \quad (3.25)$$

where x is the k -space data to be reconstructed ($x = Fu$ in equation 3.4) and I is the identity matrix. G is a set of convolution operators that convolve the multi-coil data with the pre-calculated SPIRiT kernels:

$$x_i(r) = \sum_j g_{ij} \otimes x_j(U(r)) \quad (3.26)$$

where $x_i(r)$ is the k -space data at location r in the i -th coil, $U(r)$ denotes the neighbourhood around r , $x_j(U(r))$ is the data at the neighbourhood in the j -th coil, and g_{ij} is the corresponding SPIRiT kernel. It is based on the property that the k -space data at a specific location in a single coil is related to the data in a small neighbourhood of that location in all the coils, and this relationship remains the same for all spatial locations. For SPIRiT, the neighbourhood includes all the k -space points near $x_i(r)$ in all coils, whether they were acquired or not: this is different from GRAPPA, which only includes the acquired points.

The SPIRiT kernels are estimated from the ACS region by a calibration procedure, which looks for the kernels that are the most consistent with the calibration data in the least-squares sense:

$$\hat{g}_i = \arg \min_{g_i} \|Ag_i - x_i\|^2 \quad (3.27)$$

where $g_i = [g_{i1}, g_{i2}, \dots, g_{iN}]^T$ is a vector stacked by g_{ij} for all j , x_i is the data in ACS data in the i -th coil. Each row of A is the multi-coil data in the neighbourhood at a specific location reordered into a vector same as g_i .

3.4.3 L1-SPIRiT

SPIRiT can be combined with CS in an approach known as L1-SPIRiT^{87,140}. Based on equation 3.6 and equation 3.25, the corresponding reconstruction problem is formulated as:

$$x = \arg \min_x \|Rx - f\|_2^2 + \lambda \|\Phi F^{-1}x\|_{1,2} + \alpha \|(G - I)x\|_2^2 \quad (3.28)$$

where α is an additional regularisation parameter controlling the balance between data consistency and calibration consistency. The L1 penalty in equation 3.6 is replaced by a joint L1 norm ($\|\cdot\|_{1,2}$), which is a functional combining both the L1 and L2 norms:

$$\|u\|_{1,2} = \sum_r \sqrt{\sum_c |u_{rc}|^2} \quad (3.29)$$

where c is the coil index and r is the spatial index. While the L1-norm works along the voxel dimension, the L2-norm operates along the coil dimension to enforce joint sparsity along the coil dimension.

The L1-SPIRiT problem in equation 3.28 can be solved by iterative descent methods such as the conjugate gradient algorithm¹³⁹. As an alternative method, the equality constraint $(G - I)x = 0$ can be incorporated into the objective, such that the problem is formulated as simple least-squares¹³⁹. Let x_{nacq} represent only the missing points in k -space, and let G_{acq} and G_{nacq} be the part of the operator G that operates on the acquired and non-acquired points respectively. Equation 3.25 can be rewritten as

$$\arg \min_{x_{nacq}} \left\| (G_{nacq} - I)x_{nacq} + (G_{acq} - I)f \right\|_2^2 \quad (3.30)$$

It has the usual format of least-squares ($\|Ax - b\|_2^2$) and can be solved by projection over convex sets (POCS) iterations¹³⁹. By combining the POCS algorithm for SPIRiT with the Split Bregman algorithm for CS (Table 3.1), we developed a new L1-SPIRiT reconstruction algorithm, which is shown in Table 3.2. This algorithm will be employed in the acceleration studies in Chapter 5, 6 and 7.

Table 3.2 L1-SPIRiT reconstruction solved by Split Bregman and POCS

| Split Bregman and POCS iterations for the L1-SPIRiT reconstruction |
|---|
| <p>Inputs:</p> <p>f – k-space measurements</p> <p>R – undersampling matrix</p> <p>N – the number of inner iterations</p> <p>ε – stopping tolerance (estimated noise level)</p> <p>n_{acq} – indices of acquired k-space</p> <p>G – operator matrix obtained by calibration</p> |
| <p>Outputs:</p> <p>u^{k+1} – reconstructed image or image series</p> |
| <p>Algorithm:</p> <p>Initialise: $u^0 = F^{-1}f$, $x^0 = f$ and $d^0 = b^0 = 0$</p> <p>While $\ RFu^k - f\ _2^2 > \varepsilon^2$</p> <p> For $i = 1$ to N</p> <p> $x^k = K^{-1}Frhs^k$</p> <p> $x^{k+1} = Gx^k$</p> <p> $x^{k+1}[n_{acq}] = f$</p> <p> $u^{k+1} = F^{-1}x^{k+1}$</p> <p> $d^{k+1} = \text{shrink}\left(\Phi u^{k+1} + b^k, \frac{1}{\mu}\right)$</p> <p> $b^{k+1} = b^k + \Phi u^{k+1} - d^{k+1}$</p> <p> end</p> <p> $f^{k+1} = f^k + f - RFu^{k+1}$</p> <p>end</p> |

3.4.4 Partial Fourier sampling

PF sampling is based on the property that the Fourier transform of a purely real function has complex conjugate symmetry in k -space. In theory, this property enables us to acquire half of the k -space and reduce the acquisition time. In practice, PF acquisition samples slightly more than half of k -space so that a more accurate and robust phase correction can be provided.

Figure 3.6 shows the homodyne detection algorithm used for PF sampling reconstruction¹⁴¹. Firstly, a homodyne high-pass filter is applied to pre-weight the partial k -space data. The amplitude of the asymmetric portion of k -space data is doubled to compensate for the missing data. The high-pass filtered image I_H is then reconstructed from the pre-weighted data. Meanwhile, a low-resolution image I_L is acquired from the symmetric portion of k -space data by using a low-pass filter. Finally, the phase of I_H is corrected by the phase of the low-resolution image (ϕ_L), and the final image I is obtained by taking the real part of the result. This procedure can be expressed as

$$I = \text{Re}\{I_H e^{-i\phi_L}\} \quad (3.31)$$

PF can also be combined with CS and PI by either integrating a POCS PF-constraint into a joint PI and CS optimisation algorithm¹⁴² or designing a strategy incorporating all steps of PI, CS and PF into one scheme¹³². In the studies described in the following chapters, the combination of CS, PI and PF is achieved by replacing the inverse Fourier transform performed on the high-pass filtered data (denoted by * in Figure 3.4) by a joint PI-CS reconstruction algorithm.

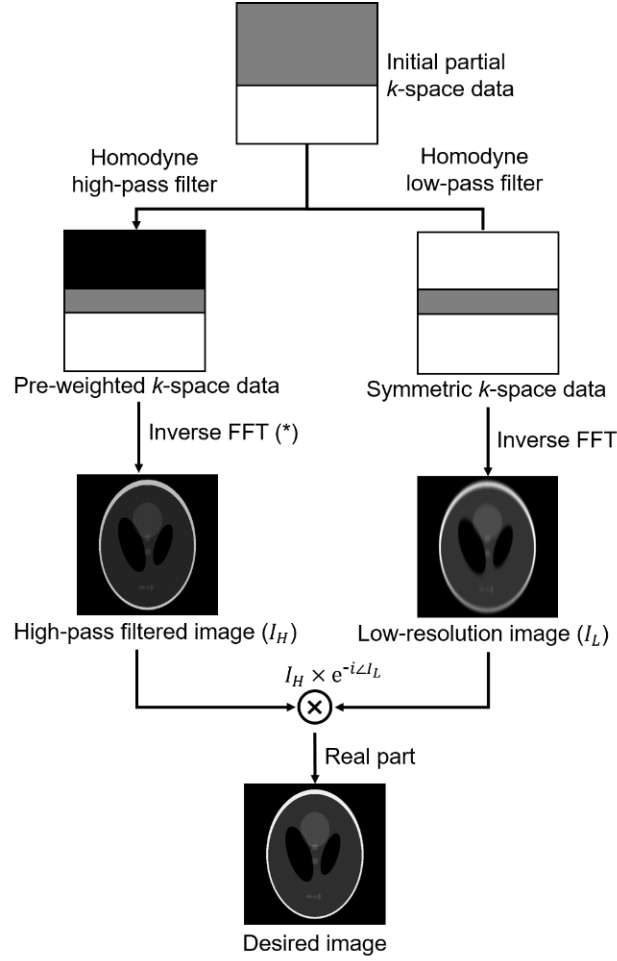


Figure 3.6 Flow chart summarizing the process of the homodyne algorithm for partial Fourier sampling reconstruction. * denotes the procedure that can be replaced by CS or PI reconstructions for sparsely undersampled data.

3.5 Quantitative evaluation metrics

Apart from the radiologists' visual evaluation, objective and quantitative metrics are important for evaluating the quality of reconstruction images. Such metrics can be valuable in the optimisation of reconstruction strategies. This section introduces the four quantitative metrics used in this thesis. Among them, peak signal-to-noise ratio (PSNR) and structural similarity (SSIM) are used to measure the difference between the reconstructed images and a set of gold standard images. They both require a full reference, which needs to be provided by fully sampled images. Contrast-to-

noise ratio (CNR) of artery-to-background can be calculated either with or without a full reference. Finally, an automatic sharpness evaluation method is developed as a no-reference matrix.

3.5.1 PSNR

PSNR, normalised mean square error (NMSE) or root mean square error (RMSE) are most commonly used quantitative metrics to evaluate reconstruction accuracy. All of them measure the squared intensity differences between the target images and the reference images, which are defined by

$$\begin{aligned} \text{MSE}(x, y) &= \frac{1}{m \times n \times s} \sum_{k=1}^s \sum_{j=1}^n \sum_{i=1}^m (x_{i,j,k} - y_{i,j,k})^2 \\ \text{RMSE}(x, y) &= \sqrt{\text{MSE}(x, y)} \\ \text{NMSE}(x, y) &= \frac{\text{MSE}(x, y)}{\text{MSE}(x, 0)} \\ \text{PSNR}(x, y) &= 10 \log_{10} \frac{\text{MAX}^2}{\text{MSE}(x, y)} \end{aligned} \quad (3.32)$$

In this thesis, x is the fully sampled reference 3D image set with the size of $m \times n \times s$, y is the image set reconstructed from the undersampled k -space data. MAX is the maximum possible pixel value of the images, which is 2^{15} for the signed 16-bit DICOM formatted images in our studies.

3.5.2 SSIM

SSIM is considered to be correlated with the quality perception of the human visual system and is effective for measuring the structural similarity between two images¹⁴³. Instead of measuring errors, SSIM is designed by modelling image distortion as a combination of three factors including loss of correlation, luminance distortion and contrast distortion¹⁴⁴. Local SSIM values for a window size of 8×8 pixels are calculated as:

$$\begin{aligned} \text{SSIM}(x, y) &= l(x, y)^\alpha c(x, y)^\beta s(x, y)^\gamma \\ &= \left(\frac{2\mu_x\mu_y + c_1}{\mu_x^2 + \mu_y^2 + c_1} \right)^\alpha \left(\frac{2\sigma_x\sigma_y + c_2}{\sigma_x^2 + \sigma_y^2 + c_2} \right)^\beta \left(\frac{\sigma_{xy} + c_3}{\sigma_x\sigma_y + c_3} \right)^\gamma \end{aligned} \quad (3.33)$$

where μ_x , μ_y , σ_x , σ_y , and σ_{xy} are the local means, standard deviations, and cross-covariance for local windows of image x , y . The parameters $\alpha > 0$, $\beta > 0$, and $\gamma > 0$, are used to adjust the relative importance of the three components. If $\alpha = \beta = \gamma = 1$ and $c_3 = c_2/2$, the index can be simplified to:

$$\text{SSIM}(x, y) = \frac{(2\mu_x\mu_y + c_1)(2\sigma_{xy} + c_2)}{(\mu_x^2 + \mu_y^2 + c_1)(\mu_x^2 + \mu_y^2 + c_2)} \quad (3.34)$$

The final SSIM index is the mean of all local SSIM values calculated by the formula above.

3.5.3 CNR of artery-to-background

For MRA, contrast-to-noise ratio of artery-to-background¹⁴⁵ can be used to evaluate the arterial signal intensity level. It is defined as the ratio of the signal difference between the artery and the other background tissues, against the noise level of the image. The formula is as follows:

$$\text{CNR} = \frac{S_{\text{artery}} - S_{\text{background}}}{\sigma} \quad (3.35)$$

where S_{artery} and $S_{\text{background}}$ are the mean arterial and background signal intensity (SI) values, σ is the noise level of the image. Arterial and background SIs are calculated by applying masks of arterial and background tissues. For the retrospective simulation studies with fully sampled reference angiograms (Chapter 5 and 6), σ is estimated by the standard deviation of the difference image (subtraction images of the reconstructed angiograms from the fully sampled reference angiograms). When reference angiograms are not available (Chapter 7), σ is estimated by the standard deviation of the region with no tissue signals, which is also obtained by applying a mask of noise area.

Figure 3.7 shows the process of generating masks. The leg mask and noise area masks (only for no-reference cases) are obtained from subtracted images and bright-blood images, while the artery mask is obtained from the subtracted angiograms. Masks are produced by applying a global threshold calculated by multiplying the maximum SI of the image set with a ratio. The background tissue mask is obtained by subtracting the artery mask from the leg mask.

Due to the high SI contrasts (arteries vs. background tissues in subtracted angiograms and the whole leg vs. regions with no signal in bright-blood images), threshold values are acceptable within a large durable range without tuning for each dataset. In our studies, the ratios for artery mask, leg mask and noise mask are 0.08, 0.01 and 0.005 respectively.

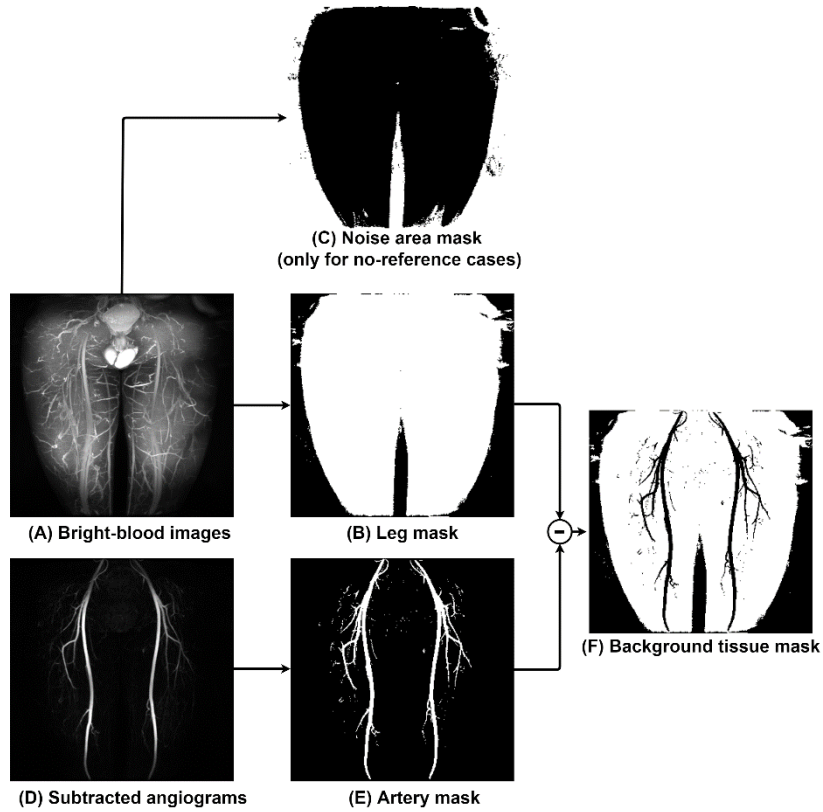


Figure 3.7 Diagram of the process of mask generation. The leg mask (B), noise area mask (C) and artery mask (E) are produced by hard thresholding. The background tissue mask is obtained by subtracting (E) from (B).

3.5.4 Sharpness

Edges in MR images carry physiologically important information and play a central role in image evaluation ¹⁴⁶. An undersampling scheme with imperfect reconstruction can result in the loss of high-frequency components, which can blur vessel edges. These blurred edges, although important for image quality and clinical diagnosis, do not have a significant impact on PSNR, SSIM and CNR values as they only represent a small fraction of a whole image. Therefore, a method for assessing the sharpness of edges is desired.

An automatic method based on curve fitting was developed to assess the sharpness of image edges. The flow chart of the method is shown in Figure 3.8. This method includes the following steps:

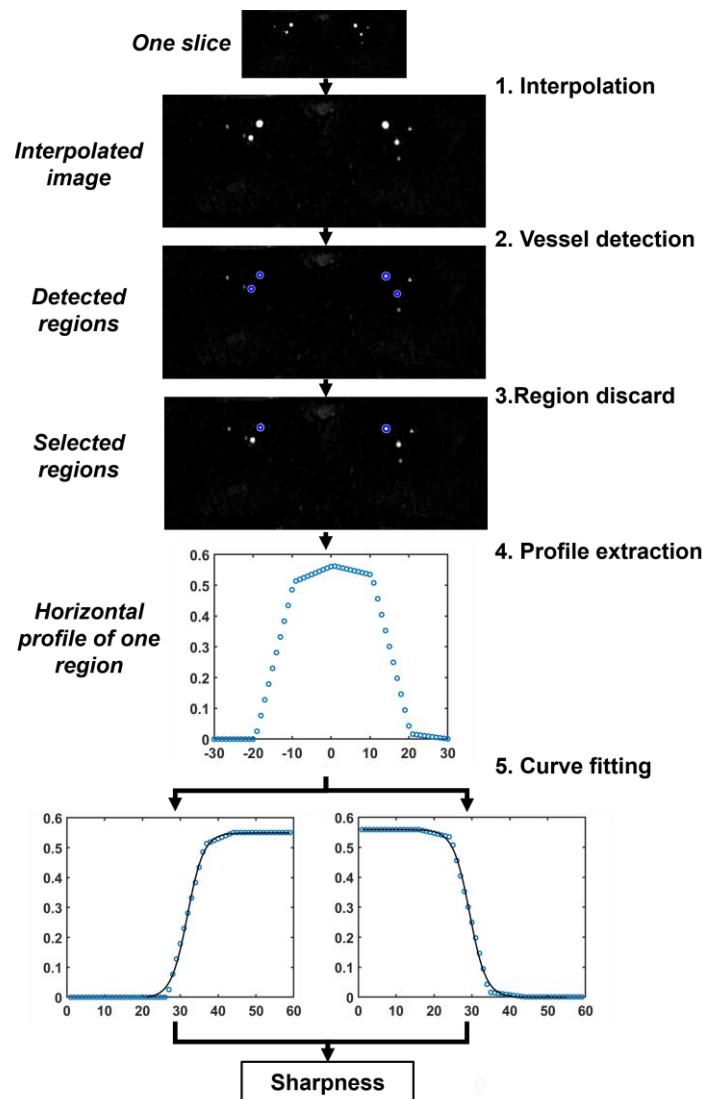


Figure 3.8 Flow chart of the sharpness evaluation process.

Interpolation

The diameters of arteries are normally small, approximately only three to five pixels. To improve curve fitting accuracy, images are firstly interpolated in y and z directions by a factor 10 using the bilinear interpolation. The output pixel value is a weighted average of pixels in the nearest 2-by-2 neighbourhood.

Vessel detection

Considering the arteries are circular on axial slices, arterial regions were detected on the individual axial slices by the circular Hough transform¹⁴⁷. In the following chapters, the typical range of radii for the detected circular objects was 15–28 pixels (matrix size of the slice of 320×80 before interpolation), and the sensitivity of the circle detection was 0.8.

Region discard

Arterial regions are discarded if the SIs of their edge pixels (the first and last points of horizontal and vertical profiles) are larger than a threshold value, which is 1/6 of the centre SI of the arterial region in our studies. All the regions are sorted according to their centre SI. Normally, over 300 regions can be detected in our studies. The 200 regions with the largest centre SI (across all the slices) are kept as the final detected arterial regions for each 3D dataset.

Profile extraction

Four 1D intensity profiles are extracted vertically and horizontally from each arterial region. The profiles are prolonged by 15 pixels at each end.

Curve fitting

Curve fitting is based on a method proposed by Ahmad *et al.*¹⁴⁶. Each intensity profile is individually fitted with a sigmoid function given by

$$f(\rho; a_0, a_1, a_2, s) = \frac{a_1}{1 + 10^{s(a_0 - \rho)}} + a_2 \quad (3.36)$$

where a_0 determines the centre location of the curve, a_1 determines the vertical range, a_2 defines the vertical offset, and s is the sharpness parameter quantifying the growth rate of the sigmoid. Figure 3.9 shows the sigmoid function for four different values of s .

Given a measured intensity profile $p(\rho)$, the sharpness parameter s can be estimated by

$$(\tilde{a}_0, \tilde{a}_1, \tilde{a}_2, \tilde{s}) = \arg \min_{a_0, a_1, a_2, s} \|\mathbf{p} - \mathbf{f}\|_2^2 \quad (3.37)$$

where \mathbf{p} and \mathbf{f} are vector forms of $p(\rho)$ and $f(\rho)$. As a nonlinear least-square solver, the trust-region-reflective algorithm¹⁴⁸ is used to find the coefficients to best fit the function.

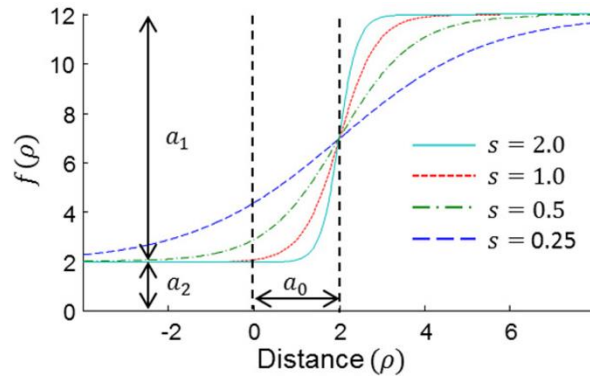


Figure 3.9 The sigmoid function for four different values of the sharpness parameter s . Taken from¹⁴⁶.

Overall sharpness

After the values of s are calculated for all the n regions, the sharpness of an image is finally defined as

$$Sharpness = 100 \cdot \frac{1}{n} \sum_{i=1}^n s(i) \quad (3.38)$$

3.6 Summary

This chapter provided the basis for the imaging acceleration studies in this thesis. Three acceleration techniques—compressed sensing, parallel imaging and partial Fourier sampling—were introduced and combined to form the basis of the reconstruction strategy. A reconstruction algorithm based on Split-Bregman and POCS-SPIRiT iterations was introduced, which will be employed in Chapters

5, 6 and 7. Four quantitative evaluation methods were introduced, which will be used for image quality evaluation in the following chapters.

Chapter 4. Improved background suppression using robust regression based weighted subtraction

4.1 Introduction

As described in Chapter 2, subtractive NCE-MRA is a class of techniques that acquires two image sets (dark-blood images (DBIs) and bright-blood images (BBIs)) with different vascular signal intensity (SI) which are later subtracted to generate angiograms. Typical subtractive NCE-MRA techniques include FSD^{59,60,78,149} and FBI^{79,80}, which have been introduced in Chapter 2.

In these conventional NCE-MRA techniques, the static background SIs from DBIs and BBIs should ideally be identical, leading to a complete absence of background signal in the subtracted images. However in practice, due to different imaging settings of the two acquisitions and the varying effective TR between the two acquisitions, some static background tissues show slightly different signal levels in BBIs and DBIs^{59,67–69,96,150–152}. For example, fat signal, if not sufficiently suppressed, can appear higher on BBIs for both FSD and FBI, leading to residual fat signal and stripe artefacts in the subtracted images^{59,66,150}. Muscle SI is normally higher on BBIs for FSD⁶⁸, but it could be slightly higher on DBIs for FBI^{96,151}. These residual background signals can potentially obscure the vascular signal of interest and affect clinical diagnosis. Venous contamination was also reported in FBI arteriogram^{67,68,152}, which can make angiographic interpretation challenging due to the close proximity of paired veins alongside peripheral arteries³.

Residual background signals can potentially be suppressed by using a weighted subtraction. Weighted subtraction has been used in some MRA techniques, such as MRA using SSFP¹⁵³, HOP-MRA¹⁵⁴ and interleaved double-echo MR angiography and venography¹⁵⁵, to maximise the blood-to-background contrast. However, the weighting factor was selected manually and empirically. Our initial investigations demonstrated that the weighting factor for the subtraction in FBI and FSD can be obtained adaptively and automatically by performing linear regression of the SIs^{68,69}. However, simple linear regression methods, such as ordinary least-squares regression (OLS) and principal component analysis (PCA), can be affected by outliers from vascular tissues such as the heart and large arteries^{68,69}. Also, some background tissues with high SI on the DBI and BBIs are not given

sufficient weighting in the regression procedure(s) to ensure that they are suppressed on the subtracted angiograms.

The purpose of this study is to develop robust regression methods to correct the SI difference of background tissues between the BBIs and DBIs and to improve the background suppression. Firstly, the signal levels of background tissues on BBIs and DBIs are evaluated in several different NCE-MRA techniques. Then, robust regression models, using iteratively reweighted least squares, are proposed to acquire the regression coefficient of the SI of background tissues on BBIs and DBIs—with the weighting function based on either the Euclidean distance or the deviation angle relative to the estimated regression line. Results from these two robust regression models, together with OLS, are compared with reference values subjectively determined by two observers over several different imaging sequences and in different vascular imaging areas.

4.2 Theory

4.2.1 Characteristics of residual signal

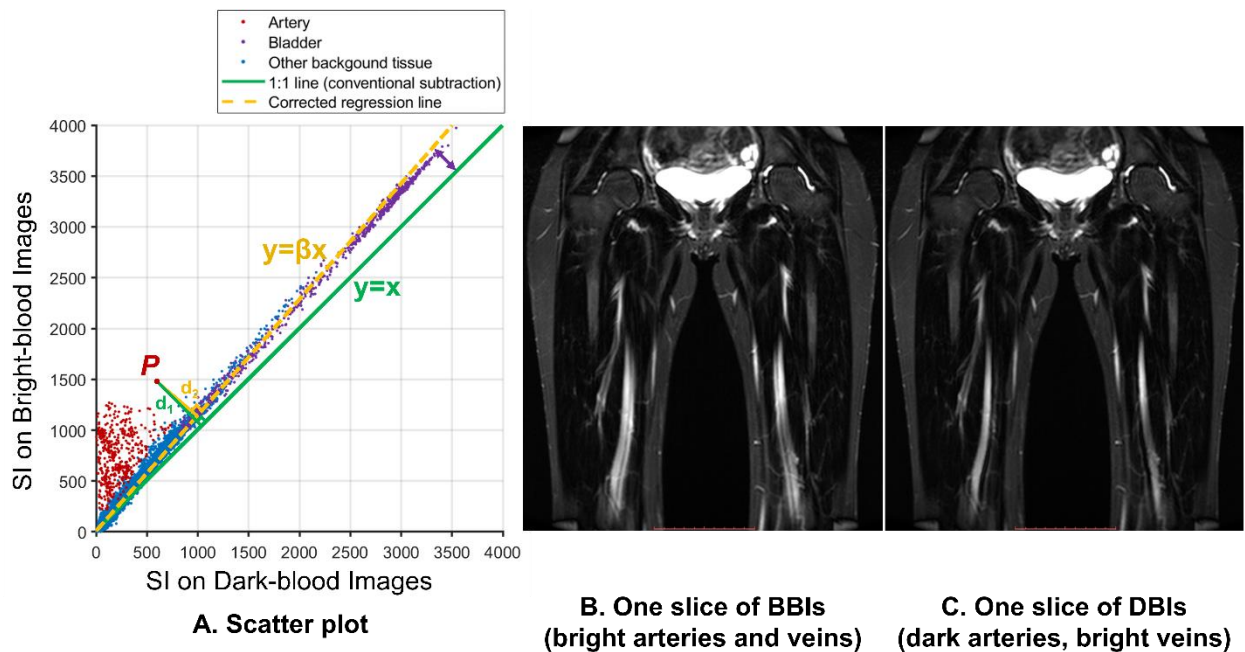
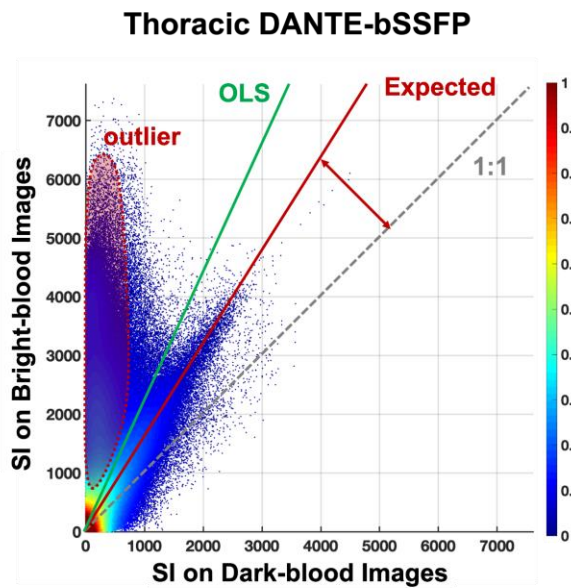


Figure 4.1 The scatter plot of the DBI and BBI SI for each pixel in one single slice (A) and the corresponding bright-artery (B) and dark-artery slice (C). The slice is selected from a femoral 3D FBI-MRA image set. The red points correspond to the artery signal, the purple points correspond to the bladder signal, and blue points

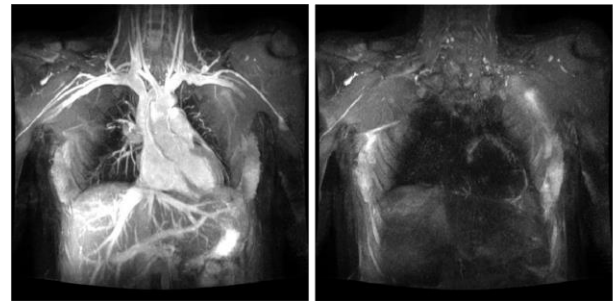
correspond to other background tissues such as veins and muscles. Using conventional direct subtraction (green line), the SI of pixel P on the subtracted angiogram is proportional to d_1 , while for the optimal subtraction (yellow line), the SI should be proportional to d_2 .

Figure 4.1 is the scatter plot of the SI of each pixel on DBIs versus the SI on BBIs for one single slice (3D femoral artery FBI). All the pixels were manually categorised into three anatomical types based on their anatomical location and intensity characteristics. It can be observed that the artery signal pixels are mainly located in the left of the scatter map, whereas the background tissue signal pixels distribute along a determined regression line $y = \beta x$. For conventional direct subtraction, the SI for a pixel P is obtained by subtracting its SI on DBIs from its SI on BBIs ($I_{Subtracted} = I_{Bright} - I_{Dark}$), which is proportional to the distance between the point P and the green line $y = x$ (line of unity) on the scatter plot (d_1). In many cases, the SIs of background tissues appear higher on BBIs than DBIs, which leads to residual background signal on subtracted angiograms, because there is still a considerable distance between the background pixel plot and the line of unity ($y = x$), particularly for background tissues with high SI such as the bladder.

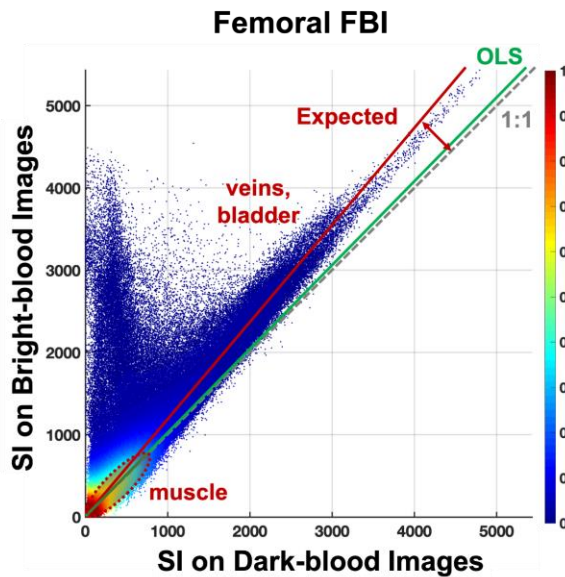
An alternative method which could weight the subtraction to the actual distributions of background signal intensities would be expected to improve the suppression of background tissues ($I_{Subtracted} = I_{Bright} - \beta I_{Dark}$, no offset was added along the y-axis in all the models used in this study). Using such a method, a regression line (yellow line) for background pixels should be used, and the distance to the regression line would then be d_2 instead of d_1 . Background tissue can thereby be reduced to close to zero, whereas the arterial signal would be less affected, as d_1 and d_2 of arterial pixels are very similar.



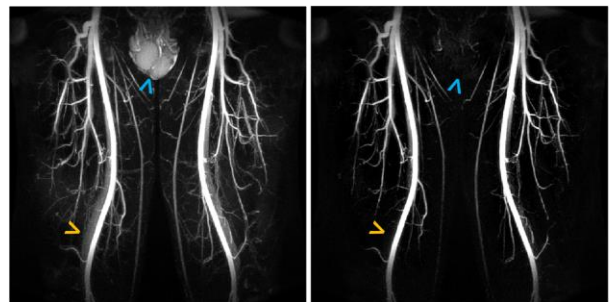
A



B



C



D

Figure 4.2 Two examples of thoracic 3D DANTE-bSSFP (A and B, both arteries and veins) and femoral 3D FBI (C and D, arteries only). A and C are scatter plots of the voxels from the whole 3D dataset with normalised density (the density of pixels is shown in coloured scale), B and D are the corresponding MIPs of original raw images, directly subtracted angiograms and expected angiograms with improved background

suppression. The green lines show the results of OLS, which fails to obtain the regression line of background voxels. The red lines are the expected results determined subjectively by manual selection.

Figure 4.2 shows two examples of scatter plots (A and C) with normalised density (shown in the colour scale) and the corresponding MIPs of original raw images, directly subtracted angiograms and expected angiograms with improved background suppression (B and D). A and B are from thoracic 3D FSD (DANTE-bSSFP, intended to show both arteries and veins)^{63,66}, and B and D are from femoral 3D FBI (intended to show arteries only). Reference angiograms with optimal background suppression and vascular visualisation were obtained by manual adjustment of the slope of the regression line to match the observed points on the scatter plot. Residual muscle signal (yellow arrowheads) can be observed on the direct subtracted thoracic FSD angiogram, while residual venous (yellow arrowheads) and testis signal (blue arrowheads) can be observed on direct subtracted femoral FBI angiograms.

The regression line can be obtained by different linear regression methods, but there are two key challenges to be addressed. The first challenge is the sensitivity to “outliers”. In some cases, such as thoracic MRA (Figure 4.2A & B), the presence of the heart leads to many flowing-blood pixels, which in the scatter plot lie in the region with high SI on BBIs and low SI on DBIs (red dashed region on Figure 4.2A). These points, which are considered as “outliers” in the linear regression, have large distances to the model prediction and thus would be given large weights in models like OLS or PCA⁶⁸. Therefore, the outliers would easily displace the regression line and generate an overlarge slope (green line in Figure 4.2A), leading to the loss of vascular signal. Secondly, the model may not be sensitive enough to pixels with high SI. In FBI (Figure 4.2C and D), muscle signal appears similar or even slightly lower^{96,151} on BBIs than DBIs. Its corresponding pixels lie in the region with low SI on both BBIs and DBIs (red dashed region on Figure 4.2C). In many cases such as femoral MRA, muscle is a much larger background component than other tissues and thus dominates the regression process, generating a relatively small regression coefficient (green line on C) for OLS. Therefore, the background tissues with high SI on both BBIs and DBIs, such as the bladder and veins, are not fully suppressed.

4.2.2 Robust regression

For OLS, the linear regression coefficient β can be solved by minimising the objective function which is given by

$$\beta_{OLS} = \arg \min_{\beta} \sum_{i=1}^n e_i^2 \quad (4.1)$$

where n is the number of samples and e is the error of estimation $e_i = y_i - x_i\beta$.

The OLS model assumes a Gaussian distribution of errors e_i . However, in the presence of outliers, the long-tail error distribution may lead to a biased estimate of the regression coefficient. Robust regression methods have been proposed to down-weight the influence of outliers by modifying the objective function, accommodating more general error distributions and reducing the sensitivity to the magnitude of the residuals. The most common general method of robust regression is M -estimator (the name comes from the maximum-likelihood estimation), which attempts to minimise the sum of a chosen function $\rho(\cdot)$ of the residual errors¹⁵⁶. The function $\rho(\cdot)$ gives the contribution of each residual to the objective function.

Formally defined, M -estimators are given by

$$\beta = \arg \min_{\beta} \sum_{i=1}^n \rho\left(\frac{e_i}{\tau}\right) = \arg \min_{\beta} \sum_{i=1}^n \rho\left(\frac{y_i - x_i\beta}{\tau}\right) \quad (4.2)$$

where τ is a scale parameter determined empirically by the median absolute deviation (MAD) estimator:

$$\tau = \text{median} \left| \varepsilon_i(\beta) - \text{median}(\varepsilon_i(\beta)) \right| / 0.6745 \quad (4.3)$$

where the constant 0.6745 makes the estimate unbiased for the normal distribution¹⁵⁷.

The function (4.2) is minimised by setting the first partial derivatives of $\rho(\cdot)$ with respect to β to zero, resulting in a nonlinear equation

$$\sum_{i=1}^n x_i \psi\left(\frac{y_i - x_i\beta}{\tau}\right) = 0 \quad (4.4)$$

where $\psi(e) = \rho'(e)$ is called the influence function. The weight function is now defined as

$$w(e) = \begin{cases} \psi(e)/e, & \text{if } e \neq 0; \\ 1, & \text{if } e = 0. \end{cases} \quad (4.5)$$

Once the format of the weighted function is chosen, the equation can be solved using a numerical method called iteratively reweighted least squares (IRLS), which iteratively estimates the weighted least squares fit. The steps are as follows:

1. Use the least-squares estimate β_{OLS} from equation (1) as initial estimates $\beta^{(0)}$
2. At each iteration t , calculate residuals $e_i^{(t-1)}$ and associated weights $w_i^{(t-1)} = w[e_i^{(t-1)}]$ from the previous iteration.
3. The new estimates of the regression coefficients are found using the matrix equation

$$\beta^{(t)} = [\mathbf{x}'\mathbf{W}^{(t-1)}\mathbf{x}]^{-1} \mathbf{x}'\mathbf{W}^{(t-1)}\mathbf{y} \quad (4.6)$$

where \mathbf{x} is the model column vector, with x_i as its i -th element, and $\mathbf{W}^{t-1} = \text{diag}\{w_i^{t-1}\}$ is the current weight matrix.

Repeat steps 2 and 3 until the estimated coefficients satisfy the converge criterion:

$$|\beta^{(t)} - \beta^{(t-1)}| < \sqrt{\varepsilon} \max(|\beta^{(t)}|, |\beta^{(t-1)}|) \quad (4.7)$$

where ε is the floating-point relative accuracy corresponding to the distance from 1.0 to the next largest floating-point number (2^{-52} for double precision and 2^{-23} for single precision).

4.2.3 Weight function

The selection of the weight function $w(\cdot)$ is the key to achieve robust regression for a specific problem. A typical function in M -estimation, the Welsch redescender¹⁵⁶ is used in this study, which is defined as:

$$\text{Welsch}(u) = \begin{cases} e^{-\left(\frac{u}{c}\right)^2} & \text{if } |u| < c \\ 0 & \text{if } |u| \geq c \end{cases} \quad (4.8)$$

$$c = 2.985$$

The tuning constant c gives coefficient estimates that have 95% asymptotic efficiency with respect to OLS at the Gaussian distribution¹⁵⁶. Further decreasing its value increases the downweight assigned to outlier points far from the regression line, and vice versa.

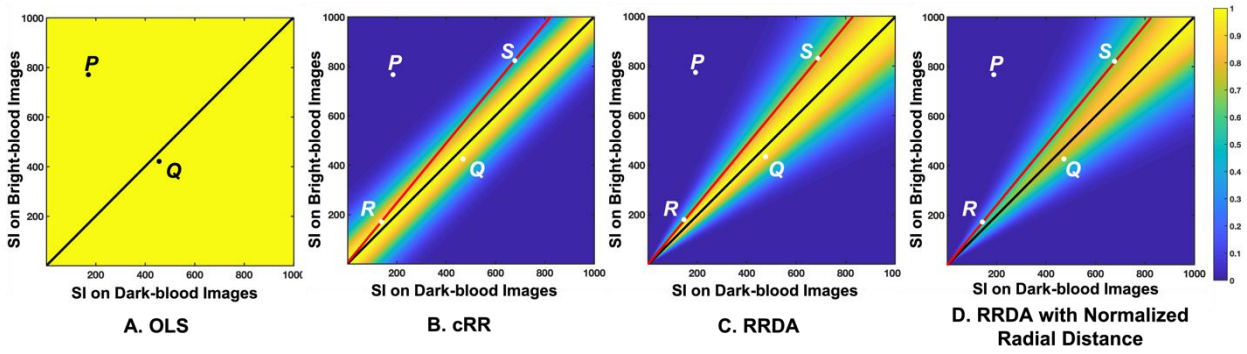


Figure 4.3 Weight maps of (A) OLS, (B) cRR, (C) RRDA and (D) improved RRDA ($\alpha=0.25$) when the current regression line is $y=x$. Point P is an example point far from the current regression line, and point Q is a point close to the regression line. Points R and S both locate on the red line and have the same deviation angle, but point S has a larger distance to the current regression line. All of the robust regression models down-weight points far from the model prediction (point P). RRDA gives the points with large SI (point S in comparison with point R) larger weights compared with cRR.

Figure 4.3 shows the weight maps of four weight functions investigated in this study. For OLS (or PCA), the weight function is $w=1$. The weights are the same everywhere on the scatter map (Figure 4.3A), such as point P and Q . In this case, point P has a much larger influence on the regression result due to its longer distance to the current regression line.

For conventional robust regression (cRR) based on the Euclidean distance to the estimated regression line (Figure 4.3B), the weight function is given by $w(e) = \text{Welsch}(e)$, where $e = y - x\beta$. The points far from the regression line (point P) are given much smaller weights than the points closer to the line (point Q), which reduces the impact of the outliers corresponding to the arterial

signal. However, cRR is not always effective at suppressing tissues with high SI on both BBIs and DBIs. For example, if the points of background tissues distribute along the line $y = \beta x$ ($\beta > 1$) (red line), for points R and S , although both are located on $y = \beta x$, point S has a larger distance to the regression line. Therefore, point S would generate a heavier residual signal on the subtracted image and should ideally be given greater emphasis in the determination of β . However, cRR determines the weight based on Euclidean distance and gives point S a smaller weight, making the model less sensitive to the points with large SI values.

A potential improvement would be to use the polar coordinate system, determining weights from the polar angle instead of Cartesian distance. For robust regression based on deviation angle (RRDA), the weight function is given by $w(\theta) = \text{Welsch}(\theta)$, where θ is the deviation angle to the regression line given by

$$\theta = \arctan\left(\frac{y}{x}\right) - \arctan(\beta) \quad (4.9)$$

The contribution of high-SI points can still be too low due to their relatively small number in comparison with low-SI points corresponding to muscle and background air. Therefore, the radial distance r can be used to further increase its sensitivity to points with large values:

$$w(\theta, r) = \text{Welsch}(\theta(\beta)) \cdot \left(\frac{r}{r_{\max}}\right)^\alpha \quad (4.10)$$

where $\theta(\beta) = \arctan\left(\frac{y}{x}\right) - \arctan(\beta)$ and $r = \sqrt{x^2 + y^2}$, α is a parameter controlling the influence of the normalised radial distance. It can be observed that point S has the same weight as R on Figure 4.3C and outweighs R on Figure 4.3D. This improved version of RRDA was used for the evaluation in this study.

Table 4.1 summarises the weight functions and characteristics of different regression methods mentioned above.

Table 4.1 The weight functions and characteristics of different regression methods

| Regression methods | Weight function | Robustness to outliers | Sensitivity to high-SI points |
|--------------------|--|------------------------|-------------------------------|
| OLS/PCA | $w = 1$ | Low | Medium |
| cRR | $w(e) = \text{Welsch}(e)$, where $e = y - x\beta$ | High | Low |
| RRDA | $w(\theta) = \text{Welsch}(\theta)$ $\theta = \arctan\left(\frac{y}{x}\right) - \arctan(\beta)$ | High | Medium |
| improved RRDA | $w(\theta, r) = \text{Welsch}(\theta(\beta)) \cdot r^\alpha$ where $\theta = \arctan\left(\frac{y}{x}\right) - \arctan(\beta)$ and $r = \frac{\sqrt{x^2 + y^2}}{r_{\max}}$ | High | High |

4.3 Methods

4.3.1 Study population and imaging protocols

Multiple datasets with differing NCE-MRA acquisition techniques were used in this study, including 36 coronal thoracic FSD-MRA datasets (DANTE-bSSFP)^{63,66} from 16 healthy volunteers and 12 patients with central venous obstruction or restricted venous access; 26 coronal femoral FBI-MRA (ECG-gated FSE) datasets from 17 healthy volunteers; and 13 coronal iliac FSD-MRA datasets (3 DANTE-bSSFP, 7 iMSDE-bSSFP^{59,60}, 3 iMSDE-FSE¹⁵⁸) from 6 healthy volunteers and 2 patients. The acquisition protocols are listed in Table 4.2.

All the images were acquired using 1.5 T MRI systems (Discovery MR450 or Optima MR450w; GE Healthcare, Waukesha, WI). Studies were approved by the local research ethics committee, and all participants gave informed consent.

4.3.2 Model parameters

In this study, OLS, cRR and RRDA methods were evaluated on all the datasets. In RRDA, we adopted $\alpha=1$ for femoral FBI, which has a large number of muscle voxels with low SIs, and $\alpha=0.5$ for thoracic and iliac MRA images.

The 3D datasets in this study have a large number of voxels ($8.4 \times 10^6 - 1.4 \times 10^8$), resulting in a large computational burden for real-time online processing. Therefore, a subset of voxels was randomly sampled for regression to increase computational efficiency. In a pilot study, we evaluated the performance of using different amounts of the randomly sampled data in all the datasets. The number of sampled voxels was increased from 2^{10} to 2^{23} , multiplying by 2 in each step, and the error between the results of partial data and full data was calculated. It was found that when the sampled voxels were larger than 2^{17} (131,072), the mean error in the regression coefficient due to this subsampling reduced to less than 0.01, which is visually undetectable on the intensity corrected angiograms. Therefore, the number of sampled voxels was fixed to 5×10^5 (500,000) for all datasets in this study. This corresponded to sampling ratios of 1.15%, 4.88% and 3.70%, and an estimated mean error of 0.0017, 0.0023 and 0.0017 in the regression line slope for femoral FBI, thoracic FSD and iliac FSD respectively. Compared with using full data, the use of partial data reduced the

average computation times of femoral FBI, thoracic FSD and iliac FSD data from 55.2, 20.2 and 30.0 seconds to 0.9, 0.6 and 1.0 seconds respectively (4-Core 3.4 GHz CPU and 16 GB RAM).

4.3.3 Image assessment

The background SI difference between BBIs and DBIs was evaluated on vascular study images using different imaging sequences. The SIs of specific background target tissues, such as muscle, liver, bladder, testis and veins (only on arteriograms) were measured on BBIs and DBIs. Matched ROIs were drawn in representative regions of target tissues on the individual raw images before subtraction. One ROI was drawn on three selected slices for each dataset and for each background tissue. The slices were selected randomly but with the requirement of a large coverage of target tissues. The mean value of each background tissue was calculated for each dataset.

The calculated regression coefficients were compared with reference values determined by two trained observers with more than four years' experience in vascular MRI. Subjective manual determination of regression coefficients was performed based on both MIPs of subtracted images and scatter plots, using an interactive graphical interface developed in MATLAB (R2019a, Mathworks Inc., Natick, MA). Manually assessed optimal regression coefficients were determined by two observers independently based on the following method: the regression line was first positioned in the centre of the distribution of background signal voxels on the scatter plot and then adjusted to achieve optimal background signal suppression without impairing vascular signal on the MIP. The reference regression value was taken as the mean of the two manually determined optimal regression coefficients.

The results obtained by each regression model were compared with the reference values over different subjects using a paired, two-sided Student *t*-test. Pearson product-moment correlation analysis and Bland-Altman analysis were also used to evaluate the agreement between the results of each regression method and the reference values. A P-value <0.05 was considered statistically significant.

SI ratios of background tissue to vascular signal were also calculated for images obtained by direct subtraction and RRDA. SIs were measured from matched ROIs drawn in representative regions in the target tissues on the MIPs of subtracted images. For FBI-MR arteriography, two vascular ROIs were drawn in the lumen regions of arteries for each MIP; for FSD-MRA visualising both arteries

and veins, one vascular ROI each was drawn from the lumen regions of arteries and veins respectively, and their mean value used as the vascular SI. Two ROIs were drawn for each type of background tissue, and the mean values were calculated for each dataset.

Table 4.2 Parameters used for thoracic FSD, iliac FSD and femoral FBI.

| Area | Imaging target | Imaging sequence | Dataset number | Subject number, gender and age | Parameters |
|----------|-----------------|------------------|----------------|--|---|
| Thoracic | artery and vein | 3D DANTE-bSSFP | 36 | 16 volunteers (8 men and 8 women) and 12 patients (6 men and 6 women; age range 19–81 years) | <p>Bright- and dark-blood acquisitions are sequential and had the same cardiac trigger delay and acquisition window.</p> <p>Free-breathing acquisitions using navigator gating (without slab-tracking, acceptance window 3–4 mm).</p> <p>Fat suppression: dual inversion-recovery (DIR) ⁶⁶. This aims to suppress fat but with reduced residual suppression of the blood signal by the short-time inversion recovery (STIR) pulse for short TR.</p> <p>Bright- and dark-blood acquisitions have the same cardiac trigger delay and acquisition window. DANTE: TR 1 ms, flip angle 10°, gradient 20 mT/m, echo train length (ETL) 150–270 pulses.</p> <p>bSSFP: acquisition matrix 256×256, acquisition slice number 32–56, slice thickness 4, FOV 400; R-R interval 2/3; flip angle 65°, TE/TR=1.0/2.7 ms, bandwidth ±125 kHz, acquisition window 115 ms. Each plane of <i>k</i>-space was acquired over two shots. Acquisitions accelerated by PI (array spatial sensitivity encoding technique, ASSET) with an acceleration factor of 3 in the phase-encoding direction.</p> |
| Iliac | artery and vein | 3D DANTE-bSSFP | 3 | 6 volunteers (5 men and 1 women) and 2 patients (2 men, 52 years and 75 years old) | <p>Bright- and dark-blood acquisitions were interleaved and had the same cardiac trigger delay and acquisition window.</p> <p>DANTE: TR 1 ms, flip angle 10°, gradient 20 mT/m, ETL 150–270 pulses; iMSDE: duration 4 ms, amplitude 6 mT/m, placed at the time of approximately peak venous flow within the cardiac cycle.</p> |
| | | 3D iMSDE-bSSFP | 7 | | <p>Acquisition parameters for both bSSFP and FSE: acquisition matrix 256×256, acquisition slice number 44–72, slice thickness:2.4, FOV 340–380; R-R interval 2–3. Fat suppression: DIR.</p> |
| | | 3D iMSDE-FSE | 3 | | <p>bSSFP: flip angle 65°, TE/TR=1.2/3.1 ms, bandwidth: ±125 kHz, acquisition window 198 ms. Each plane of <i>k</i>-space was acquired over two shots. ASSET factor 2.</p> <p>FSE: acquisition slice number 36–40, slice thickness 2.4 mm, FOV 340–360; TE_{eff}62 ms, bandwidth ±83.3 kHz, ETL 64, echo spacing 3.1 ms, acquisition window 198 ms. Acquisitions accelerated by PI (Autocalibrating Reconstruction for Cartesian sampling, ARC) with an acceleration factor of 2 and half Fourier in the phase-encoding direction.</p> |
| Femoral | artery | 3D FBI | 26 | 17 volunteers (11 men and 6 women) | <p>Systolic and diastolic acquisitions were interleaved, and their trigger delay times were 220ms and 500–1000ms respectively.</p> |

| | | | | | |
|--|--|--|--|-------------------------------|---|
| | | | | women; age range 24–45 years) | <p>Fat suppression: STIR with an inversion time of 174 ms.</p> <p>FSE: acquisition matrix 224×224–384×384, acquisition slice number 80, slice thickness 1.8–2 mm, FOV 400–440; TR=2–3 R-R intervals, TE_{eff} 30–60 ms, bandwidth ±62.5–83.3 kHz, ETL 60–80, echo spacing 3.6–4.6 ms, acquisition window 216–294 ms; accelerated by SPIRiT¹³⁹, PF and CS (overall acceleration factor 6–10, with a variable-density Poisson disk sampling pattern).</p> <p>Variable flip angles⁸¹ (start from 105° and increase to 180° for the systolic acquisition; constant 180° for the diastolic acquisition) and flow-spoiled gradients (10% of one-half the area of the readout gradient for both systolic and diastolic acquisitions)⁸⁰ were both used to increase flow sensitivity.</p> |
|--|--|--|--|-------------------------------|---|

4.4 Results

4.4.1 Signal level of static tissues on BBIs and DBIs

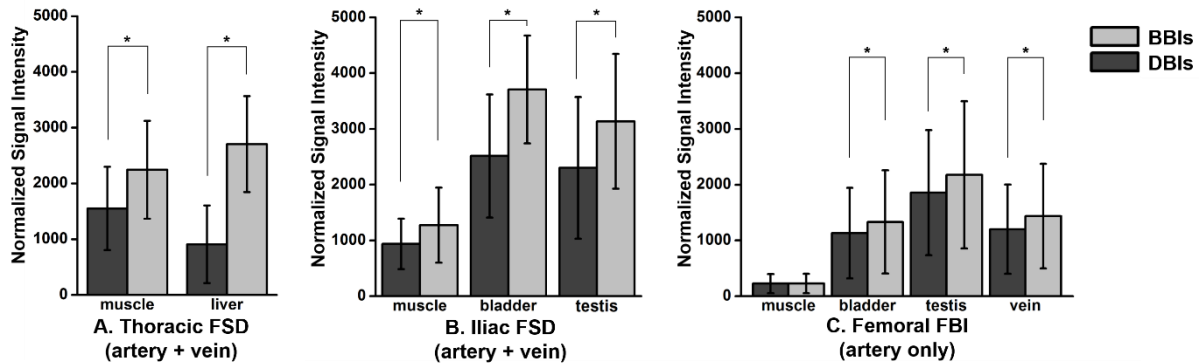


Figure 4.4 Signal level of background tissues in BBIs and DBIs in thoracic FSD (A), iliac FSD (B) and femoral FBI (C). Asterisk (*) indicates significance at $P < 0.05$ level. Signal levels are significantly lower on DBIs in all cases except for the muscle signal in femoral FBI.

Figure 4.4 shows the signal levels of representative static tissues on DBIs and BBIs in the different study populations. SI differences can be observed in all these tissues, especially for organs containing plenty of water such as bladder and liver. The signal levels of most static tissues are significantly higher on BBIs than DBIs ($p < 0.05$), leading to residual background signal on the subtracted angiograms. However, for femoral FBI, there is no significant difference between the muscle SI on BBIs and DBIs, which can bias the regression towards the distribution of other tissues such as bladder and veins.

4.4.2 Example images

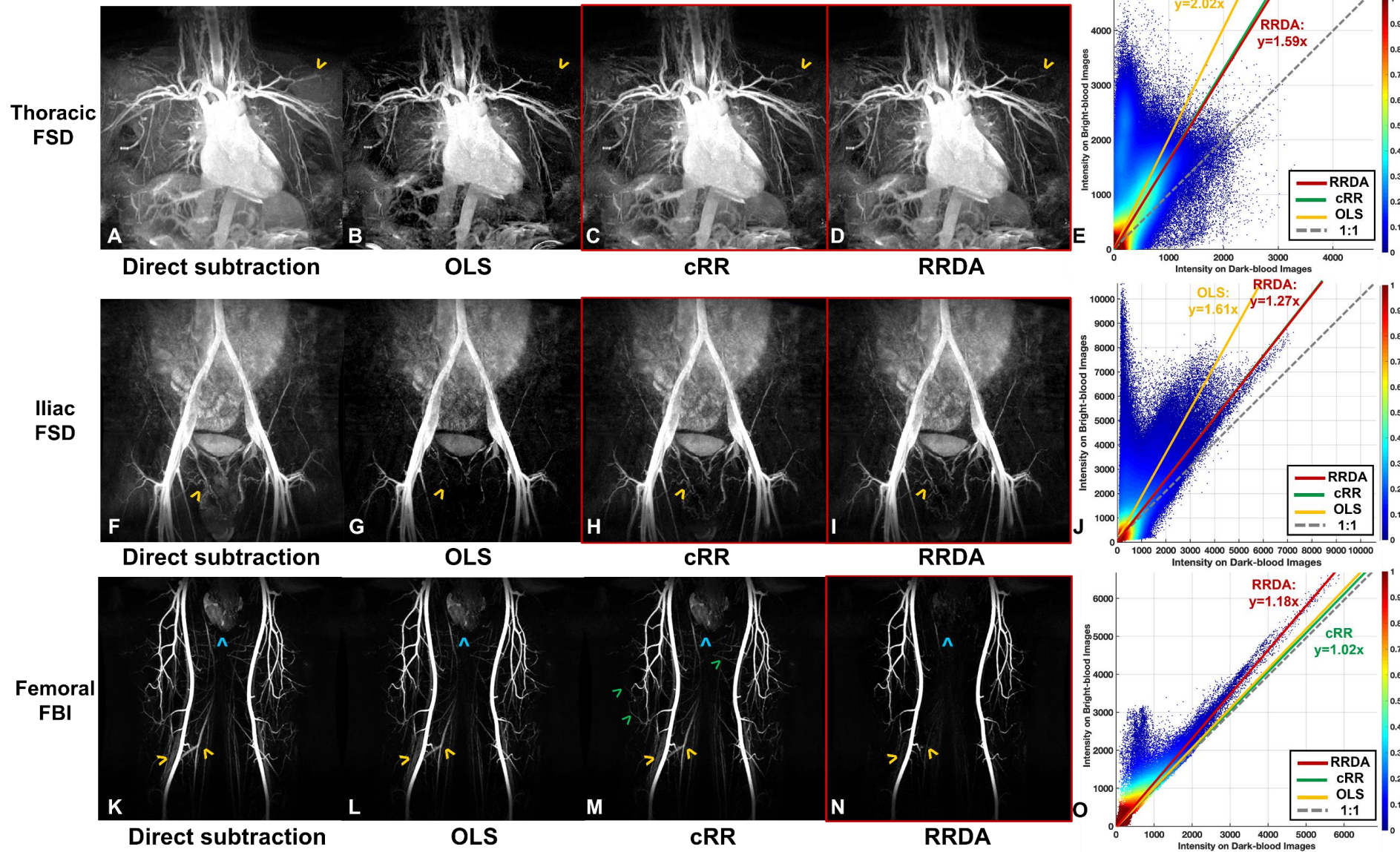


Figure 4.5 Example MIPs and the corresponding scatter plot of thoracic 3D DANTE-bSSFP (A–E), iliac 3D iMSDE-FSE (F–J) and femoral 3D FBI (K–O). The grey dashed lines on the scatter plots are the 1:1 line for the direct subtraction; the yellow, green and red solid lines are the regression lines estimated by OLS, cRR and RRDA respectively. The red boxes denote the regression results that agree most closely with the reference value. The arrowheads on MIPs denote the suppressed background tissue signal. The green arrowheads on M denote small venous branches which are easily confused with arterial branches but can be suppressed by RRDA. RRDA had good regression results in all the three cases. OLS generated an overlarge regression coefficient in thoracic and iliac FSD, which led to signal loss in small vessels. cRR failed to suppress the residual background signal in femoral FBI, but agreed with RRDA in the other cases.

Figure 4.5(A–E) shows an example result of thoracic FSD-MRA (DANTE-bSSFP) from a patient with central venous obstruction. The performance of RRDA is compared with OLS and direct subtraction. OLS (yellow solid line on E) was affected by outliers and overestimated the regression coefficient, leading to signal loss in small vessels (arrowheads on A to D). In contrast, both RRDA and cRR generated the correct regression line (red and green solid line on E) and thus suppressed residual muscle signal while preserving the blood signal (C and D). Similar results can be found in F–J showing an example of iliac iMSDE-FSE from a healthy volunteer.

Another example of femoral FBI is shown in Figure 4.5(K–O). The regression in cRR and OLS was dominated by the muscle voxels with a large number of voxels and low SI: their regression coefficients were insufficient to suppress veins (yellow arrowheads on L and M) or background tissues (blue arrowhead on L and M). RRDA was less sensitive to the muscle voxels (red solid line on J): background tissues such as testis (the blue arrowhead on N) and veins (yellow arrowheads in N) were suppressed, while the arterial signal is preserved. Note that some small vessels denoted by the green arrowheads on M are actually veins, which can be easily confused with arterial branches but can be suppressed by RRDA.

4.4.3 Quantitative analysis

Table 4.3 Comparison of mean regression coefficients calculated by different regression methods versus the reference values.

| Imaging Sequence | Statistics | OLS | cRR | RRDA | Reference values |
|------------------|---------------------|--------------|--------------|--------------|------------------|
| Thoracic FSD | Mean coefficient | 1.80±0.21 | 1.49±0.15 | 1.49±0.15 | 1.50±0.15 |
| | Bias | 0.293±0.153 | -0.012±0.051 | -0.007±0.056 | - |
| | P-value | <0.05 | 0.16 | 0.48 | - |
| | Mean absolute error | 0.293 | 0.039 | 0.038 | - |
| | Pearson r value | 0.69 | 0.94 | 0.93 | - |
| Femoral FBI | Mean coefficient | 1.08±0.05 | 1.04±0.05 | 1.13±0.05 | 1.13±0.05 |
| | Bias | -0.043±0.034 | -0.089±0.041 | 0.004±0.014 | - |
| | P-value | <0.05 | <0.05 | 0.22 | - |
| | Mean absolute error | 0.047 | 0.089 | 0.012 | - |
| | Pearson r value | 0.75 | 0.62 | 0.96 | - |
| Iliac FSD | Mean coefficient | 1.25±0.10 | 1.20±0.07 | 1.18±0.08 | 1.21±0.06 |
| | Bias | 0.036±0.022 | -0.013±0.027 | -0.026±0.034 | - |
| | P-value | 0.12 | 0.10 | 0.05 | - |
| | Mean absolute error | 0.062 | 0.025 | 0.036 | - |
| | Pearson r value | 0.40 | 0.92 | 0.92 | - |

Bias, *P*-values, mean absolute errors and Pearson *r* values are between automatic regression results and the reference values.

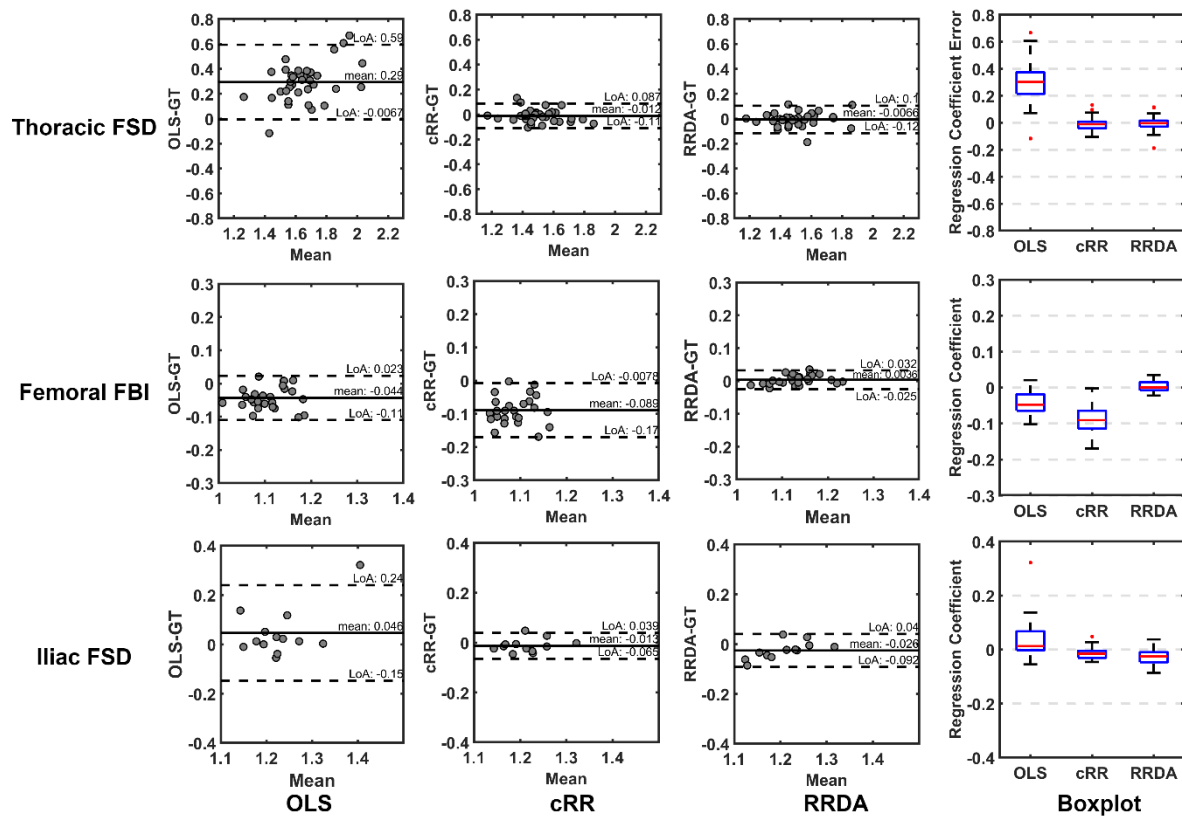


Figure 4.6 Bland-Altman plots and boxplots comparing the regression results of OLS, cRR and RRDA.

The statistical analysis results are listed in Table 4.3. Figure 4.6 shows the Bland-Altman plots and boxplots comparing the performance of different regression methods for different types of images. The iliac datasets using different sequences were categorised into one category due to their similar image characteristics and regression results.

OLS has high mean absolute errors and low correlation coefficients in all the three image types. In particular, due to its sensitivity to outliers, OLS tends to overestimate the regression coefficients in thoracic FSD, leading to a large bias of 0.275 and also large variation. cRR is more resistant to outliers. It has excellent performance in thoracic and iliac FSD. However, cRR has a bias of -0.089 in femoral FBI. The regression coefficients of cRR are smaller than the reference values in all the femoral FBI datasets evaluated in this study. RRDA achieved accurate and robust results in all the three types of images, with small bias, small mean absolute error and high correlation coefficients. No significant differences were found between the RRDA results and reference values for any of the three methods.

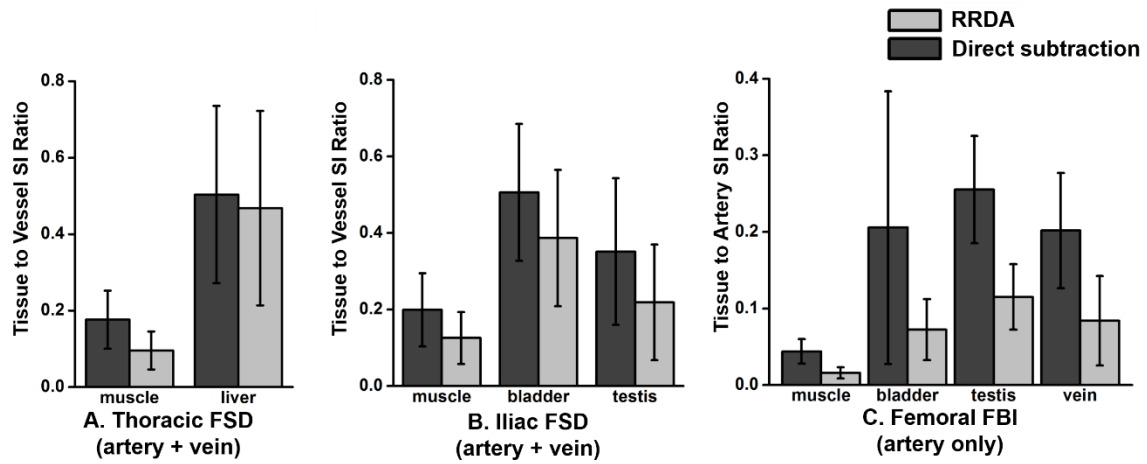


Figure 4.7 Comparison of the tissue-to-artery/vein SI ratios between RRDA and direct subtraction in thoracic FSD (A), iliac FSD (B) and femoral FBI (C). Statistically significant differences can be observed in all the cases ($P < 0.05$).

A comparison of the tissue-to-vessel SI ratios between RRDA and direct subtraction is shown in Figure 4.7. In thoracic FSD, the muscle and liver to vessel SI ratios in RRDA reduced to 54.4% and 93.0% of their values in direct subtraction respectively; in iliac FSD, the muscle-, bladder- and testis- to-vessel SI ratios reduced to 63.1%, 76.5% and 62.2% respectively; in femoral FBI, the muscle-, bladder-, testis- and vein-to-artery SI ratios reduced to 36.0%, 35.2%, 45.1% and 41.5% respectively.

4.5 Discussion

This study has developed a robust regression method to compensate for the SI differences of static background tissues between BBIs and DBIs in subtractive NCE-MRA. Signal level differences were found in almost all the static tissues for the subtractive NCE-MRA techniques investigated in this study. These differences lead to residual background signal when using direct subtraction, but this residual signal can be substantially reduced by using weighted subtraction, if an appropriate weighting factor is determined, corresponding to the regression coefficient between the background tissue signals.

FSD produces dark-blood images by using flow-sensitive preparation modules to suppress blood with fast flow. Although these modules are velocity-dependent, they can still impair the signal level of static residual background tissues. With MSDE or iMSDE, some static signal loss is inevitable, resulting from inherent T_2 decay, T_1 steady-state decay¹⁵⁹, diffusion, eddy currents

from crusher gradients and imperfections in the 180° pulses due to B_1 inhomogeneities. DANTE pulse trains cause a spoiling effect in flowing spins and suppress their signal. Static spins may form a steady state but still experience some signal decay compared with their initial states. The signal loss can be more serious when eddy current effects distort the gradient waveforms and thus impair the phase preservation of the static signal ¹⁵⁹.

FBI attenuates flowing spins due to the flow dephasing and flow void effect of the FSE sequence. Variable flip angles ⁸¹ or spoiling gradients ⁸⁰ are normally employed to increase its sensitivity to blood flow velocity. Unfortunately, both of these approaches can also slightly reduce the signal from background tissues containing water or blood, such as veins, bladder and testis. The SI differences between BBIs and DBIs can be more serious when the variable flip angles and flow-spoiled gradients are only employed in systolic acquisitions.

Another factor leading to the background SI difference is the varying TRs of systolic and diastolic acquisitions ^{67,151}, which may be caused by two effects. First, the FBI sequence in this study uses an interleaved black/bright-blood acquisition, which alternates between bright- and dark-blood acquisitions in consecutive heartbeats. Since the diastolic acquisition has a longer trigger delay, *i.e.*, a longer period of T_1 recovery, background tissues would have slightly higher SI on the diastolic images than the systolic images. This is especially obvious for tissues with a long T_1 and T_2 such as the bladder, as their signals are not fully recovered within a TR of 2 or 3 R-R intervals and thus greatly fluctuate between BBIs and DBIs. The FSD sequences used in this study acquire all images with the same cardiac trigger delay and do not have this issue. Another reason for varying TRs is the large R-R variations due to irregular heartbeats of subjects. This is more serious for the sequential acquisition of bright- and dark-blood data, which is used in the thoracic FSD sequence in this study. The influence of irregular heartbeats on background artefacts has been evaluated in volunteers with caffeine consumption or with cardiac arrhythmia by Kim *et al.* ⁶⁷.

The sensitivity to outliers is the main limitation for using OLS. For a regression biased towards background tissues, vascular and heart voxels with different signal level on BBIs and DBIs can be regarded as outliers and can affect the regression particularly when they occupy a large proportion of image voxels. As the conventional robust regression method, cRR using IRLS can minimise the effect of outliers by assigning a weight to each data point according to its distance from the regression line. Weights and regression coefficients are then recomputed iteratively.

The results of our study show that cRR achieved accurate and robust results for thoracic and iliac FSD-MRA data.

However, in femoral FBI, the muscle signal, which has similar low SI on BBIs and DBIs, has overwhelmingly the largest number of voxels and thus dominates the regression. Both OLS and cRR generated regression coefficients significantly smaller than the reference values, and were not sufficient to fully suppress background signal. To solve this problem, we adopted a polar system and deviation angle (in RRDA) instead of the Euclidean distance used in cRR. The reasons are as follows: Firstly, on the scatter plot, the SI difference between BBIs and DBIs is reflected as a deviation angle between the distribution of background points and the line $y=x$ (rotation), rather than a straight distance (translation). Therefore, it is more appropriate to correct SI based on deviation angles. Secondly, compared with low SI tissues such as muscle, high SI tissues have higher residual SI on subtracted images and therefore should have a larger weight in order to achieve an optimal background suppression, but they are given smaller weights in cRR due to their longer distance to the regression line. Additionally, the large voxel number of low SI background tissues is addressed by adding a normalised radial distance into the weighting function of RRDA. The points farther from the origin are assigned larger weights, so that the model is more strongly influenced by the relatively small number of points with large values.

Although background tissues were suppressed by using weighted subtraction, the desired vascular signals were only minimally affected. In this study, obvious vascular signal loss was only observed when the weighting factor is overestimated, for example, the OLS results in thoracic FSD-MRA. This is due to the distribution of vascular signal and background signal on the scatter plot and can be explained on Figure 4.1A. For the arterial pixels on Figure 4.1A, which locate on the bottom left of the scatter plot, their distance to the line $y=x$ (d_1) and the regression line (d_2) are very similar, while d_1 is much larger than d_2 for background pixels locating on the upper right. Therefore, using d_2 instead of d_1 does not change arterial SI much but can substantially reduce the SI of background tissues.

It should be noted that in conventional subtractive NCE-MRA techniques, background static signal suppression in unsubtracted raw images is still necessary. For example, STIR, magnetisation transfer contrast¹⁶⁰ and longer TE⁸¹ have been used in FBI for background suppression in order to reduce the SI of background tissues and thereby any residual background SIs on subtracted angiograms. The weighted subtraction method developed in this chapter gives subtractive NCE-MRA techniques a larger tolerance of background SI difference between BBIs

and DBIs. This potentially allows the imaging sequence design to maximise the arterial signal even at the cost of increasing background signals, *e.g.*, using minimum TE in FBI and selecting the flip angle maximising the arterial signal in bSSFP. Another potential sequence design is to generate images with maximum arterial signal but different background SIs on BBIs and DBIs, *e.g.*, using strong flow dephasing for the systolic acquisition and weak flow dephasing for the diastolic acquisition in FBI.

Although the regression results and background suppression effect of robust regression methods were analysed in volunteer and patient images, the diagnostic performance was not evaluated in this study. Future work will assess if clinical diagnosis or diagnostic confidence can be improved by background suppression using robust regression. Further work is also needed to evaluate the methods in other subtractive imaging sequences and anatomical regions.

4.6 Conclusion

In conclusion, robust regression approaches have been developed to correct the SI difference between background tissues on BBIs and DBIs for several subtractive NCE-MRA techniques, reducing residual background signal on subtracted angiograms. Compared with OLS and the conventional robust regression method, RRDA proved more resistant to outliers across the range of different NCE-MRA methods investigated and more sensitive to background signal with high intensity. In this initial study, it achieved accurate and robust performance applied to several different subtractive NCE-MRA techniques and different body regions.

An important advantage of reducing the static background signal in angiograms is that it improves image sparsity, which may facilitate compressed sensing reconstruction and potentially improve reconstruction accuracy ¹⁶¹. A reconstruction method exploiting the improved sparsity will be introduced in Chapter 6.

Chapter 5. Optimisation of Poisson-disk sampling pattern for highly accelerated femoral NCE-MRA

As discussed in Chapter 3, NCE-MRA techniques typically have long acquisition times but can be accelerated by CS, PI and PF sampling. The purpose of this chapter is to investigate the optimal sampling patterns for the 3D accelerated femoral artery FBI sequence.

5.1 Introduction

NCE-MRA techniques suffer from long acquisition times, especially those requiring more than one acquisition, such as FBI. The long acquisition time not only limits the clinical acceptance of these techniques but also renders them sensitive to artefacts from patient motion. CS, PI and PF sampling can be used to accelerate the acquisition by using, for example, a Poisson-disk sampling pattern¹⁰². However, the design of the optimal sampling pattern still needs to be evaluated.

This study investigates the optimal values for several important parameters of sampling pattern design. Retrospective sub-sampling, *i.e.* acceleration, was performed on ten fully sampled datasets using different sampling patterns to determine the optimal parameter ranges. The performance of the optimised patterns was then compared with typical non-optimised patterns.

5.2 Sampling Pattern Design for 3D Accelerated MRI

5.2.1 Requirements of PI, PF and CS

The sampling along the readout direction must be continuous and relatively smooth, as it is impossible to switch rapidly the magnetic field gradients that perform the spatial encoding to ‘jump around’ in k -space. Therefore, undersampling is normally performed in the k_y - k_z plane for 3D Cartesian MRI acquisitions.



Figure 5.1 Typical sampling patterns in the k_y - k_z plane for 3D MRI acquisitions. A: PI in k_y and k_z directions (for autocalibrating methods), B: PF in k_y directions, C: CS using a Poisson-disk pattern with variable density.

For parallel imaging, k -space is sampled on a Cartesian grid with constant distances between samples (Figure 5.1A), generating coherent and predictable artefacts (aliasing). For autocalibrating methods such as GRAPPA¹³⁶ and SPIRiT¹³⁹, a fully sampled central calibration region is required for calculating the linear combination weights, or calibration kernel.

PF Sampling is applied by covering only a fraction of k -space and using conjugate symmetry to fill the missing sections (Figure 5.1B). The sampled fraction needs to be larger than one half of the length of the dimension so that a phase reference can be calculated from the symmetric centre of k -space. Previous studies reported that PF sampling can be applied in both k_y and k_z dimensions for 3D acquisitions¹⁶².

CS has more requirements on sampling patterns. Firstly, the samples must be selected randomly to guarantee a very high degree of incoherence¹⁶³. However, it was noticed that purely random patterns have a number of large ‘holes’ and ‘clumps’ in the k -space coverage, which can limit the image quality achieved by CS⁹⁴. As a pseudo-random distribution, the Poisson-disk sampling pattern^{122,123} is more preferable, as it reduces the numbers of ‘holes’ and ‘clumps’ by imposing constraints on the maximum and minimum distance between sampling points. Secondly, for MRI, the underlying signal density of k -space is not uniform but is most concentrated for the low-frequency components at the centre of k -space and falls away towards the periphery. This characteristic leads to the preferred use of variable density sampling patterns that are dense near the centre of k -space and sparse near the periphery. Finally, a fully sampled central region is typically kept to ensure a reliable CS initialisation¹⁴². Figure 5.1C shows a typical Poisson-disk sampling pattern with variable density for 3D CS acquisitions.

5.2.2 Variable density Poisson-disk

In creating a Poisson-disk distribution, each sampled point generated a disk around itself with a radius of r , where the probability of a new sample was decreased to ensure a maximum spread of the sampling over the k_y - k_z plane.

Variable density undersampling commonly uses a probability density function that decays with the distance to the centre of k -space^{164,165}. In this study, a Gaussian distribution is used with the probability density function as:

$$P(k_y, k_z) = e^{-\left(\left(\frac{k_y}{S_y}\right)^2 + \left(\frac{k_z}{S_z}\right)^2\right)(10d)^2} \quad (5.1)$$

where k_y and k_z are the k -space coordinates in the ranges of $[-S_y, +S_y]$ and $[-S_z, +S_z]$ respectively, S_y and S_z are the sizes of the k_y - k_z plane, d is the density decay factor. The probability density function is incorporated into the pattern generation by modifying the disk radius r as:

$$r(k_y, k_z) = \frac{r_0}{P(k_y, k_z)} \quad (5.2)$$

where r_0 is a constant disk radius defining the minimum distance between neighbouring points when using a uniform distribution. In this study, the Poisson-disk generation program was modified based on the code provided by Michael W. Weiner from University of California, San Francisco.

5.3 Optimisation of Sampling Pattern Parameters

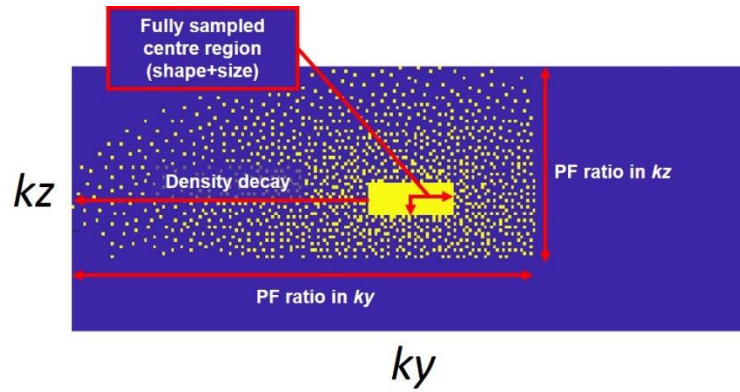


Figure 5.2 A typical Poisson-disk sampling pattern for 3D accelerated imaging combining PI, CS and PF. Key parameters in sampling pattern design include density decay factor, fully sampled central region size, fully sampled central region shape and PF sampling ratios in k_y and k_z dimensions.

PI, CS and PF can be combined together by using a Poisson-disk sampling pattern shown as Figure 5.2. There are several important parameters in pattern design, which will be evaluated and optimised in this study.

5.3.1 Density decay factor

Although variable density patterns are normally preferred, the extent of the density variability needs to be optimised. If too many sampling points accumulate in the centre of k -space and too few at the edges, the reconstructed images may lose edge details or get blurred due to reduced high-frequency components. In contrast, the reconstruction accuracy may also be affected if the sampling pattern is too uniform and cannot reflect the underlying signal density. In this study, the density decay factor in equation 5.1 is optimised, which determines the reduction of sampling density towards the periphery of k -space.

5.3.2 Fully sampled central region

As described above, the fully sampled central region of k -space is essential for all CS, PI and PF. The shape and size of the calibration region may influence the reconstruction quality and needs to be optimised. Bearing in mind that for a given total number of sampling points, an increased central calibration region size means fewer peripheral points in the k -space. For example, a large fully sampled region improves calibration accuracy in PI, phase estimation accuracy in PF and initialisation reliability in CS, but may lead to impaired detail depiction and image blurring due to insufficient sampling points at the periphery of k -space, and vice versa.

5.3.3 Partial Fourier ratio(s)

Although PF can be combined with CS and PI, it remains unclear whether the introduction of PF can further improve acceleration performance or not in comparison with only using CS and PI, and what fraction of k -space should be filled in pattern design. The performance of using two-dimensional PF and the optimal fraction of k_z dimension is also evaluated in this study.

5.4 Methods

5.4.1 Data acquisition

Ten fully sampled femoral artery FBI datasets were acquired from healthy volunteers using a 1.5 T MRI system (Discovery MR450; GE Healthcare, Waukesha, WI). Parameters included

matrix size: 224×224×80, ETL: 80–90, FOV: 40–44 cm, slice thickness: 2 mm, TE: 45 ms, TR: 2 or 3 heartbeats, receiver bandwidth: ±62.5 kHz and total acquisition time: 346–394 TRs. The readout direction was set to be the superior-inferior direction. Retrospective simulated acceleration was performed on the fully sampled data. Images were reconstructed using the KSPIC method, which will be described in Chapter 6.

5.4.2 Image assessment

The four objective quantitative metrics described in Chapter 3 were used to assess the image quality of reconstructed undersampled images. PSNR, SSIM and CNR of artery-to-background require a full reference, which is provided by the fully sampled images. For PSNR, SSIM and CNR of artery-to-background, the measurement was performed on the whole 3D dataset. For sharpness evaluation, the measurement was performed on each axial slice along the y and z directions, corresponding to the k_y - k_z undersampling plane. The final measurements were averaged over all the ten datasets.

5.4.3 Pattern optimisation

The optimisation was performed using the AFs of 6×, 10× and 14×. The total numbers of sampling points for 6×, 10× and 14× were 2342, 1408 and 1006 respectively. The density decay factor, the size and shape of fully sampled central region, PF ratio in the k_y and k_z dimensions were optimised sequentially. For each optimisation process, only one parameter was varied to test their influence on the reconstruction quality. Once finishing one process, the optimised value was carried forward to the optimisation of the next parameter.

Optimised sampling patterns under different AFs were designed using the optimal ranges of values. The performance of the optimised sampling patterns with AFs from 4 to 20 was evaluated on the ten fully sampled datasets.

In order to assess the improvements offered by the optimised sampling patterns, the resulting images were compared with some typical non-optimised images: their sampling patterns had uniform density (density decay factor of zero), square fully sampled central regions (16 points × 16 points) and did not use PF (PF factor of 1.0). A paired Student's t -test was used for the comparison. A P value less than 0.05 was considered to indicate statistical significance.

5.5 Results

5.5.1 Optimisation of density decay factor

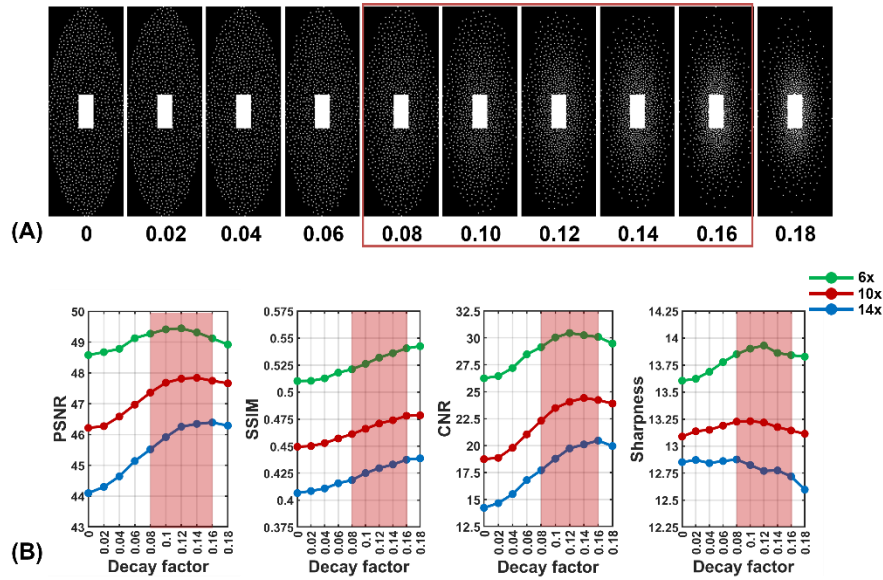


Figure 5.3 Sampling patterns with varying density decay factor (10×) (A) and corresponding quantitative measurements with AFs of 6×, 10× and 14× (B).

Figure 5.3(A) shows the sampling patterns with density decay factor varying from 0 to 0.18 (10× acceleration). The fully sampled region sizes are 40×14, 32×12 and 28×10 for 6×, 10× and 14× respectively. The corresponding quantitative measurements using different AFs are shown in Figure 5.3(B). The result shows that the four metrics all returned relatively high values when the factor is between 0.08 and 0.16, indicating an optimal value range (shaded red in Fig 5.3) in this study.

5.5.2 Optimisation of fully sampled central region size

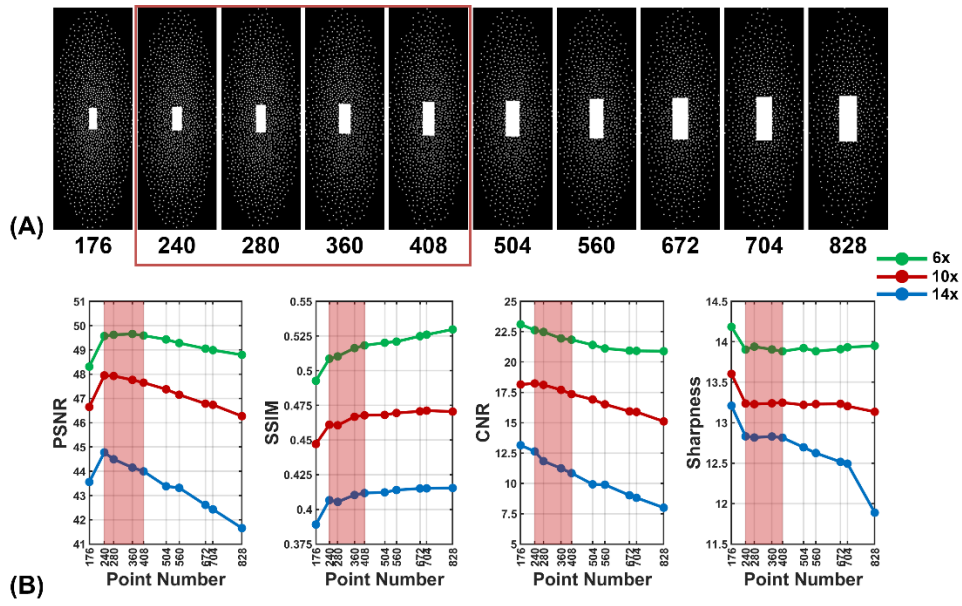


Figure 5.4 Sampling patterns with varying sizes of the fully sampled central region (A) and corresponding quantitative measurements with AFs of 6 \times , 10 \times and 14 \times (B).

As shown in Figure 5.4(A), the sizes of the fully sampled central region were 22 \times 8, 24 \times 10, 28 \times 10, 30 \times 12, 34 \times 12, 36 \times 14, 40 \times 14, 42 \times 16, 44 \times 16 and 46 \times 18, which respectively corresponded to the following numbers of points: 176, 240, 280, 360, 408, 504, 560, 672, 704 and 828. The density decay factor was fixed at 0.1.

The result in Figure 5.4(B) shows that the four metrics all returned relatively high values when the number of points was between 240 and 408. This number range corresponds to a portion (central region number/total number) range of 0.10–0.17 for the AF of 6 \times , 0.17–0.29 for the AF of 10 \times and 0.24–0.40 for the AF of 14 \times . Further increasing the size of the fully sampled region increases SSIM but reduces CNR and PSNR. It can also be observed that the measurements for a higher AF (14 \times) reduce more rapidly than measurements for a lower AF (6 \times).

5.5.3 Optimisation of fully sampled central region shape

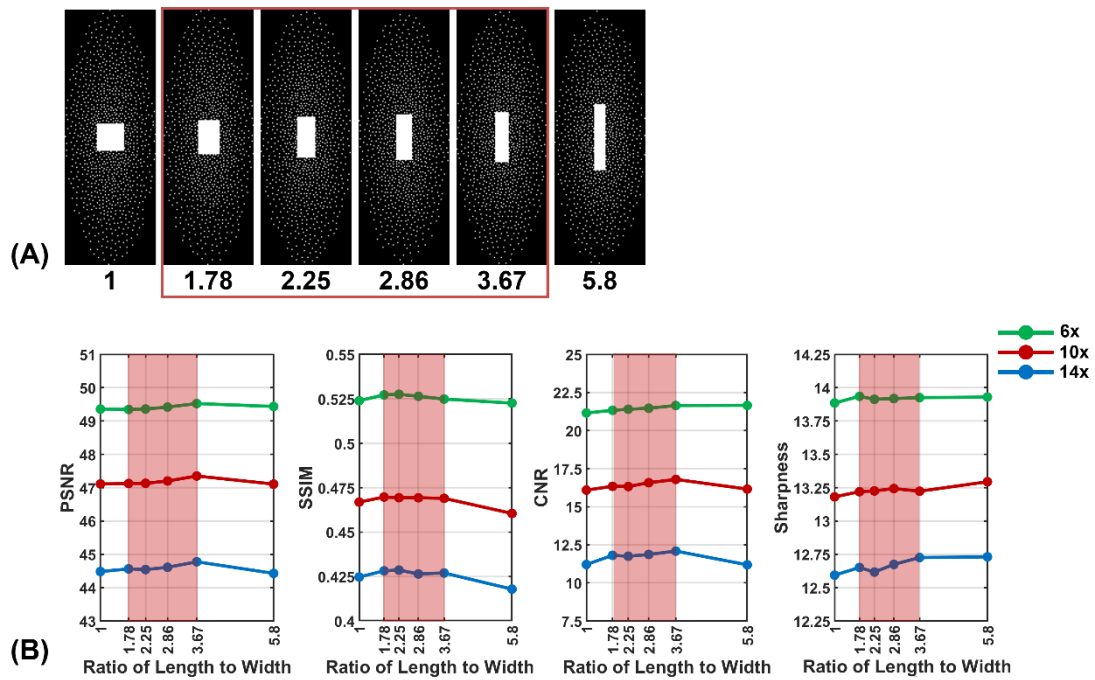


Figure 5.5 Sampling patterns with different shapes of fully sampled central region (varying ratios of length to width) (10×) (A) and corresponding quantitative measurements with AFs of 6×, 10× and 14× (B).

As shown in Figure 5.5(A), the sizes of the fully sampled central region are 24×24 , 32×18 , 36×16 , 40×14 , 44×12 and 58×10 , corresponding to ratios of length to width from 1 to 5.8. The point numbers of the fully sampled region are very close for different patterns (560 – 580). The density decay factor is fixed at 0.1.

There is no significant variation in the values of the four metrics, indicating that the shape of the fully sampled central region does not have a strong influence on acceleration performance. A range of 1.78 to 3.67 is considered optimal.

5.5.4 Optimisation of PF ratio in the k_y dimension

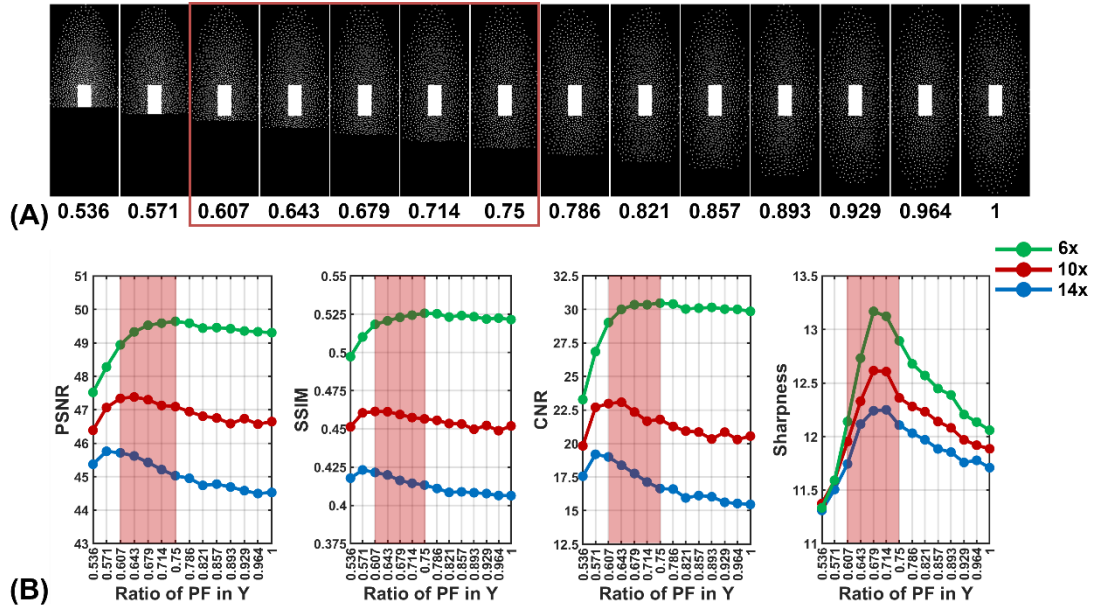


Figure 5.6 Sampling patterns with varying PF ratios in the k_y dimension (10x) (A) and corresponding quantitative measurements with AFs of 6 \times , 10 \times and 14 \times (B).

Figure 5.6(A) shows the sampling patterns with the PF ratio in k_y dimension increasing from 0.536 to 1 using the AF of 10 \times . The fully sampled region sizes are 40 \times 14, 32 \times 12 and 28 \times 10 for 6 \times , 10 \times and 14 \times respectively (the region was cropped for PF ratios of 0.536 and 0.571). The density decay factor is fixed at 0.1.

The results in Figure 5.6(B) demonstrate that the range between 0.607 and 0.75 would be the overall optimal range for PF sampling ratio in the k_y dimension for different AFs for different AFs. The values of all the four metrics reduce when their values are out of this range, especially for the sharpness. To be more specific, the PSNR, SSIM and CNR results show that the optimal range for the AF of 14 \times is smaller than the optimal ratio for the AF of 6 \times , indicating that a smaller PF ratio in the k_y dimension, *i.e.*, larger blank regions, is more desirable for a larger AF (14 \times).

5.5.5 Optimisation of PF ratio in the k_z dimension

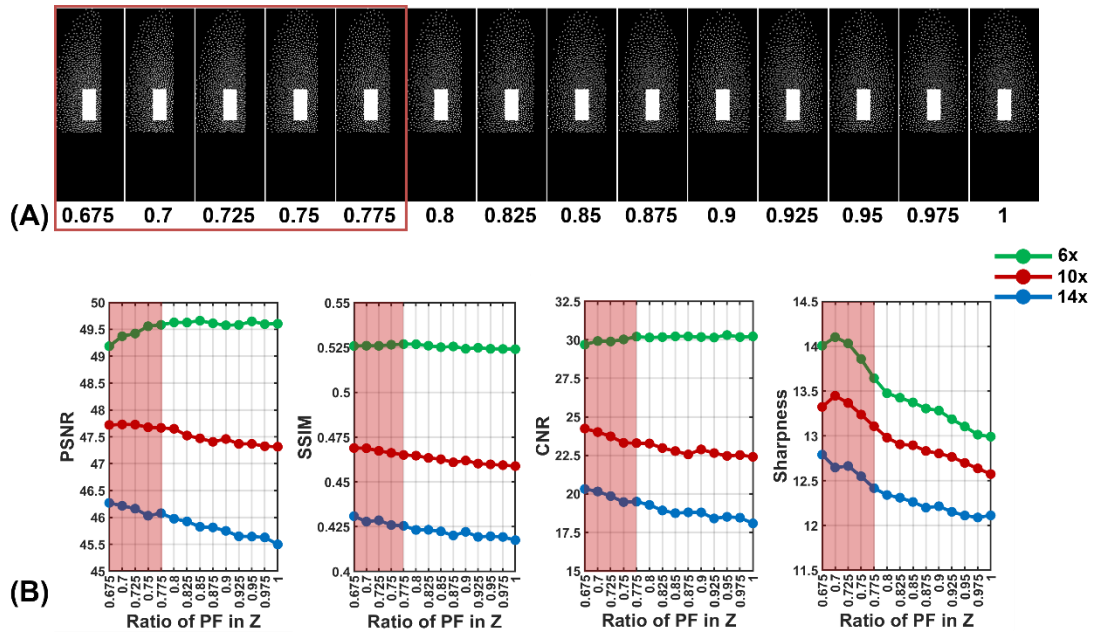


Figure 5.7 Sampling patterns with varying PF ratios in the k_z dimension (10x) (A) and corresponding quantitative measurements with AFs of 6 \times , 10 \times and 14 \times (B).

Figure 5.7(A) shows the sampling patterns with the PF ratio in the k_z dimension increasing from 0.675 to 1 (10 \times acceleration). The fully sample region sizes are 40 \times 14, 32 \times 12 and 28 \times 10 for 6 \times , 10 \times and 14 \times respectively. The density decay factor is fixed at 0.1. The optimised value 0.679 from the previous section was used for the fraction of k_y . The result in Figure 5.7(B) shows that the four metrics returned relatively high values when the k_z PF ratio is between 0.675 and 0.775. For an AF of 6 \times , the PSNR value is higher when the ratio is larger, but the PSNR value reduces with increasing ratio for an AF of 14 \times . This trend also exists for SSIM and CNR, indicating that a smaller PF ratio in the k_z dimension, *i.e.*, larger blank regions, is more desirable for a larger AF (14 \times).

5.5.6 Summary of optimised parameters

According to the above evaluation results, the optimal value ranges for the parameters in sampling pattern design in this study are summarised in Table 5.1.

Table 5.1 The optimal value ranges by AF for the sampling pattern design (matrix size: 224×224×80)

| AF | PF ratio in k_y | PF ratio in k_z | Density decay | Fully sampled central region shape (ratio of length to width) | Fully sampled central region size (point number and portion) |
|-----|-------------------|-------------------|---------------|---|--|
| 6× | 0.68–0.75 | 0.725–0.775 | 0.08–0.14 | 1.78–3.67 | 240–408 (10%–17%) |
| 10× | 0.64–0.71 | 0.7–0.75 | 0.08–0.14 | 1.78–3.67 | 240–408 (17%–29%) |
| 14× | 0.61–0.68 | 0.675–0.725 | 0.1–0.16 | 1.78–3.67 | 240–408 (24%–40%) |

5.5.7 Comparison of optimised patterns and non-optimised patterns

Figure 5.8 shows the optimised patterns and non-optimised patterns with AFs from 4× to 20× and their performance on one 3D FBI dataset. The parameters of the two series of patterns are summarised in Table 5.2. It can be observed that the optimised patterns improved the image quality in terms of signal loss (blue arrowheads), blurring (blue arrowheads) and depiction of small branches (yellow arrowheads). The corresponding quantitative evaluation results are summarised in Fig. 5.9. Optimised patterns outperformed non-optimised patterns in all four metrics.

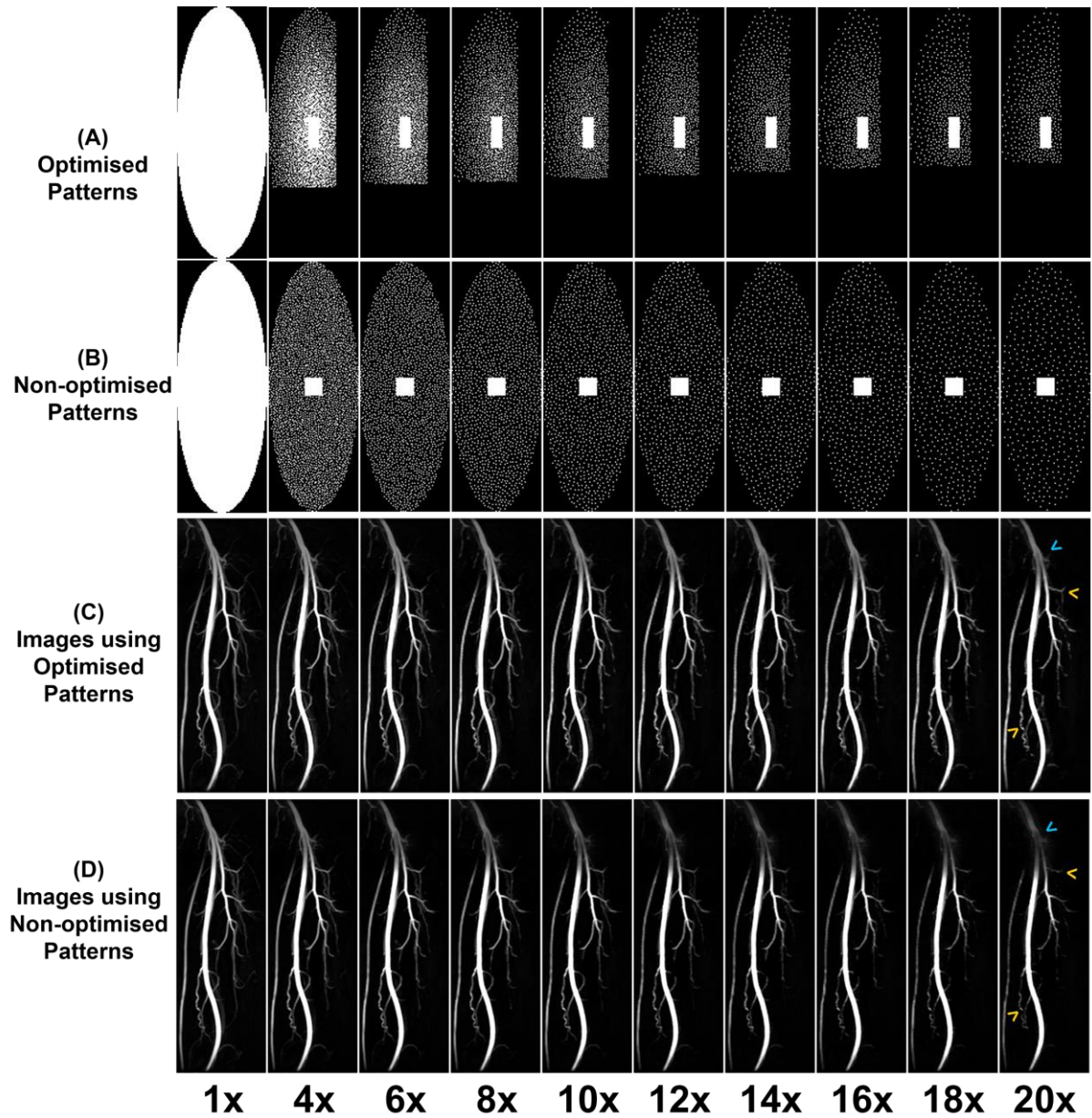


Figure 5.8 Optimised (A) and non-optimised (B) sampling patterns and the corresponding example MIPs (left leg) of reconstructed images (C and D) with different AFs. Blue arrowheads on (C) and (D) denote signal loss and blurring on images using non-optimised patterns. Yellow arrowheads denote improved delineation of small branches on images using optimised patterns.

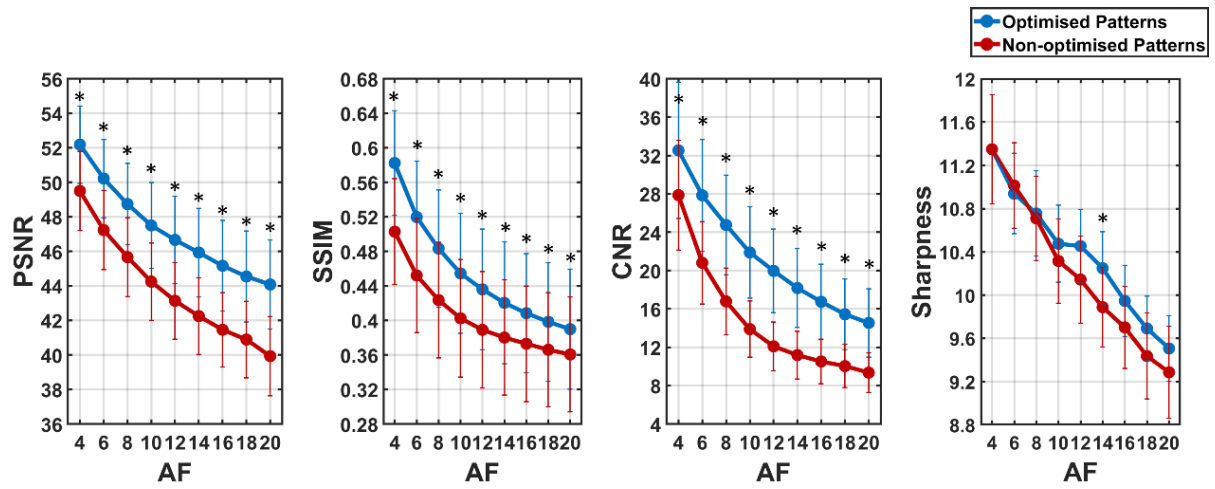


Figure 5.9 Quantitative evaluation results of accelerations using optimised patterns and non-optimised patterns with different AFs. The values are the mean and standard deviation calculated over the ten volunteer datasets. *denotes statistical significance between optimised patterns and non-optimised patterns (two-tailed paired Student's t -test, $P < 0.05$).

Table 5.2 The parameters by AF for optimised and non-optimised sampling patterns in Chapter 5 (matrix size: 224×224×80)

| AF | Optimised /non-optimised | PF ratio in k_y | PF ratio in k_z | Density decay | Fully sampled central region size { k_y size, k_z size} |
|-----|-----------------------------|-------------------|-------------------|------------------|---|
| 4× | Optimised | 0.71 | 0.75 | 0.1 | {28,10} |
| | Non-optimised | 1 | 1 | 0 | {16,16} |
| 6× | Optimised | 0.71 | 0.75 | 0.1 | {28,10} |
| | Non-optimised | 1 | 1 | 0 | {16,16} |
| 8× | Optimised | 0.70 | 0.74 | 0.1 | {28,10} |
| | Non-optimised | 1 | 1 | 0 | {16,16} |
| 10× | Optimised | 0.68 | 0.73 | 0.1 | {28,10} |
| | Non-optimised | 1 | 1 | 0 | {16,16} |
| 12× | Optimised | 0.67 | 0.71 | 0.1 | {28,10} |
| | Non-optimised | 1 | 1 | 0 | {16,16} |
| 14× | Optimised | 0.66 | 0.71 | 0.1 | {28,10} |
| | Non-optimised | 1 | 1 | 0 | {16,16} |
| 16× | Optimised | 0.64 | 0.7 | 0.1 | {28,10} |
| | Non-optimised | 1 | 1 | 0 | {16,16} |
| 18× | Optimised | 0.63 | 0.69 | 0.1 | {28,10} |
| | Non-optimised | 1 | 1 | 0 | {16,16} |
| 20× | Optimised | 0.62 | 0.68 | 0.1 | {28,10} |
| | Non-optimised | 1 | 1 | 0 | {16,16} |

5.6 Discussion

This study evaluated the influence of the parameters in Poisson-disk sampling pattern design and explored their optimal values. The optimisation process was performed at three different AFs in this study.

Poisson-disk patterns using variable density with optimised k -space density decay factor outperformed uniformly distributed density patterns, but using overlarge density decay factors would lead to the loss of high-frequency components and impair the quality of reconstructed images. The range between 0.08 and 0.14 is suggested for the selection of density decay factor.

The design of the fully sampled central region also has an influence on the acceleration performance. The optimal size for the central region is 24×10–34×12 for the matrix size used in this study. The shape of the central region has less influence on image quality. In this study, the

optimal range of the length to width ratio of the central region was 1.78–3.67, and the length to width ratio of the whole k_y - k_z plane was 2.8. Therefore, keeping the length to width ratio of central region consistent with the phase to slice resolution ratio is suggested.

It was shown that compared to only using CS and PI, the implementation of PF in two directions (k_y and k_z) can further improve the acceleration performance, especially in terms of image sharpness. The optimal ranges of PF ratios in both k_y and k_z dimensions vary slightly, depending on the desired AF. Smaller PF ratios with larger blank regions are more desirable for larger AFs, so that the sampled region would not be too sparse.

Clearly the parameters in the sampling pattern design may interact with each other, and changing one of them may also affect the optimal value of the other parameters. For example, the optimal density decay factor may be different in the conditions with and without PF. Future work will perform the optimisation process iteratively to obtain the patterns with optimal values for all parameters.

There is also scope for separate optimisation of the sampling ratios or decay patterns for the k_y and k_z directions separately, particularly if the desired resolution is not isotropic and the FOV is different in slice and phase-encode directions.

In this study, the determination of optimal ranges of parameters was not completely objective. Several adaptive optimisation techniques have been proposed^{166–168}, which optimise sampling patterns in an objective and automatic way. These methods use fully sampled data to construct a sampling distribution, from which the sampling points are drawn randomly. The main drawback of these algorithms is that they do not optimise sampling patterns for a given reconstruction method. However, Gözcü *et al.* recently used a learning-based framework to generate parameter-free patterns from the fully sampled training data, which can optimise patterns both for a specific reconstruction method and imaging anatomy¹⁶⁹. These methods could be investigated in future work.

Finally, the evaluation in this study was only performed on the femoral FBI MRA images reconstructed by the KSPIC method. It is quite likely that the optimal parameter values vary for different vascular study regions, imaging protocols, reconstruction methods and even different image matrix sizes. For example, the density decay factor should be selected according to a power distribution of k -space^{163,166}, which can be affected by the anatomical details. To achieve

optimal acceleration performance, specific sampling pattern optimisation for other techniques and regions is still needed.

5.7 Conclusion

In this study, we optimised the parameters in sampling pattern design with different AFs for the 3D accelerated femoral artery FBI sequence. In a comparison using retrospective acceleration by subsampling of a full dataset, the optimised patterns outperformed the non-optimised patterns. The sampling patterns used in Chapters 6 and 7 will be designed according to the optimisation results in this study.

Chapter 6. Reconstruction for highly accelerated subtractive NCE-MRA using k -space subtraction with phase and intensity correction

This chapter introduces several reconstruction strategies for accelerated subtractive NCE-MRA. A new reconstruction method, k -space subtraction with phase and intensity correction, is developed, which can exploit the sparsity of subtracted angiogram data and potentially improve reconstruction performance.

6.1 Introduction

The sparsity of the representation of the signal is an important factor for both CS and PI reconstruction. With increasing sparsity, fewer samples are needed to accurately reconstruct the signal, and a better reconstruction quality can be achieved from a given number of samples^{94,96}. As described in section 3.1.3 of Chapter 3, MR angiograms are especially sparse, with high signal only from blood vessels, and low background signals.

Subtractive NCE-MRA involves at least two raw datasets with different blood contrasts and one subtracted dataset, enabling different potential reconstruction strategies for accelerated imaging. Generally, there are two reconstruction strategies for subtractive NCE-MRA. One strategy is to perform reconstruction on bright-blood (BB, bright-artery for arteriography) and dark-blood (DB, dark-artery for arteriography) data separately followed by magnitude subtraction, and the other is to perform subtraction in k -space and then reconstruct the subtracted data.

Methods based around magnitude subtraction are straightforward and commonly used, but they do not take advantage of sparsity in the subtracted angiogram. Rapacchi *et al.* proposed a CS algorithm that combines BB and DB reconstruction together and adds a magnitude subtraction term into the cost function to exploit the sparsity of angiogram¹⁰². This method was reported to improve CS reconstruction in both thoracic DCE-MRA and NCE dynamic intracranial MRA^{102,115}. To distinguish it from the traditional magnitude subtraction method, this method will be called ‘combined magnitude subtraction’ (CMS) in this chapter.

Methods based on k -space subtraction are alternative approaches to promote sparsity. The subtracted k -space data is inherently sparse in its image domain representation. Although having drawbacks in terms of increased sensitivity to phase error and imposed signal-to-noise ratio

penalty^{102,115}, complex subtraction in k -space has shown superior performance in both peripheral CE- and NCE-MRA with PI, especially at large AFs^{96,170}.

Another problem of subtractive NCE-MRA is that some background tissues appear with a different intensity level in BB and DB images, resulting in residual signals in the subtracted images^{68,69}. An optimised weighted subtraction approach has been proposed in Chapter 4, which corrects the intensity difference of background tissues and improves background suppression. Applying the intensity correction prior to reconstruction could not only suppress the background tissue signals but also potentially further increase the data sparsity. However, weighted complex subtraction is expected to cause an increase of negative signals after subtraction, which would appear as background artefacts due to the loss of polarity in the reconstructed magnitude image^{161,171}. Moreover, the weighting factor cannot be obtained directly from complex datasets.

In this chapter, we firstly propose an improved reconstruction method based on k -space subtraction, termed as k -space Subtraction with Phase and Intensity Correction (KSPIC). A phase correction procedure is used to preserve the polarity of the negative signal and remove background artefacts. This procedure requires a background reference for phase corrections, which can be provided by the systolic or diastolic dataset in subtractive NCE-MRA. Moreover, an intensity correction procedure is applied based on the method described in chapter 4, with the weighting factors calculated from the DB images and BB images generated by a fast and incomplete CS reconstruction. Secondly, the CMS method^{102,115} is implemented for subtractive NCE-MRA. Intensity correction is also applied for CMS to further improve its performance in background suppression.

Both a retrospective study and a prospective study have been performed. The retrospective study utilised ten fully sampled Cartesian femoral artery FBI datasets and performed simulated undersampling on them. The prospective study performed accelerated FBI acquisitions using specific undersampling schemes. The performance of KSPIC and CMS are compared with conventional k -space subtraction reconstruction (KS) and magnitude subtraction reconstruction (MS) in both retrospective and prospective studies.

6.2 Reconstruction strategies for subtractive NCE-MRA

6.2.1 Independent reconstruction with magnitude subtraction afterwards (MS)

One conventional strategy is to reconstruct BB and DB datasets (denoted by subscripts b and d respectively) independently and then do magnitude subtraction (MS). The flow chart of MS is shown in Figure 6.1A. According to the theory described in Chapter 3, the reconstruction can be written as an unconstrained optimisation problem:

$$u_b = \arg \min_{u_b} \|RFu_b - f_b\|_2^2 + \lambda \|\Phi u_b\|_{1,2} + \gamma \|(G - I)Fu_b\|_2^2 \quad (6.1)$$

$$u_d = \arg \min_{u_d} \|RFu_d - f_d\|_2^2 + \lambda \|\Phi u_d\|_{1,2} + \gamma \|(G - I)Fu_d\|_2^2 \quad (6.2)$$

Here, f_b and f_d are the acquired data, u_b and u_d are the estimated images, G denotes the SPIRiT kernels computed from auto-calibration signals, F is the Fourier operator, and R is a k -space sampling operator. Φ is the sparsifying transform operator, which is finite-differences in this study. $\|\cdot\|_{1,2}$ is the joint L1 norm. λ and γ are two regularisation parameters, which determine the balance between the data consistency, calibration consistency and the promotion of sparsity. Following the reconstruction, the intensity correction method described in Chapter 4 can optionally be applied to the reconstructed BB and DB images to suppress residual signals from background tissues (MS-IC). The RRDA method with $\alpha=1$ is used for all the reconstruction strategies with intensity correction in this chapter.

6.2.2 K -space subtraction prior to reconstruction (KS)

Subtracting the raw data in k -space prior to reconstruction (KS) can take advantages of the sparsity more directly (Figure 6.1B). The reconstruction can be formulated as:

$$u_s = \arg \min_{u_s} \|RFu_s - (f_b - f_d)\|_2^2 + \lambda \|\Phi u_s\|_{1,2} + \gamma \|(G - I)Fu_s\|_2^2 \quad (6.3)$$

6.2.3 Combined reconstruction with magnitude subtraction (CMS)

The combined reconstruction adds magnitude subtraction terms between BB and DB datasets, which can exploit the sparsity of subtracted images (Figure 6.1C). u_b and u_d are iteratively minimised in a single algorithm:

$$(u_d, u_b) = \arg \min_{(u_d, u_b)} \left\{ \begin{aligned} &\|RFu_d - f_d\|_2^2 + \lambda \|\Psi u_d\|_{1,2} + \mu \|u_b|e^{i\phi_d} - u_d|_{1,2} + \gamma \|(G-I)Fu_d\|_2^2 \\ &\|RFu_b - f_b\|_2^2 + \lambda \|\Psi u_b\|_{1,2} + \mu |u_b - |u_d|e^{i\phi_b}|_{1,2} + \gamma \|(G-I)Fu_b\|_2^2 \end{aligned} \right\} \quad (6.4)$$

where μ is the parameter controlling the weight of the subtraction terms.

The intensity correction method can also be employed after the CMS reconstruction (CMS-IC).

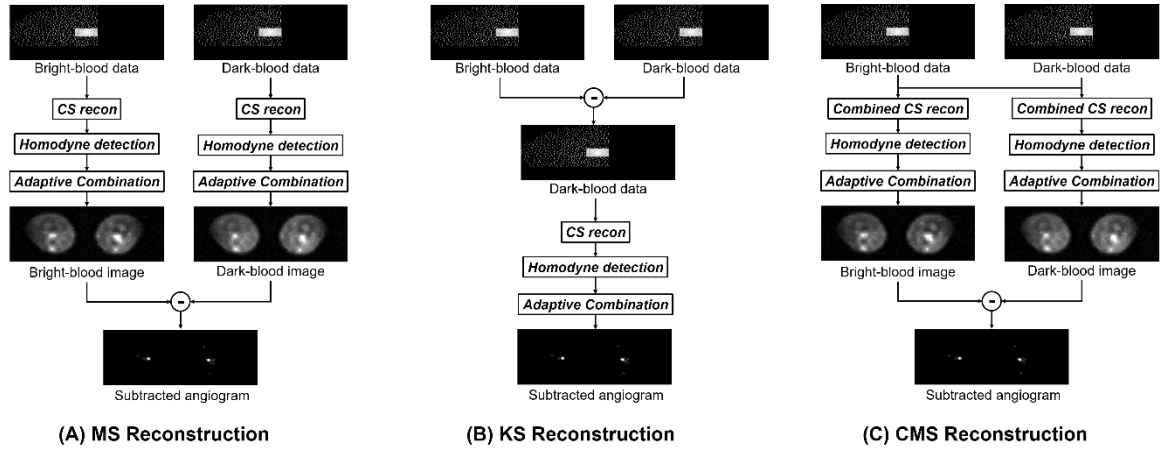


Figure 6.1 Flow charts of (A) the magnitude subtraction reconstruction process, (B) the k -space subtraction reconstruction process and (C) the combined magnitude subtraction reconstruction.

6.2.4 K -space subtraction with phase correction (KSPC)

For FBI, the SI of some background tissues, such as muscle and fat, may appear slightly higher on the DB images^{96,151}. Its representation in the image domain should become negative after subtraction. However, when using k -space subtraction methods, the negative signal loses its polarity when taking the magnitude of the reconstructed image and appears as background artefacts on the subtracted angiograms.

Phase-sensitive detection can be used to correct this background phase variation so that the real part of the image can be used, and the polarity can be preserved^{172–176}. This method normally requires an additional acquisition of a background phase reference, which should adequately represent the background phase variation but not be corrupted by polarity shifts¹⁷⁴. Fortunately, in subtractive NCE-MRA, this reference can be provided by the BB or DB data, which has the same background phase variation as subtracted dataset and all positive values in the image domain.

In KS with phase correction (KSPC), a homodyne low pass filter is applied to the DB or BB data to obtain a low-resolution image as a background phase reference. The phase of the reference image ϕ_r is then removed from the reconstructed subtracted image I_S on a pixel-by-pixel basis, so that the polarity of the negative signal is preserved in the real part of the resultant image (I_{PC}):

$$I_{PC} = \text{Re}\{I_S e^{-i\phi_r}\} \quad (6.5)$$

Finally, the corresponding background artefacts can be removed by nulling the negative values.

6.2.5 *K*-space subtraction with phase and intensity correction (KSPIC)

The intensity correction method described in Chapter 5 can be employed in *k*-space subtraction approaches. Although intensity correction can easily be applied to magnitude subtraction approaches, it is not straightforward to determine the appropriate weighting factor for *k*-space subtraction approaches. In order to calculate the weighting factor prior to the full CS reconstruction, a fast CS reconstruction is firstly performed to acquire a partially reconstructed image set. Weighted subtraction in *k*-space can lead to additional negative signals after subtraction but can be removed by the phase correction procedure.

The image reconstruction process of *k*-space subtraction with phase and intensity correction (KSPIC) is as shown in Fig. 6.2. Firstly, a fast CS reconstruction with only two iterations and without PI reconstruction is performed on 10% of the *k*-space data. The 10% subsampled data was obtained by performing a 1D fast Fourier transform (FFT) in the *x*-direction to form a hybrid *x-k_y-k_z* space, and then selecting equally-spaced axial slices along the *x*-direction. This gives the *k*-space data for a set of axial (*k_y-k_z*) slices (10% of the total number of slices). Secondly, the intensity correction procedure is used to acquire the linear regression coefficient between the BB and DB signals of the background tissues. Next, a weighted complex subtraction is performed on the *k*-space data, using the linear regression coefficient as the weighting factor. A full CS reconstruction, in combination with SPIRiT¹³⁹ for PI and homodyne detection for PF sampling, is then performed on the full subtracted dataset. Finally, a background phase reference is reconstructed from the symmetric central region of the DB dataset and is used to restore the polarity of the negative signal (as described above for KSPC).

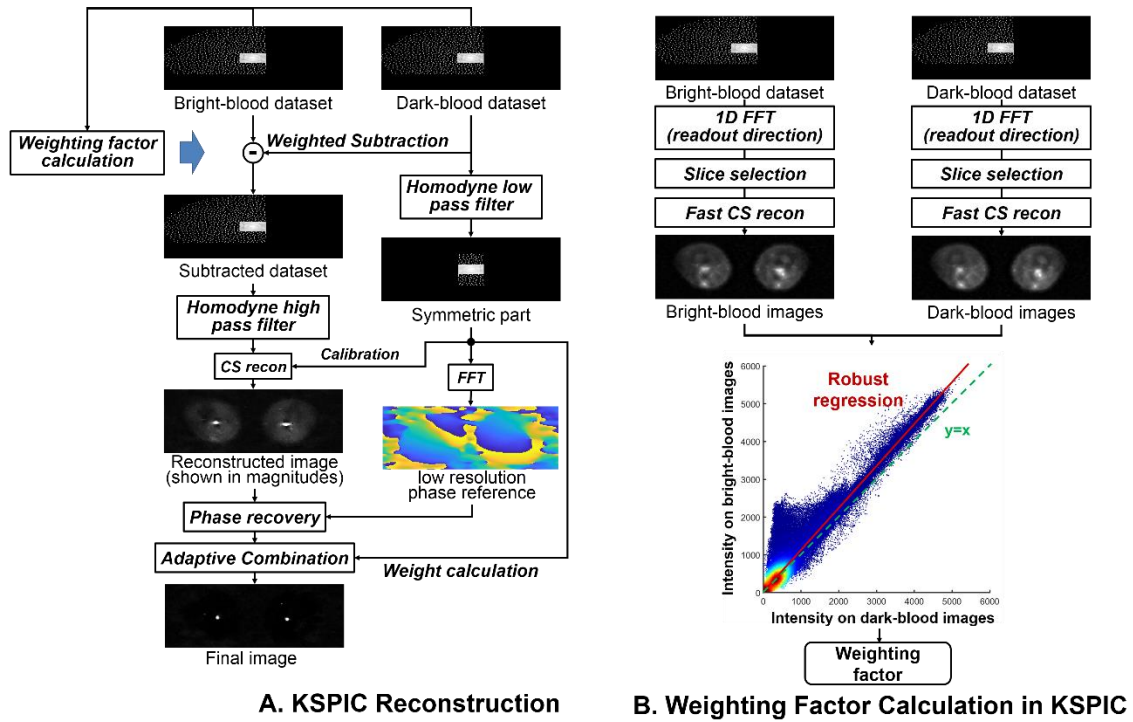


Figure 6.2 Flow charts of (A) the KSPIC reconstruction process and (B) the weighting factor calculation procedure. The phase map is obtained from the DB dataset.

6.2.6 Summary of reconstruction strategies

In summary, the reconstruction strategies included in this study are listed in Table 6.1. KS-IC images will not be assessed because they are corrupted by background artefacts caused by inverted negative signals, which are enhanced by the weighted subtraction. All the other methods will be evaluated in the retrospective study using quantitative metrics. MS, KS, CMS-IC and KSPIC will be evaluated in the prospective study using subjective quality scores.

Table 6.1 Reconstruction methods included in this study

| | Magnitude subtraction | | K-space subtraction | |
|------------------------------|-----------------------|-----------------------|---------------------|-----------------------|
| | Conventional | Combined | Conventional | With phase correction |
| Without intensity correction | MS ^{a,b} | CMS ^a | KS ^{a,b} | KSPC ^a |
| With intensity correction | MS-IC ^a | CMS-IC ^{a,b} | KS-IC | KSPIC ^{a,b} |

^a denotes the methods that will be evaluated in the retrospective study using quantitative metrics

^b denotes the methods that will be evaluated in the prospective study using qualitative scores

6.3 Methods

6.3.1 Subjects and imaging protocols

Twelve healthy subjects (8 men and 4 women; age range 24–45 years) were imaged using the 3D Cartesian femoral artery FBI sequence. Examinations were performed using a 1.5 T system (Discovery MR450; GE Healthcare, Waukesha, WI) and a 32-channel or 8-channel cardiac array coil. Studies were approved by the local research ethics committee, and all participants gave informed consent.

Prior to the 3D FBI acquisition, a 2D ECG-gated preparation scan with a single thick slice and multiple cardiac phases was used to determine the appropriate diastolic ECG delay times⁷⁹. The ECG preparation scan uses an incremental delay relative to the R-wave trigger with 20 increments to cover the entire cardiac cycle.

As for the standard GE product FBI sequence, the adaptive refocus technique using variable refocusing flip angles (see Chapter 2.4.3) was used to increase flow sensitivity in prospective 3D FBI acquisitions. The adaptive refocus technique was only applied in the systolic (dark-artery) acquisition with an initial flip angle of 105°; the diastolic (bright-artery) acquisition used a constant flip angle of 180°. No flow-spoiled gradients were used for prospective acquisitions with the image matrix size of $320 \times 320 \times 80$.

Weak flow-spoiled gradients⁸⁰, together with the adaptive refocus technique, were applied in fully sampled acquisitions with a smaller matrix size ($224 \times 224 \times 80$). Flow-spoiled gradients were applied along the readout direction in both systolic and diastolic acquisitions with a strength of 10% (the percentage of one-half the area of the readout gradient). The readout direction is applied in parallel with the vessel orientation, which is the superior-inferior direction.

For the prospective acceleration, a CS accelerated FBI pulse sequence using self-designed patterns was developed on GE's EPIC programming platform. Ten groups of prospectively accelerated images were acquired from ten subjects, each with four datasets accelerated by 10×, 15×, 20× and 25× respectively. For the retrospective simulated study, ten fully sampled femoral FBI datasets were acquired from ten subjects and accelerated using AFs from 4 to 20. Simulated undersampling was then performed on fully sampled datasets. CS, PI and PF sampling were combined together to accelerate FBI acquisitions using the undersampling patterns designed based on the optimal ranges of parameters determined in Chapter 5 (values listed in Table 6.2). Additional details of the FBI acquisitions are listed in Table 6.2.

6.3.2 CS reconstruction

All datasets were firstly compressed into four virtual channels to reduce computation burden (see details in Section 6.3.3). All the reconstructions are based on the Split-Bregman algorithm, together with POCS iterations for the L1-SPIRiT reconstruction (see Section 3.4.3). The reconstruction program was developed based on the original Split-Bregman code provided by Ziwu Zhou (University of California, Los Angeles) and the original L1-SPIRiT code provided by Michael Lustig (University of California, UC Berkeley). Finite-differences were used as the sparsifying transform. The inner and outer iterations were both set to a fixed number. The Split-Bregman algorithm has a rapid convergence, allowing CS reconstruction in a small iteration number. In this study, the full CS reconstruction has ten iterations in total, with five inner iterations and two outer iterations. The fast CS reconstruction has only two iterations with no inner iterations. The homodyne detection for PF sampling was incorporated in the reconstruction (see Section 3.4.4).

The images evaluated in this study were reconstructed offline on a 64-bit PC using the CPU (Core i7-6700 with 4 Core/3.4 GHz, 40 GB RAM). The total reconstruction time was 2–3 minutes. For the prospective study, an automated inline reconstruction was also implemented on the MRI system, with six iterations in total for the Split-Bregman algorithm. This reconstruction took approximately two minutes, allowing the operator to see the reconstructed images while the subject was still on the table. All the reconstructions were implemented in MATLAB (R2019a, Mathworks Inc., Natick, MA). The performance of the fast partial CS reconstruction was evaluated and compared with the full CS reconstruction and 3D FFT.

The weighting parameters in Equations 6.1–6.4 were optimised in a separate pilot study. Since the calibration consistency term was solved by the POCS iterations without using its weighting parameter γ , only λ and μ (only for CMS) needed to be optimised; this optimisation was performed by retrospectively undersampling k -space using a range of parameter values, and then maximising the PSNR between CS reconstructed images and the fully sampled reference images. All raw k -space data were normalised by their maximum image intensity prior to reconstruction, which allows the same weighting parameters to be used for a large range of MRA datasets¹⁰². The optimised weighting parameters were fixed for the rest of our study.

6.3.3 Coil compression and coil combination

The data in this study were acquired using a 32-channel or 8-channel coil array. The large channel number creates a large computation burden. A coil compression algorithm¹⁷⁷ was used

to compress data from 32 or 8 channels into fewer virtual channels before the image reconstruction. The coil compression program used in this study was provided from Tao Zhang at Stanford University.

Following CS reconstruction, the reconstructed individual channel images need to be combined into a single composite image with full FOV. An adaptive combination method¹⁷⁸ was used in this study, and its performance is compared with the standard root-sum-of-squares (RSS) technique. The adaptive combination program used in this study was provided from Ricardo Otazo at New York University.

The performance evaluation was performed on three fully sampled datasets with 32 channels. The data were firstly compressed into virtual channels with the number of channels ranging from 2 to 32. Then, the compressed data were undersampled retrospectively using an AF of 10 \times and reconstructed. The reconstructed individual channel images were combined into a single image using either adaptive combination or RSS. The optimal number of virtual channels was determined by evaluating quantitative results.

6.3.4 Central region of k -space

The central region of k -space has three purposes. Firstly, SPIRiT requires a fully sampled centre region to calculate the linear combination weights for PI reconstruction. This region can be obtained from BB, DB or subtracted data. Secondly, the phase correction procedure requires a symmetric central region of k -space to estimate the background phase reference, which can be provided by either BB or DB data. Finally, the adaptive channel combination method also requires low-resolution reference images for calculating the weights for combining coil elements, which can be obtained from the central region of BB, DB or subtracted data.

In this study, the central region for SPIRiT reconstruction and adaptive combination of coil elements was obtained from BB data, while the central region for phase correction was obtained from DB data. The performance of reconstructions using the central regions selected from different data and with different sizes was evaluated and compared.

6.3.5 Image assessment

For the retrospective study, simulated accelerated images were evaluated using the four objective quantitative metrics described in Chapter 3, which are PSNR, SSIM, CNR of artery-to-background and sharpness assessment. The fully sampled images are used as the reference

images in PSNR, SSIM and CNR of artery-to-background. The reconstruction methods were categorised into two groups: those with intensity correction and those without it. To achieve fair comparisons, the same reference images were used for different reconstruction methods in each group. The reference images were defined as the average of the fully sampled images reconstructed by different methods, *i.e.*, for the evaluation of KSPIC, MS-IC and CMS-IC, the reference images were the average of images reconstructed by KSPIC, MS-IC and CMS-IC, while for the evaluation of KSPC, KS, MS and CMS, the reference images were the average of images reconstructed by KSPC, KS, MS and CMS. These averaged images were used in this way because of the difficulty of determining a reasonable reconstruction method for creating reference images. For example, using the reconstruction with intensity and phase correction as the reference could be unfair for the other reconstructions without intensity or phase correction, leading to a very large error or low similarity; and similarly using reconstructions based on *k*-space subtraction could be unfair for the reconstructions based on magnitude subtraction. Also, using different reconstructions for different reference images (same as the reconstruction method to be evaluated) is not feasible, because images reconstructed by the methods without phase correction may contain unwanted artefacts and should not be considered as reference images. The other details of the metric implementations are the same as used in Section 5.4.2. For the prospective study, MIPs of the images reconstructed by four different methods were assessed by two experienced radiologists in a randomised order. The radiologists were blinded to reconstruction methods and AFs. Three separate aspects of the images were graded: vessel delineation; image noise and artefacts; and background and venous contamination. The criteria for scoring are as follows:

Vessel delineation

1=non-diagnostic delineation, poor delineation of all-sized arteries

2=acceptable delineation of main/large arteries but impaired delineation of intermediate and small arteries.

3=good display of main/large arteries but impaired delineation of small branches

4=excellent arterial display with good delineation of all-size arteries

Image artefacts

1=severe artefact and/or noise leading to non-diagnostic images

2=moderate artefact and/or noise, impairing the definition of the fine structures of vessels

3=mild artefact and/or noise, but not impairing the delineation of vessels

4=excellent artefact and noise suppression

Background and venous contamination

1=severe background or venous contamination affecting diagnosis

2=moderate background or venous contamination

3=minimal background or venous contamination but not affecting diagnosis

4=excellent background and signal suppression

6.3.6 Statistics analysis

Statistical analysis evaluated differences between KSPIC/KSPC and the other reconstruction methods. For subjective image quality scores, Wilcoxon signed-rank tests were performed to identify pairwise differences between KSPIC and MS, KS and CMS-IC respectively. For quantitative metrics results, paired Student's *t*-tests were performed to assess pairwise differences between KSPIC/KSPC and the other reconstructions at 4×, 12× and 20×. Pairwise comparisons include KSPIC vs MS-IC, KSPIC vs CMS-IC, KSPC vs MS, KSPC vs KS, KSPC vs CMS. Statistical significance was defined at $P < 0.05$ in all tests.

Table 6.2 Parameters used in retrospective and prospective studies.

| Study | Number of datasets | Common protocol parameters | Respective protocol parameters | Acceleration parameters | AFs and acquisition times |
|---------------------|---|---|---|--|---|
| Retrospective study | 10 fully sampled datasets | FOV 400–420 mm ² ; R-R interval: 2/3 heartbeats depending on the heart-rate; Fat suppression: short-time inversion recovery (STIR) with an inversion time of 174 ms; Flip angle: 90°; Refocus angle: 180°. | Matrix size: 224(x) × 224(y) × 80(z); Slice thickness: 2 mm; Bandwidth: ±62.5 kHz; Echo train length: 80; TE _{eff} : 30 ms; Flow dephasing: variable flip angle and flow-spoiled gradients (10%). | Fully sampled acquisitions: fully sampled ellipsoidal <i>k</i> -space without acceleration. Retrospective simulations: Poisson-disk sampling patterns with the optimised parameters in Table 5.2, Section 5.5.7. | Retrospective AFs: 4×, 6×, 8×, 10×, 12×, 14×, 16×, 18× and 20×. Acquisition time of fully sampling: 314 or 352 TR (692–1182 heart beats) |
| Prospective study | 10 groups of undersampled datasets with different AFs | | Matrix size: 320(x) × 320(y) × 80(z); Slice thickness: 1.8–2.0 mm; Bandwidth: ±83.3 kHz; Echo train length: 60–70; TE _{eff} : 45 ms; Flow dephasing: variable flip angle. | Poisson-disk sampling patterns with the following parameters: Density decay factor: 0.1 for all AFs; PF ratio: 0.6–0.7 in <i>k_y</i> , 0.7–0.75 in <i>k_z</i> ; Fully sampled centre region: 24×12 for all AFs. | Prospective AFs: 10×, 15×, 20× and 25×; Corresponding acquisition times: 152–276, 104–192, 80–144 and 64–120 heart beats. |
| ECG prep scan | One acquisition for each examination | | Matrix size: 256(x) × 128(y); Section thickness: 150 mm; TE _{eff} : 80 ms Number of phases: 20 | PI and PF sampling | Acquisition time: 1–2 minutes |

Acquisition times vary due to different heart-rates, number of beats per TR and ETL.

6.4 Results

6.4.1 Retrospective simulation

Figure 6.3 shows quantitative evaluation results of the seven different methods. The corresponding values and statistics evaluations are summarised in Table 6.3 and Table 6.4 (only at 4 \times , 12 \times and 20 \times).

PSNR, SSIM and CNR of artery-to-background

KS with phase correction has the best performance in terms of SSIM and CNR of artery-to-background both with intensity correction (KSPIC) and without intensity correction (KSPC). The PSNR values of CMS/CMS-IC and MS/MS-IC are higher when the AF<8 but decrease rapidly with increasing AF. KS has low PSNR and CNR especially at small AFs, which is mainly due to the artefacts caused by negative signals with reversed polarity. Compared with MS/MS-IC, CMS/CMS-IC has larger CNR but lower SSIM values. The PSNR of CMS/CMS-IC is between that of KSPC/KSPIC and MS/MS-IC—higher than MS/MS-IC but lower than KSPC/KSPIC when the AF<8, and lower than MS/MS-IC but higher than KSPC/KSPIC when the AF>8.

In comparisons between KSPC/KSPIC and other reconstructions, significant differences existed in all cases except the PSNR of CMS at 4 \times , SSIM of KS at 20 \times , CNR of CMS at 4 \times and PSNR of CMS-IC at 12 \times .

Sharpness

The *k*-space subtraction methods (KSPC/KSPIC and KS) have significantly better sharpness than magnitude subtraction methods (MS/MS-IC and CMS/CMS-IC). No significant differences were found between KS and KSPC.

Example images

Figure 6.4 shows example results of KS, MS, CMS-IC and KSPIC in fully sampled and retrospectively accelerated datasets using the AF from 4 to 20. KSPIC achieved good and consistent image quality over the range of different AFs. Noticeable image degradation in terms of increased artefacts, residual background tissue and impaired vessel delineations can be observed in KS, MS and CMS-IC, especially when the AF is large.

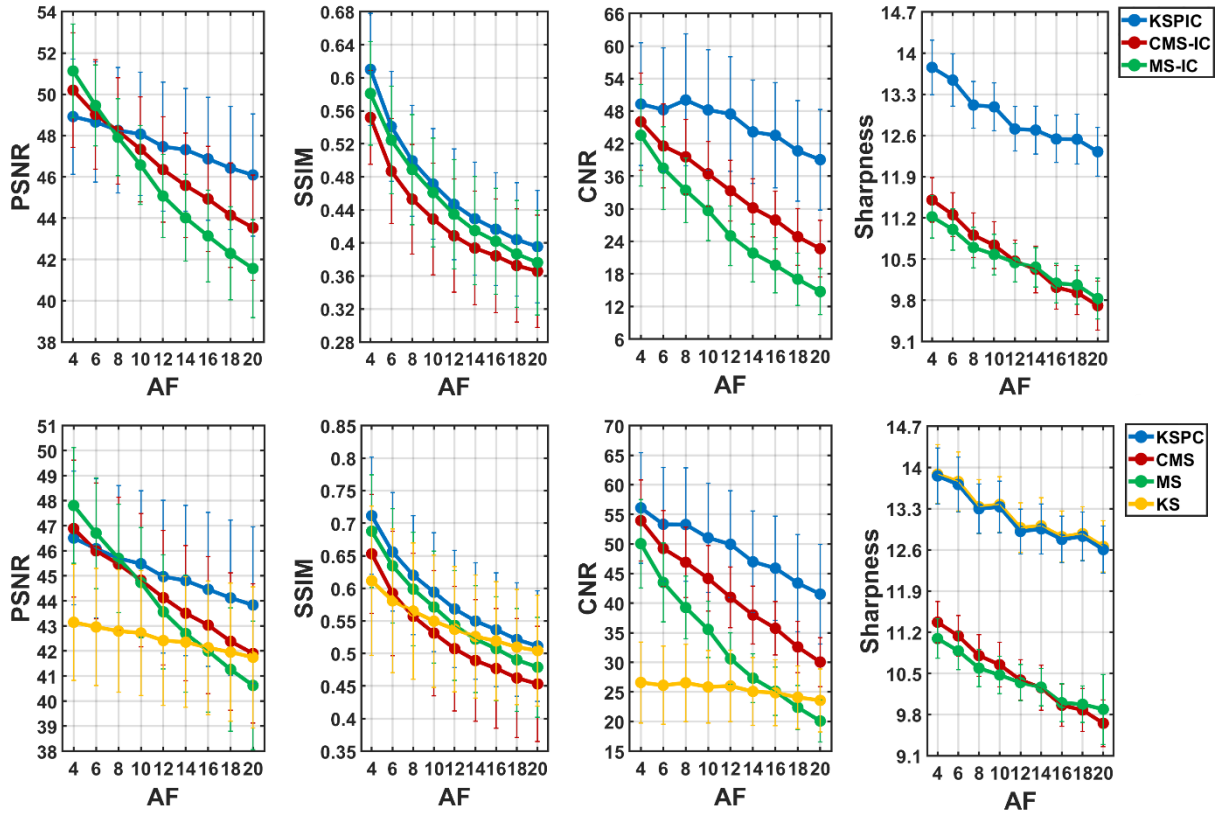


Figure 6.3 Plots summarising quantitative evaluation of simulated acceleration. PSNR, SSIM, CNR of artery-to-background and sharpness versus the AF were calculated for the different reconstructions. Top row: reconstructions with intensity correction including KSPIC, MS with post-processing intensity correction and CMS with post-processing IC. Bottom row: reconstructions without intensity correction including KS with phase correction, CMS, conventional MS and conventional KS. The values are the mean and standard deviation calculated over the 10 volunteer datasets.

Table 6.3 Quantitative analysis results (mean \pm standard deviation) of KS, MS, CMS and KSPC. Images were retrospectively accelerated by 4 \times , 12 \times and 20 \times from 10 volunteer datasets.

| PSNR | | | | | | | | | | | | |
|-----------------------------|-------|---|---------------------|-------|---|---------------------|-------|---|---------------------|-------|---|------|
| | KS | | | MS | | | CMS | | | KSPC | | |
| 4× | 43.14 | ± | 2.46 ^(a) | 47.81 | ± | 2.45 ^(a) | 46.89 | ± | 2.90 | 46.51 | ± | 2.84 |
| 12× | 42.41 | ± | 2.74 ^(a) | 43.56 | ± | 2.42 ^(a) | 44.13 | ± | 2.85 ^(a) | 44.97 | ± | 3.24 |
| 20× | 41.75 | ± | 2.99 ^(a) | 40.62 | ± | 2.72 ^(a) | 41.90 | ± | 2.95 ^(a) | 43.83 | ± | 3.32 |
| | | | | | | | | | | | | |
| SSIM | | | | | | | | | | | | |
| | KS | | | MS | | | CMS | | | KSPC | | |
| 4× | 0.61 | ± | 0.12 ^(a) | 0.69 | ± | 0.09 ^(a) | 0.65 | ± | 0.10 ^(a) | 0.71 | ± | 0.10 |
| 12× | 0.54 | ± | 0.10 ^(a) | 0.54 | ± | 0.09 ^(a) | 0.51 | ± | 0.10 ^(a) | 0.57 | ± | 0.10 |
| 20× | 0.50 | ± | 0.09 | 0.48 | ± | 0.08 ^(a) | 0.45 | ± | 0.09 ^(a) | 0.51 | ± | 0.09 |
| | | | | | | | | | | | | |
| CNR of artery-to-background | | | | | | | | | | | | |
| | KS | | | MS | | | CMS | | | KSPC | | |
| 4× | 26.60 | ± | 7.25 ^(a) | 50.05 | ± | 7.93 ^(a) | 53.95 | ± | 7.26 | 56.09 | ± | 9.89 |
| 12× | 26.01 | ± | 6.42 ^(a) | 30.60 | ± | 4.63 ^(a) | 40.99 | ± | 5.44 ^(a) | 49.95 | ± | 9.57 |
| 20× | 23.57 | ± | 5.63 ^(a) | 20.09 | ± | 3.75 ^(a) | 30.05 | ± | 4.40 ^(a) | 41.53 | ± | 8.91 |
| | | | | | | | | | | | | |
| Sharpness | | | | | | | | | | | | |
| | KS | | | MS | | | CMS | | | KSPC | | |
| 4× | 13.89 | ± | 0.53 | 11.09 | ± | 0.35 ^(a) | 11.37 | ± | 0.37 ^(a) | 13.86 | ± | 0.50 |
| 12× | 12.98 | ± | 0.45 | 10.34 | ± | 0.32 ^(a) | 10.39 | ± | 0.36 ^(a) | 12.91 | ± | 0.41 |
| 20× | 12.66 | ± | 0.46 | 9.89 | ± | 0.63 ^(a) | 9.65 | ± | 0.42 ^(a) | 12.61 | ± | 0.43 |

^a Denotes statistical significance (two-tailed paired Student's *t*-test, $P < 0.05$) when compared with the proposed KSPC method at the same acceleration.

Table 6.4 Quantitative analysis results (mean \pm standard deviation) of MS-IC, CMS-IC and KSPIC. Images were retrospectively accelerated by 4 \times , 12 \times and 20 \times from 10 volunteer datasets.

| PSNR | | | | | | |
|-----------------------------|-------|---------------------------|--|--------|---------------------------|-------------------|
| | MS-IC | | | CMS-IC | | KSPIC |
| 4 \times | 51.16 | \pm 2.38 ^(a) | | 50.26 | \pm 2.92 ^(a) | 48.87 \pm 3.00 |
| 12 \times | 45.09 | \pm 2.14 ^(a) | | 46.36 | \pm 2.70 | 47.42 \pm 3.33 |
| 20 \times | 41.57 | \pm 2.51 ^(a) | | 43.54 | \pm 2.71 ^(a) | 46.06 \pm 3.16 |
| SSIM | | | | | | |
| | MS-IC | | | CMS-IC | | KSPIC |
| 4 \times | 0.55 | \pm 0.07 ^(a) | | 0.58 | \pm 0.06 ^(a) | 0.61 \pm 0.07 |
| 12 \times | 0.41 | \pm 0.07 ^(a) | | 0.44 | \pm 0.07 ^(a) | 0.45 \pm 0.07 |
| 20 \times | 0.37 | \pm 0.07 ^(a) | | 0.38 | \pm 0.07 ^(a) | 0.40 \pm 0.07 |
| CNR of artery-to-background | | | | | | |
| | MS-IC | | | CMS-IC | | KSPIC |
| 4 \times | 43.54 | \pm 9.94 ^(a) | | 46.04 | \pm 9.51 ^(a) | 49.30 \pm 11.98 |
| 12 \times | 25.00 | \pm 5.85 ^(a) | | 33.31 | \pm 5.92 ^(a) | 47.46 \pm 11.17 |
| 20 \times | 14.73 | \pm 4.47 ^(a) | | 22.64 | \pm 5.57 ^(a) | 39.04 \pm 9.81 |
| Sharpness | | | | | | |
| | MS-IC | | | CMS-IC | | KSPIC |
| 4 \times | 11.22 | \pm 0.38 ^(a) | | 11.50 | \pm 0.40 ^(a) | 13.76 \pm 0.49 |
| 12 \times | 10.44 | \pm 0.34 ^(a) | | 10.46 | \pm 0.38 ^(a) | 12.71 \pm 0.40 |
| 20 \times | 9.83 | \pm 0.37 ^(a) | | 9.71 | \pm 0.44 ^(a) | 12.32 \pm 0.44 |

^a Denotes statistical significance (two-tailed paired Student's *t*-test, $P < 0.05$) when compared with the proposed KSPIC method at the same acceleration.

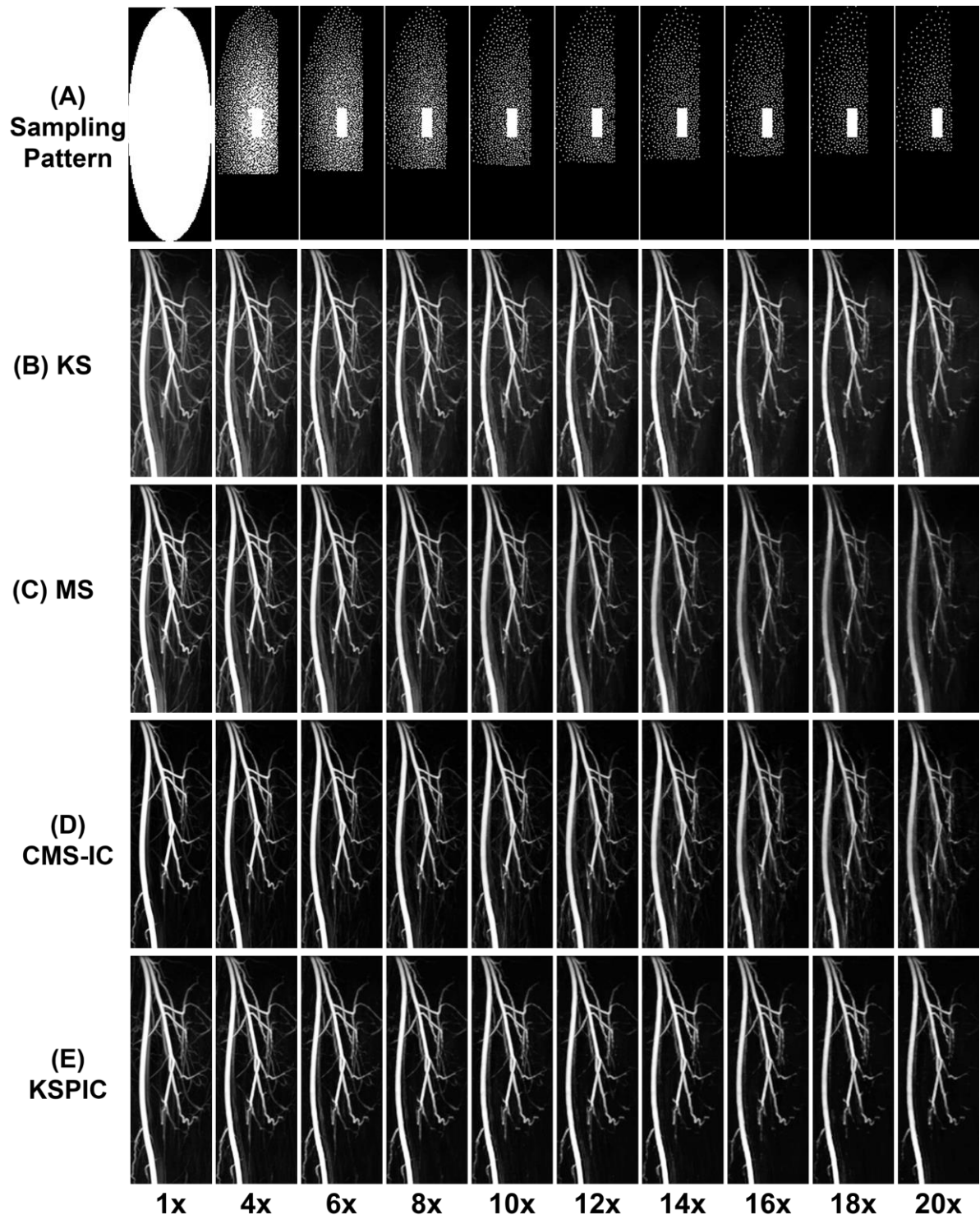


Figure 6.4 Example images of retrospective simulated accelerations using different reconstructions. A: Sampling patterns with the AF from 4 to 20. B–E: MIPs (left femoral arteries) of images reconstructed by KS, MS, CMS-IC and KSPIC respectively.

6.4.2 Prospective acquisition

Example MIPs from two healthy volunteers are demonstrated in Figure 6.5. All the four methods achieved good image quality at 10× acceleration, but image blurring and artefacts appear on MS and CMS-IC at 25× acceleration (yellow arrowheads). Compared with magnitude subtraction methods, KS has good noise suppression and less venous contamination, but impaired delineations of small branches can be observed on KS images (red arrowheads). Residual background tissues, such as veins, can be observed on the MS and KS images. CMS-IC has improved background suppression by employing IC, while KSPIC has the best suppression.

Subjective image quality scores are summarised in Figure 6.6 and Table 6.5. Subjective scores show good agreement with the objective evaluation results using quantitative metrics in the retrospective study. KSPIC achieved the highest scores in all three performance metrics including vessel delineation, image artefacts, and background and venous contamination. The high scores are maintained at large AFs. No significant differences were observed between 10× acceleration and other larger AFs except the vessel delineation score at 25×.

MS and CMS-IC have lower scores, and their performance degrades rapidly with increasing AF. KS has good suppression of noise, artefacts and also background signals, but shows poor vessel delineation. Significant differences were found in all cases between KSPIC and the other reconstructions except the image artefacts and background contamination scores of CMS-IC at 10×, and the background contamination scores of KS at 20× and 25×.

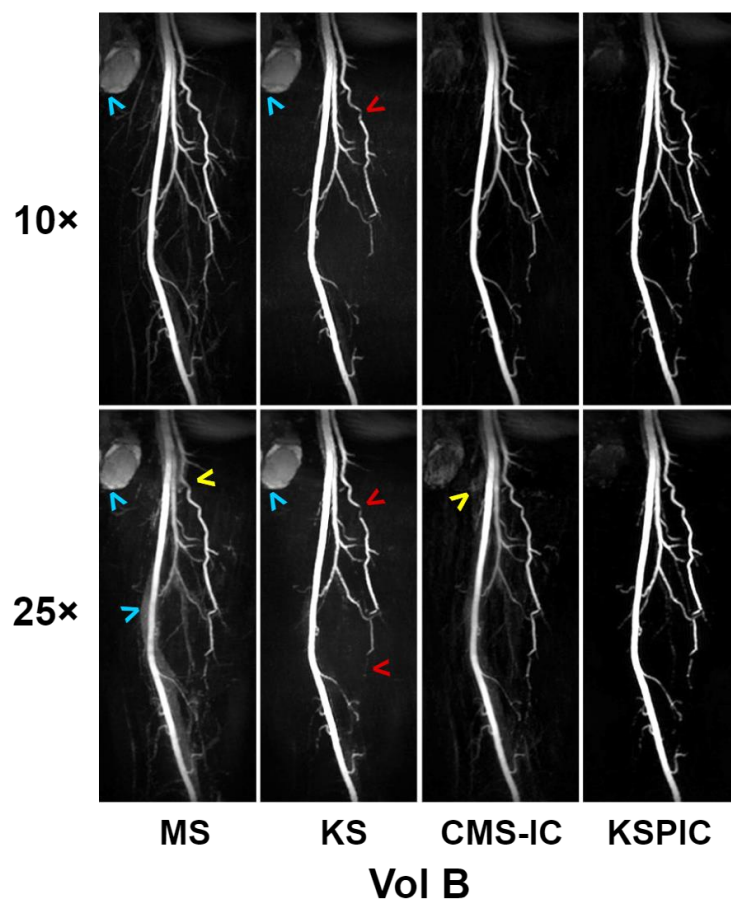
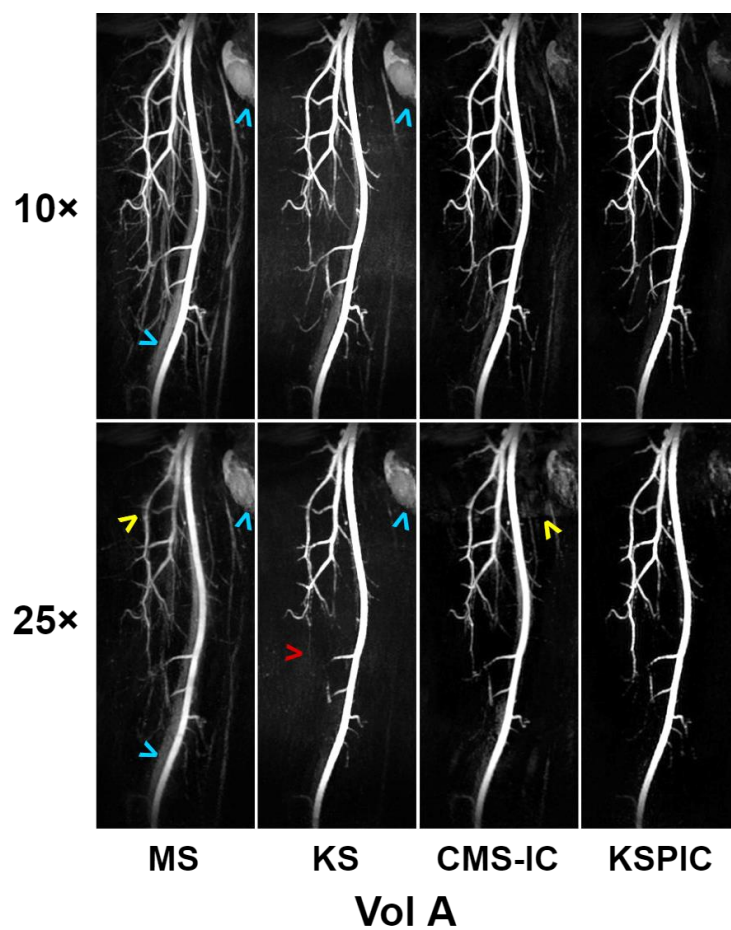


Figure 6.5 Example MIP images of prospectively accelerated acquisitions from two healthy volunteers using AFs of 10× and 25× with KS, MS, CMS-IC and KSPIC. The blue arrowheads denote residual veins and other background tissues on KS and MS images; the yellow arrowheads denote image blurring or artefacts caused by undersampling with a high AF on MS and CMS-IC images; the red arrowhead denotes impaired depiction of small branches on KS image.

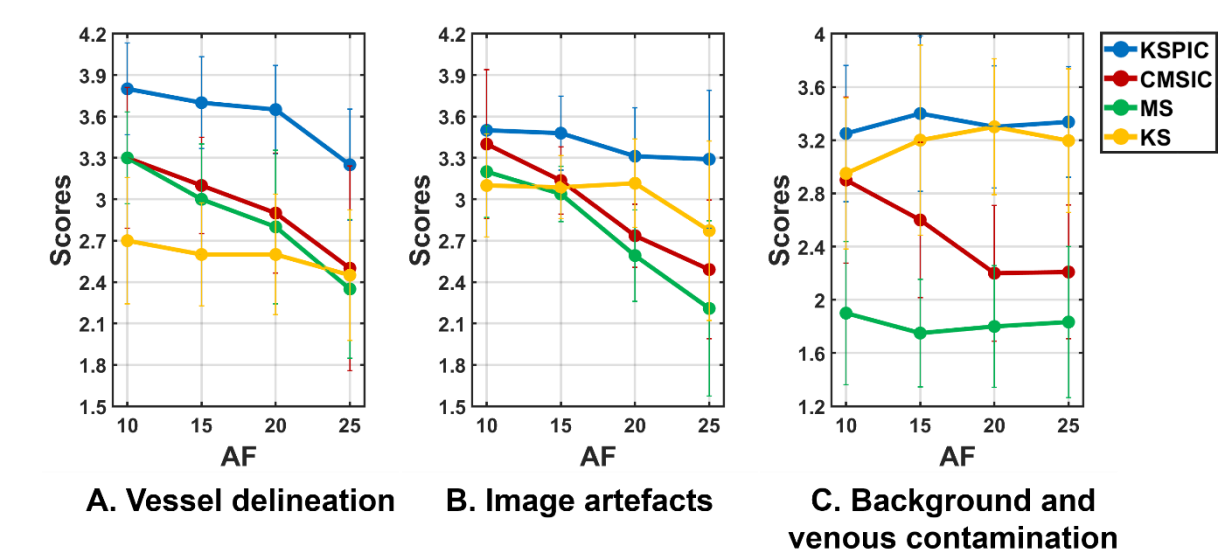


Figure 6.6 Plots summarising subjective image quality scores (1–4 scales) in terms of vessel delineation, noise and artefacts, and background and venous contamination on the images prospectively accelerated by 10×, 15×, 20× and 25×. The values are the mean and standard deviation calculated over the 10 volunteer datasets.

Table 6.5 Subjective scores (mean \pm standard deviation) of images prospectively accelerated by 10 \times , 15 \times , 20 \times and 25 \times from 10 volunteer datasets.

| Vessel delineation | | | | | | | | | | | |
|-------------------------------------|-------|---|---------------------|--------|---|------------------------|------|---|------------------------|------|--------------------------|
| | KSPIC | | | CMS-IC | | | MS | | | KS | |
| 10× | 3.80 | ± | 0.33 | 3.30 | ± | 0.51 ^(a) | 3.30 | ± | 0.33 ^(a) | 2.70 | ± 0.46 ^(a) |
| 15× | 3.70 | ± | 0.33 | 3.10 | ± | 0.35 ^(a) | 3.00 | ± | 0.40 ^(a) | 2.60 | ± 0.37 ^(a) |
| 20× | 3.65 | ± | 0.32 | 2.90 | ± | 0.44 ^(a) | 2.80 | ± | 0.56 ^(a, b) | 2.60 | ± 0.44 ^(a) |
| 25× | 3.25 | ± | 0.40 ^(b) | 2.50 | ± | 0.74 ^(a, b) | 2.35 | ± | 0.50 ^(a, b) | 2.45 | ± 0.47 ^(a) |
| Image artefacts | | | | | | | | | | | |
| | KSPIC | | | CMS-IC | | | MS | | | KS | |
| 10× | 3.50 | ± | 0.00 | 3.40 | ± | 0.54 | 3.20 | ± | 0.33 ^(a) | 3.10 | ± 0.37 ^(a) |
| 15× | 3.48 | ± | 0.27 | 3.14 | ± | 0.24 ^(a) | 3.04 | ± | 0.20 ^(a) | 3.09 | ± 0.23 ^(a) |
| 20× | 3.31 | ± | 0.35 | 2.74 | ± | 0.23 ^(a) | 2.59 | ± | 0.33 ^(a, b) | 3.12 | ± 0.32 ^(a, b) |
| 25× | 3.29 | ± | 0.50 | 2.49 | ± | 0.50 ^(a) | 2.21 | ± | 0.63 ^(a, b) | 2.77 | ± 0.65 ^(a, b) |
| Background and venous contamination | | | | | | | | | | | |
| | KSPIC | | | CMS-IC | | | MS | | | KS | |
| 10× | 3.25 | ± | 0.51 | 2.90 | ± | 0.62 | 1.90 | ± | 0.54 ^(a) | 2.95 | ± 0.57 ^(a) |
| 15× | 3.40 | ± | 0.58 | 2.60 | ± | 0.58 ^(a) | 1.75 | ± | 0.40 ^(a) | 3.20 | ± 0.71 ^(a) |
| 20× | 3.30 | ± | 0.46 | 2.20 | ± | 0.51 ^(a, b) | 1.80 | ± | 0.46 ^(a) | 3.30 | ± 0.51 |
| 25× | 3.34 | ± | 0.42 | 2.21 | ± | 0.5 ^(a, b) | 1.83 | ± | 0.57 ^(a) | 3.20 | ± 0.54 |

^a Denotes statistical significance (Wilcoxon signed-rank test, $P < 0.05$) when compared with the proposed KSPIC method at the same acceleration.

^b Denotes statistical significance (Wilcoxon signed-rank test, $P < 0.05$) when compared with 10 \times acceleration using the same reconstruction method.

6.4.3 Phase correction

The following results show the effect of the phase correction procedure using data from the retrospective acceleration study. Figure 6.7 shows MIPs of reconstructions using k -space subtraction with (KSPC, panel A) and without phase correction (KS, panel C). Intensity correction was not applied in either of these two reconstructions. The error maps of different reconstructions are obtained by calculating the difference between the accelerated images and the fully sampled reference images (panel B and D). Panel E shows the magnitudes of negative values on the reconstructed images with restored polarity, *i.e.*, the negative signals which are removed from the KSPC images. Background artefacts can be observed on the KS image without phase correction, coincided with the location of the negative signals (red dashed circle). This proves that the background artefacts are caused by negative signals which lose their polarity during reconstruction. These artefacts, although not strong, can obscure branch vessels with low SI on the MIP. Phase correction removed these artefacts and generated a darker and clearer background. Apart from background artefacts caused by polarity reversal, high error vascular regions can be seen on panel D (red arrowheads), which are caused by the distortions and arterial signal loss due to inaccurate phase estimation of arteries.

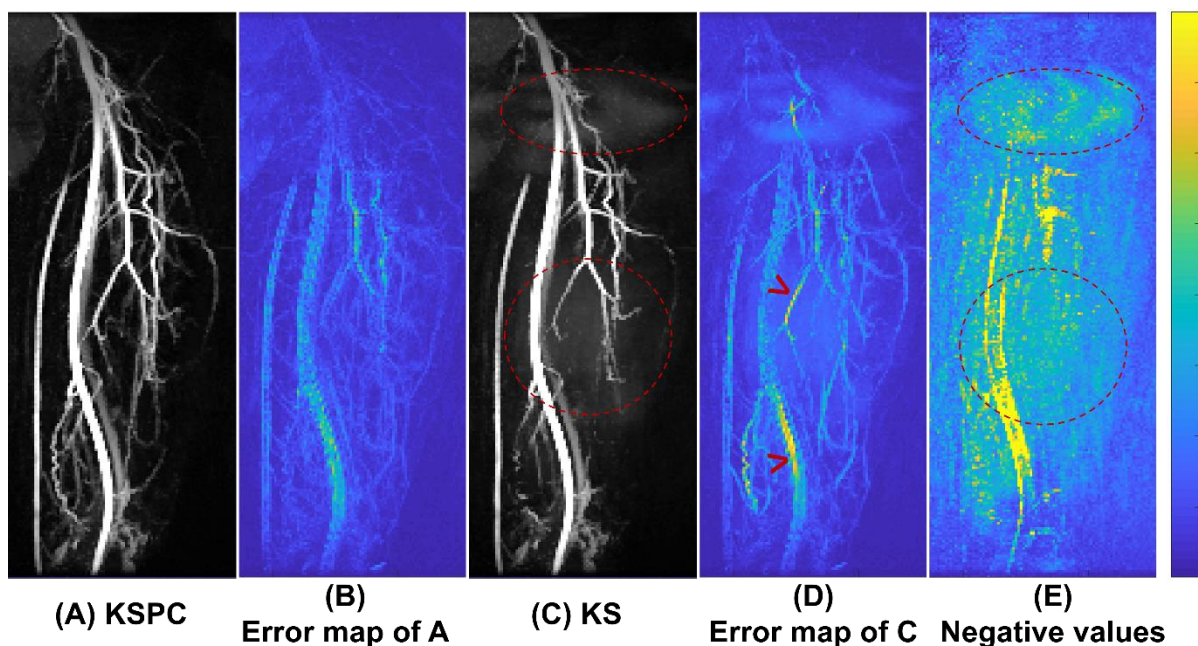


Figure 6.7 Example MIPs of reconstructions using k -space subtraction with phase correction (KSPC, panel A) and without phase correction (KS, panel C). Panel B and D show the error maps using the fully sampled reference images as the reference. Panel E is the MIP showing only the magnitudes of negative values on the reconstructed images with restored polarity. Background artefacts due to the loss of polarity can mask some small arteries in the KS reconstruction. The background artefacts coincided with the

location of negative signals (red arrowheads). Some local vascular regions show higher error values on the KS image (white arrowheads).

Figure 6.8 shows the quantitative evaluation of KSPIC reconstructions using the central region acquired from different data sources. SPIRiT kernel calculations based on the different data sources do not show much difference in PSNR and SSIM but show slightly different trends in CNR of artery-to-background. For adaptive channel combination (B) using the central region acquired from BB or DB images shows higher CNR of artery-to-background than using the central region acquired from subtracted angiograms. For phase correction (C), reconstruction using the background phase reference from DB data shows higher PSNR and SSIM but slightly lower CNR, which will be explained in the discussion with reference to Figure 6.9 and Figure 6.10.

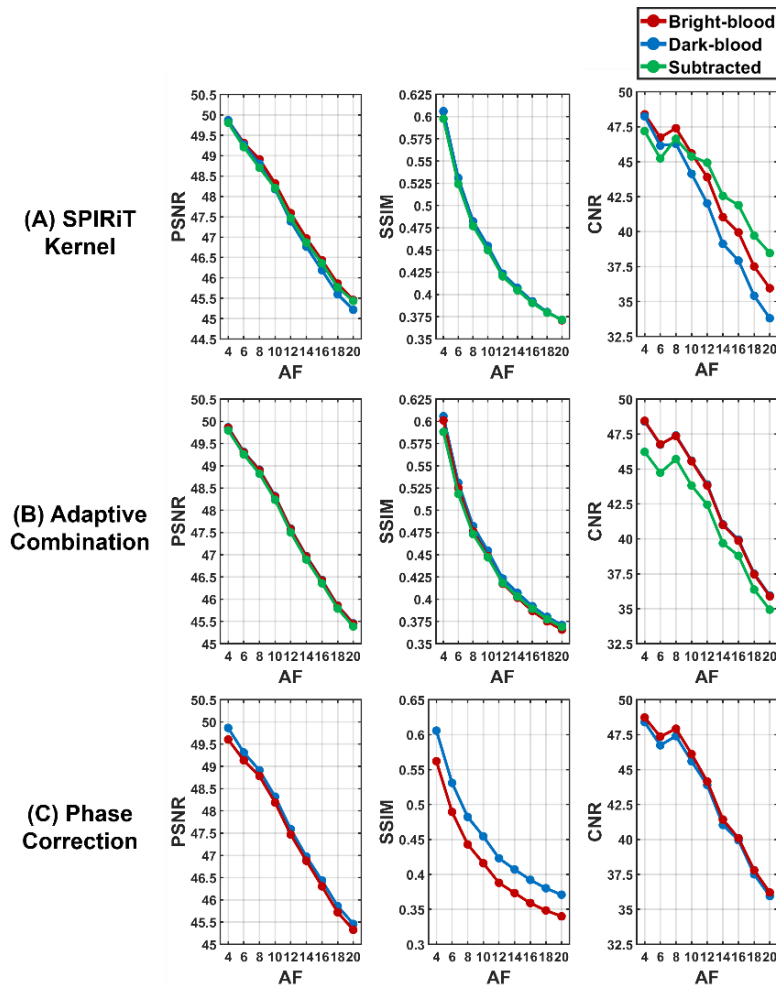


Figure 6.8 Quantitative evaluation of KSPIC reconstructions using the central region acquired from different data sources for (A) SPIRiT kernel calculation, (B) weights calculation in adaptive channel

combination, and (C) background phase reference in phase correction. The average values across 10 datasets are shown.

Figure 6.9 shows an example of reconstructed images using the background phase reference from BB (A and C) and DB (B and D) data in phase correction. Artefacts caused by incoherent undersampling can be observed on images using the phase reference from BB data, especially on the axial slices which contain high SI tissues with large areas, such as the testis (C and the yellow arrowheads on A). These artefacts were largely reduced by using the phase reference from DB data.

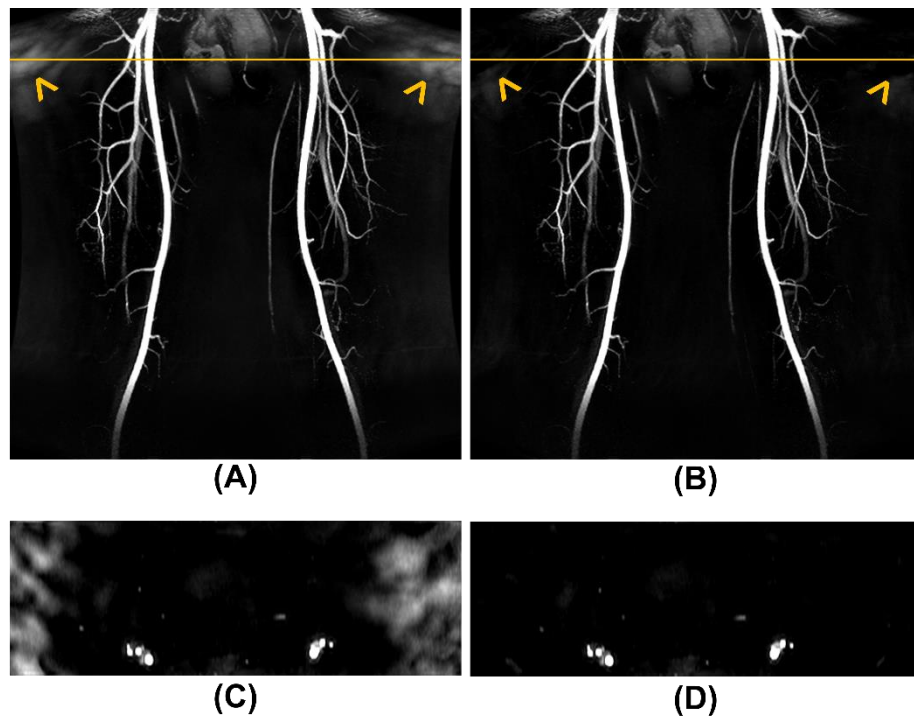


Figure 6.9 An example of reconstructed images using phase reference from BB (A and C) and DB (B and D) data. A and B are coronal MIPs, where the yellow arrowheads denote background artefacts which are more extensive on A. C and D are axial slices corresponding to the location denoted by the yellow lines on A and B respectively.

The evaluation of the effect of the size of the central k -space region used for phase estimation (phase correction region) is shown in Figure 6.10. The quantitative evaluation shows that 12-20 was the optimal range of the region length (width=1/2 length) in this study (Figure 6.10A). Larger phase correction regions lead to rapid decreases of all the three measurements. In

particular, excessively detailed phase estimation leads to arterial phase change in the DB images (red arrowheads in Figure 6.10B), leading to central signal loss in the arteries (Figure 6.10C). The phase map obtained from the subtracted data contains inverted polarity and is corrupted by phase singularities, thus cannot be used as background phase reference (bottom row in Figure 6.10B).

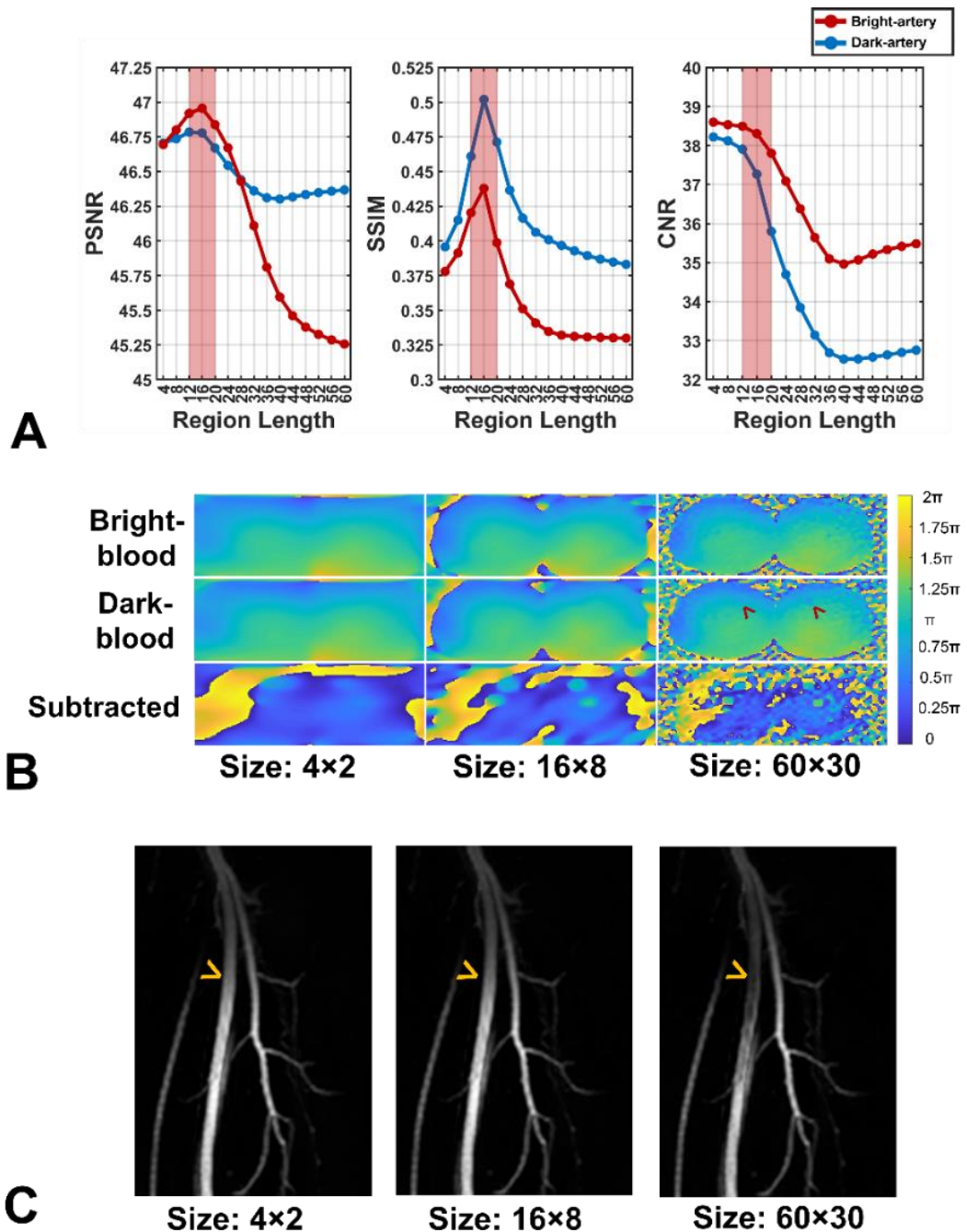


Figure 6.10 Evaluation of the phase correction region size. **A:** The quantitative evaluation of reconstructions with different lengths of phase correction region (length: width=2:1). **B:** Phase references acquired from BB, DB and subtracted data with different sizes of phase correction region. Red

arrowheads denote phase changes in arteries that can impair the arterial signal in reconstruction. **C:** Central signal loss in arteries using a large-size phase correction region from DB data (the yellow arrow on the right image).

6.4.4 Coil compression and coil combination

Figure 6.11 shows the performance of coil compression and coil image combination. The reconstructed individual channel images were combined into a single image using either adaptive combination or RSS. The adaptive combination has much higher scores in all three measurements, especially when the virtual channel number is small. For RSS, the PSNR and SSIM keep increasing with increasing numbers of virtual channels, while the quantitative measurements of adaptive combination achieve peak values at small virtual channel numbers. The evaluation results show that adaptive combination outperforms RSS and its use allows fewer compressed virtual channels without degradation in image quality. The coil compression process took an average computation time of 82.8 ± 12.2 seconds but greatly reduced the reconstruction time from 1168.7 ± 234.2 seconds at 32 channels to 43.3 ± 22.5 seconds for 4 virtual channels (the number used in this study).

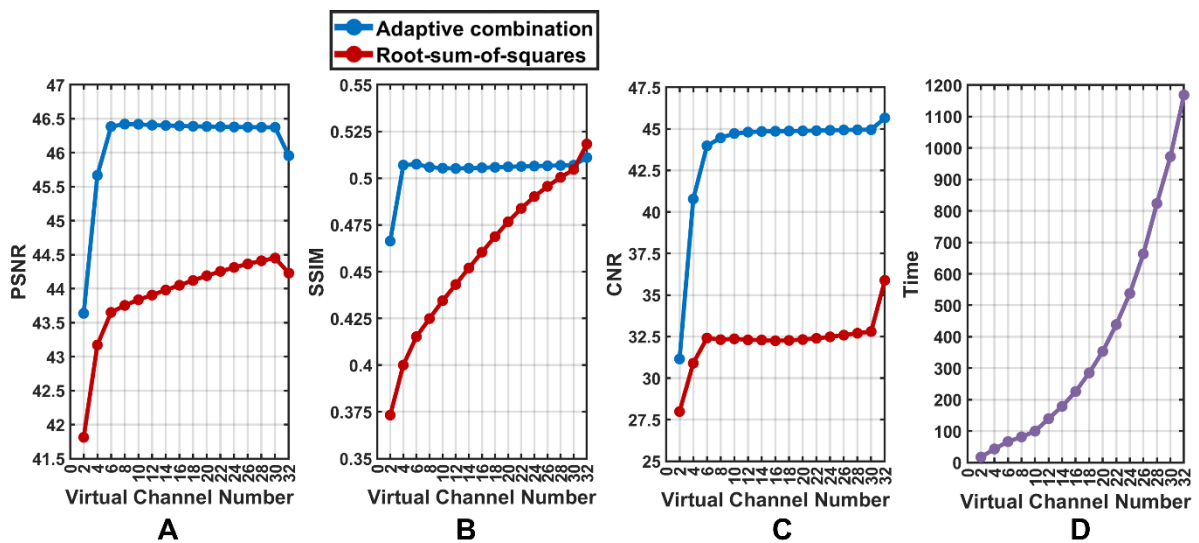


Figure 6.11 The quantitative evaluation results (A, B and C) and reconstruction time (D) of coil compression and coil image combination with different virtual channel numbers. The data from 32 channels were compressed into fewer virtual channels before the image reconstruction, and the reconstructed individual coil images were combined using either adaptive combination (blue line) or RSS (red line). The evaluation was performed on three datasets retrospectively undersampled using an AF of 10 \times .

6.4.5 Fast partial reconstruction and iteration numbers

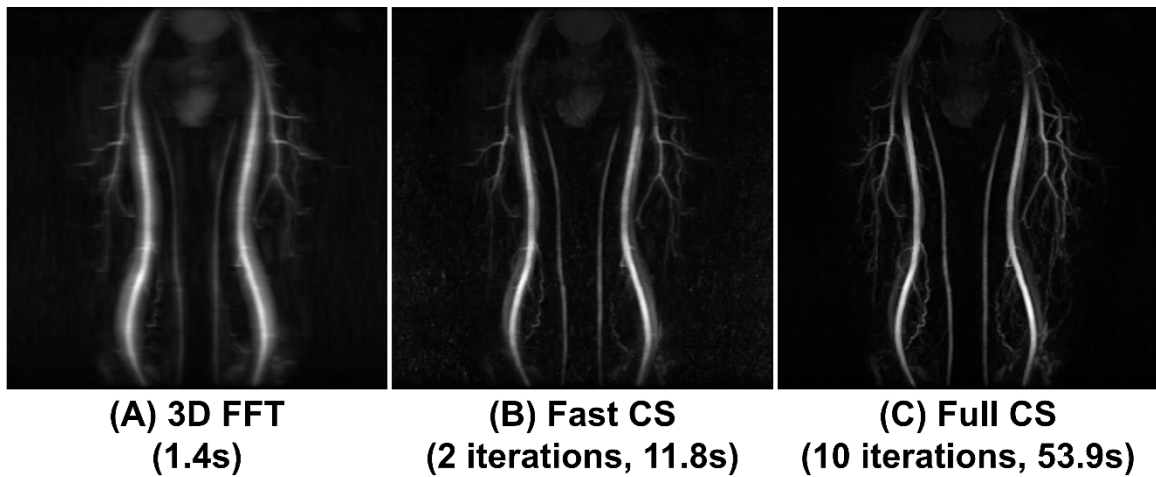


Figure 6.12 Example images reconstructed by 3D FFT (A), fast CS (B) and full CS (C).

Figure 6.12 shows example images (MIP) reconstructed by 3D FFT, fast CS and full CS (AF=10). Compared with 3D FFT (A), fast CS with only two iterations shows much better performance (B), which is close to the result of full CS reconstruction (C).

The reconstruction time of fast CS for intensity correction can be further reduced by applying it only to 10% axial slices of the k -space data (see Section 6.2.5). Table 6.6 summarises the evaluation of intensity correction incorporated with FFT, fast CS and full CS. Evaluation was performed on 11 retrospectively accelerated datasets at an AF of 10 \times . Compared with full CS, fast CS and FFT both greatly reduced the average computation time, from 80.2 seconds to 4.2 and 4.0 seconds respectively. Although both the results of FFT and fast CS showed no significant differences from the results of full CS, fast CS achieved lower bias, mean absolute error and higher Pearson correlation coefficients.

Table 6.6 Comparison of mean intensity correction coefficients calculated based on images reconstructed by FFT, fast CS and full CS.

| Statistics | FFT | Fast CS (10% data) | Full CS |
|--|--------------|-----------------------|-------------|
| Mean intensity correction coefficients | 1.091±0.068 | 1.010±0.069 | 1.105±0.062 |
| Bias | -0.014±0.023 | -0.006±0.016 | - |
| P-value | 0.09 | 0.30 | - |
| Mean absolute error | 0.017 | 0.012 | - |
| Pearson <i>r</i> value | 0.945 | 0.978 | - |
| Computation time (seconds) | 4.0±1.1 | 4.2±0.2 | 80.2±4.7 |

6.5 Discussion

In this study, a new reconstruction method based on *k*-space subtraction, KSPIC, was proposed for accelerated subtractive NCE-MRA. KSPIC applies the intensity correction procedure proposed in Chapter 4 prior to the full CS reconstruction and uses a phase correction procedure to restore the negative polarity and remove background artefacts.

Phase correction is inspired by the phase sensitive detection method used in inversion-recovery (IR) imaging^{172–176}. MR images are generally displayed as magnitude images, which avoids the need for correcting phase shifts in MR data caused by gradient ramping, eddy currents, motion, and the phase delay of electronic circuits¹⁷⁹. However, negative magnetisations in IR imaging, for example at short inversion times, are inverted to positive values by taking magnitudes. The same phenomenon exists in subtractive NCE-MRA, in which negative signals are produced by image subtraction.

When PF sampling is applied, the phase correction in KSPIC can be regarded as part of the process of the homodyne reconstruction but using the raw data instead of the subtracted data itself. It has been reported in a previous study that for reconstruction methods based on *k*-space subtraction, the low-resolution reference obtained from DB data can provide better performance than that from subtracted data in PF reconstruction, but the reasons and quantitative comparisons were not fully evaluated⁹⁶. From the perspective of PF reconstruction, using homodyne from

raw data has two main advantages. Firstly, the phase reference from subtracted data shows reversed phases of negative signals. Therefore, the reference cannot restore the polarity of negative signals but will invert them to positive values. In contrast, the phase reference acquired from raw data can preserve negative polarity and remove background artefacts by only showing positive signals. Secondly, as shown in Figure 6.10B (bottom row), the phase reference acquired from subtracted data is corrupted by phase singularities, which can affect the PF reconstruction. Signal loss and distortions of arteries can be found in some local regions in images reconstructed by KS using a phase reference from subtracted data.

The quantitative results show that the reconstruction using the background phase reference from DB data has slightly higher PSNR and SSIM (Figure 6.8) than for a BB phase reference. Using the phase reference from BB data shows improved suppression of artefacts out of the subject (Figure 6.9). This can be explained by the subtraction and reconstruction scheme of KSPIC: artefacts due to undersampling can be generated in BB and/or DB data individually, especially in the slices with high SI tissues and less sparsity. These artefacts are incoherent and differ between BB and DB data. For the artefacts generated outside the subject in the DB data, their signals will have negative polarity after image subtraction. The negative polarity can only be restored by using the phase reference from DB data, which can provide the phase of the artefact signal. BB data does not contain the signal of those artefacts and can only provide phases of background noise, and therefore cannot suppress the artefacts.

Apart from the data source, the size of the phase correction region also has an influence on the performance of phase correction. The phase map obtained from a small central region of k -space from raw data can provide the background phase reference showing the slowly-varying phase variation related to hardware considerations. A more accurate phase estimate can be obtained by using a larger size for the phase correction region but is not helpful for phase correction. On the contrary, phase references with larger phase correction regions contain detailed phase variation related to anatomical tissues, which impair the precise correction of phases.

Applying the intensity correction procedure described in Chapter 4 can suppress the residual signal of background tissues. However, the linear regression needs to be performed on reconstructed individual BB and DB images and is difficult for k -space subtraction based methods. The fast convergence of the split-Bregman algorithm enables a fast partial CS reconstruction, so that intensity correction can be performed on the partially reconstructed images prior to the full reconstruction. Intensity correction can also potentially increase the data

sparsity and improve CS and PI reconstruction. In this study, the improvement in sparsity is not obvious in FBI due to the similar muscle SI on BB and DB data. Future work will evaluate the performance of KSPIC in other subtractive NCE-MRA techniques, such as DANTE-FSD, mentioned in Chapter 4, which shows significantly higher SI on BB images than DB images.

CE-MRI also involves image subtraction between the images acquired before and after the contrast injection. Previous studies have reported that complex subtraction in k -space has better performance than magnitude subtraction in both CE-MRA with PI acceleration¹⁷⁰ and dynamic CE-MRA without acceleration¹⁸⁰. KSPIC can be potentially applied to subtractive CE-MRA to further improve the reconstruction performance and allow greater AFs. Arterial spin labelling is another subtractive MRI technique used in both angiography and perfusion imaging, which can also be a potential implementation area of KSPIC.

Only femoral FBI on healthy volunteers was evaluated, which is a limitation of this study. Future work will assess acceleration based on KSPIC on patient data and evaluate if it can improve the diagnostic performance. The feasibility of KSPIC in other body areas will also be evaluated, such as calf, thorax and abdomen.

6.6 Conclusion

A new reconstruction method based on complex subtraction with intensity correction, KSPIC, was developed for highly accelerated femoral FBI in this chapter. It was compared with CMS, another advanced reconstruction method.

In respect of KSPIC the optimal size of the phase correction region was found to be 12–20 pixels in this study, neither too large nor too small. Acquiring the phase correction region from DB data rather than BB data improved the suppression of incoherent artefacts outside the subject. It was also noted that coil compression and adaptive combination can greatly reduce the computation time of CS reconstruction without obvious degradation of image quality. Adaptive combination outperformed the traditional RSS method, especially when using small virtual channel numbers.

Compared with conventional MS and KS reconstruction methods, KSPIC has the best reconstruction performance in the quantitative and qualitative measurements, permitting good image quality to be maintained up to higher AFs. In the prospective acceleration evaluation, KSPIC can accelerate the acquisition up to 20 times without significant decreases of subjective

quality scores in terms of vessel delineation, noise and artefacts and background signal contamination. KSPIC has the potential to further reduce the acquisition time of subtractive NCE-MRA techniques for clinical examinations.

Chapter 7. High-resolution fresh blood imaging with compressed sensing

7.1 Introduction

Spatial resolution is an important factor for MRA, as it is critical for the depiction of small vessels and the differentiation between fine grades of stenosis ³. Peripheral arteries have small branches with diameters less than one millimetre, which places particularly high demands on spatial resolution. An insufficient resolution would enhance partial volume effects, leading to underestimation of the blood signal and impaired visualisation of small vasculature and vessel boundaries ¹¹⁴. Moreover, peripheral MR angiography requires coverage of a large subject volume of interest, with at least 40 cm in the left-right direction and at least 80 cm to as much as 140 cm in the superior-inferior direction ¹⁸¹. The extended volume coverage requires high imaging efficiency so that multiple stations can be imaged in a short examination time, which constrains the matrix size and the spatial resolution.

The resolution in the phase-encoding direction(s) can be improved by acquiring more phase encodes, which, however, leads to increased acquisition times. Alternatively, angiograms can be acquired by using undersampling in the phase-encoding directions. Zenge *et. al.* combined PI using GRAPPA with a continuously-moving-table technique in 3D CE-MRA, and converted the reduction in acquisition time into an increase in spatial resolution in the phase-encoding directions ¹⁸¹. The technique provided a more detailed display of the peripheral arterial vessel system. Çukur *et. al.* developed a 3D magnetisation-prepared bSSFP sequence with improved resolution in phase-encoding directions and more frequent repetition of T₂-preparation ¹¹⁴. CS was implemented to improve imaging efficiency so that the acquisition time was not prolonged. The depiction of the vasculature was reported to be significantly improved.

As described in Chapters 5 and 6, CS, PI and PF undersampling can be combined together with the KSPIC reconstruction to substantially reduce the acquisition time of subtractive NCE-MRA without serious degradation of image quality. The time savings can be potentially used for improving spatial resolution in phase-encoding directions. Also, the resolution in the readout direction can be improved by increasing the readout gradient strength. For FBI, a stronger readout gradient can over-enhance the flow dephasing effect, leading to arterial signal loss even in the diastolic acquisition, but it can potentially be compensated by using flow compensation gradients ⁸⁰.

In this chapter, a high-resolution accelerated FBI technique is developed using the earlier results to acquire a femoral MRA examination with increased spatial resolution in the same acquisition time as a current standard-resolution examination. The acquisition matrix sizes in the readout and in-plane phase-encoding direction (x and y , coronal plane) were both increased from 256 to 512. Flow-compensation gradients in readout gradients with negative amplitudes were used for high-resolution acquisitions instead of flow-spoiled gradients. The amplitudes of spoiler gradients in the through-plane phase encoding direction (z) were increased to eliminate the residual stimulated echoes refocused by flow-compensation gradients. The resulting images with different resolutions were compared with standard-resolution images, both quantitatively and qualitatively.

7.2 Method

7.2.1 Sequence design of high-resolution FBI

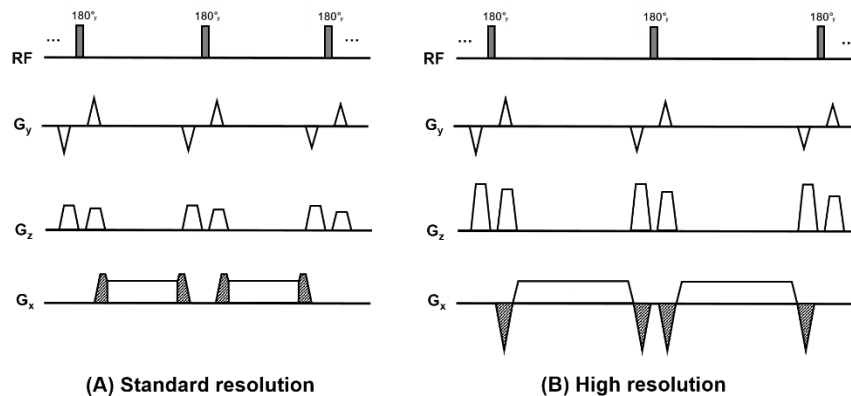


Figure 7.1 Diagrams of the 3D FBI sequence with the standard resolution (A) and increased high resolution (B). Positive flow-spoiled gradients are added along the readout axis in standard-resolution FBI, and negative flow-compensation gradients are added in high-resolution FBI (diagonal pattern). Phase-encoding gradients along the z -axis are combined with the spoiler gradients.

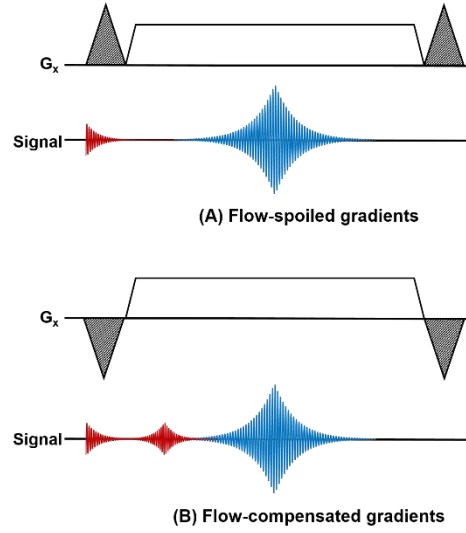


Figure 7.2 The timing of the FID signal and its refocused echo (red) and the primary spin echo (blue) relative to the readout gradient.

Figure 7.1 shows the diagrams of the 3D FBI sequence with the standard resolution and increased high resolution. Compared with standard-resolution FBI, three modifications were made to the high-resolution FBI:

a) Readout gradients with increased time duration

Firstly, due to the increased matrix size in the readout direction, the readout gradient needs to be increased in either its amplitude or duration. In this study, the time duration is increased, while the amplitude remains the same by retaining the same total bandwidth.

b) Partially flow-compensated readout gradients

Secondly, the dephasing effect might be over-enhanced by using stronger readout gradients, leading to arterial signal loss even in the (bright blood) diastolic acquisition. To balance the increased dephasing effect, partially flow-compensated readout gradients with negative amplitudes were used instead of positive flow-spoiled readout gradients. The total zero moment of the readout gradient is maintained the same for different resolutions. The strength of the flow-compensation/spoiled gradient is thus calculated as:

$$S_h = \frac{M_{std} (1 + S_{std}) - M_h}{M_h} \quad (7.1)$$

where M_{std} and M_h are the acquired matrix sizes of standard-resolution FBI and high-resolution FBI, and S_{std} and S_h are the strengths of the flow-spoiled/compensated gradients of standard-

resolution FBI and high-resolution FBI. The strength of gradients is defined as a percentage of one-half the area of the readout gradient ⁸⁰.

c) Increased spoiler gradients along the z-axis

Thirdly, when flip angles of the refocusing RF pulses are not exactly 180°, longitudinal magnetisation that regrows due to T₁ relaxation during the time period between the RF pulses will be converted to transverse magnetisation and create a free induction decay (FID) signal ¹⁸². As shown by Figure 7.2A, while sufficient flow-spoiler gradients can eliminate the FID signal (red), the flow-compensation gradients would generate a refocused echo (Figure 7.2B), leading to artefacts in the short T₁ tissues.

Spoiler gradients can also be added along the through-plane phase-encoding direction (z-axis) by combining them with the phase-encoding gradients. As shown in Figure 7.1, a spoiler gradient (z-spoiler) is placed after each refocusing RF pulse to eliminate the FID signal, and another gradient is placed before the next RF pulse for rephasing. The difference between the two gradients corresponds to the z-axis phase-encoding gradients. In this study, the strength of z-spoilers was set to 160% and 240% of one-half the area of the readout gradient for standard-resolution and high-resolution FSE respectively.

7.2.2 Subjects and imaging protocols

Seven healthy subjects (5 men and 2 women; age range 24–45 years) were imaged using a 1.5 T system (Discovery MR450; GE Healthcare, Waukesha, WI) and a 32 channel cardiac array coil. Studies were approved by the local research ethics committee, and all participants gave informed consent.

Each subject underwent five 3D femoral artery FBI acquisitions with matrix sizes (*x* and *y* dimensions) of 256×256, 320×320, 384×384, 448×448 and 512×512. The FOV (*x* and *y* dimensions) was 42 cm for all acquisitions, yielding resolutions of 1.64×1.64, 1.31×1.31, 1.09×1.09, 0.94×0.94 and 0.82×0.82 mm² respectively. The corresponding flow-spoiled/compensated gradient strengths were 20%, −24%, −54%, −74% and −90%. The echo spacing increased from 4.5 ms to 6.7 ms for different resolutions. The matrix size, FOV and resolution in the *z* dimension were 80, 14.4 cm and 1.8 mm in all the acquisitions. Other parameters include receiver bandwidth: ±83.3 kHz; ETL: 58–70, TE_{eff}: 45 ms, TR: 2 or 3 heartbeats; inversion time for STIR fat suppression: 174 ms. The readout direction was set to be the superior-inferior direction. To reduce the refocused FID signal, the refocusing flip angles

were constant at 180° for both systolic and diastolic acquisitions, without using the adaptive refocus technique. Flow suppression is mainly achieved by flow-spoiled gradients (or large readout gradients) in this study.

The acquisitions were accelerated by PI, CS and PF and reconstructed by KSPIC as described in Chapter 6. The total number of k -space samples was 2000, corresponding to total AFs of 8.0, 10.1, 12.1, 14.1, 16.1 for the acquisitions with resolutions from 256 to 512 respectively. The acquisition times were thus kept the same over the different resolutions acquired for each subject. The acquisition times varied between different subjects (132–258 heartbeats, 3.5–4.5 minutes) because the heart-rate, number of heartbeats per TR and ETL were different for each subject.

7.2.3 Image evaluation

MIPs of the images with different resolutions were assessed by two experienced radiologists, in a randomised order for each subject. The radiologists were blinded to image resolution. The images were graded in terms of the large vessel delineation and small vessel delineation with the criteria as follows:

Large Vessel delineation

- 1=severe signal loss in large vessels and non-diagnostic delineation
- 2=moderate signal loss in large vessels and impaired depictions of large vessels
- 3=slight signal loss at the centre of the vessels
- 4=excellent depictions with high signal intensity

Small Vessel delineation

- 1=severe loss of small branches
- 2=moderate loss of small branches and blurred boundaries
- 3=slight loss of small branches and impaired definitions of the fine structures
- 4=excellent display with sharp boundaries and clear definitions of fine structures

In addition, CNR of artery-to-background (without reference images) and sharpness assessment described in Chapter 3 were used as objective and quantitative indices to evaluate the angiograms with different resolutions. Wilcoxon signed-rank tests and paired Student's t -tests were performed respectively to detect differences in subjective image quality scores and quantitative measurements between the standard-resolution images and high-resolution images. Statistical significance was defined at $P < 0.05$ in all tests.

7.3 Results

7.3.1 Example images

Example MIPs with zoomed-in views from two healthy volunteers are demonstrated in Figure 7.3. As denoted by the yellow arrowheads, high-resolution FBI improved the delineation of small arterial branches, providing sharp boundaries and clear definition of fine structures. In comparison, loss of small branches and impaired definition of the fine structures can be observed on standard-resolution images. Images with the resolution from 256 to 448 all show good visualisations of large arteries, but slight signal loss in the centre of large arteries can be observed on the images with a resolution of 512.

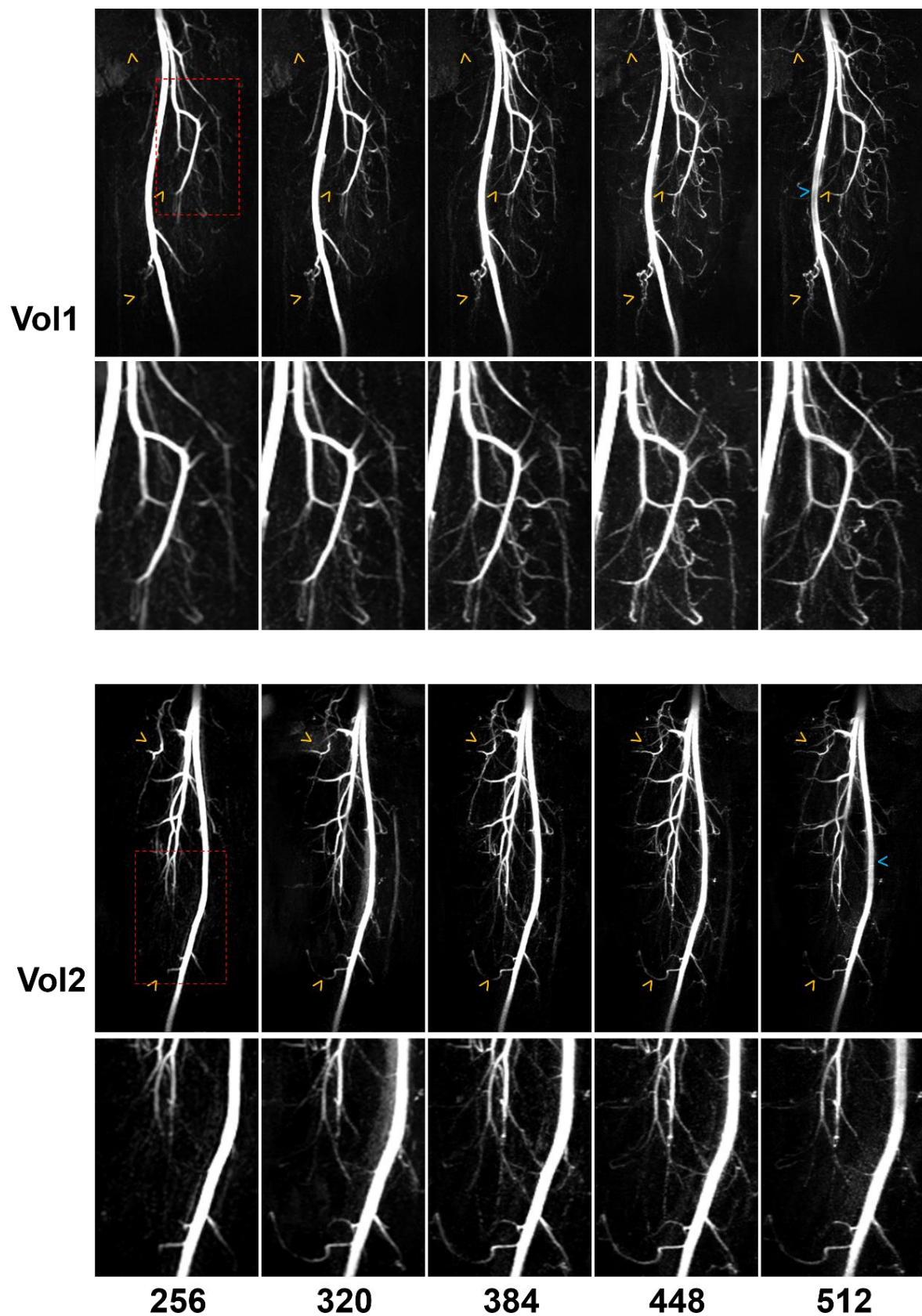


Figure 7.3 Example MIP images with different resolutions from two healthy volunteers. For each volunteer, the upper row shows the capture of one leg, and the lower row shows the zoomed-in views of

small branches in the red dashed box in the upper row images. The acquired matrix sizes are the same in x and y dimensions, increasing from 256 to 512. The size in the z -direction are the same value (80) across different acquisitions. The yellow arrowheads denote the improved depiction of small arterial branches, and the blue arrowheads denote the slight signal loss in the large artery on the image with very high resolution (512×512).

7.3.2 Quantitative evaluation

Figure 7.4 shows the subjective image quality scoring results. For the delineation of large vessels, no significant differences were detected between the images with the standard-resolution and the images with different high resolutions. The delineation of small vessels was improved by increasing the image resolution. Significant differences exist between the standard-resolution images and high-resolution images with all increased matrix sizes except for 512×512.

Objective evaluation results are shown in Figure 7.5. While sharpness was significantly improved in all the high-resolution acquisitions, CNR of artery-to-background significantly decreased with increasing resolution.

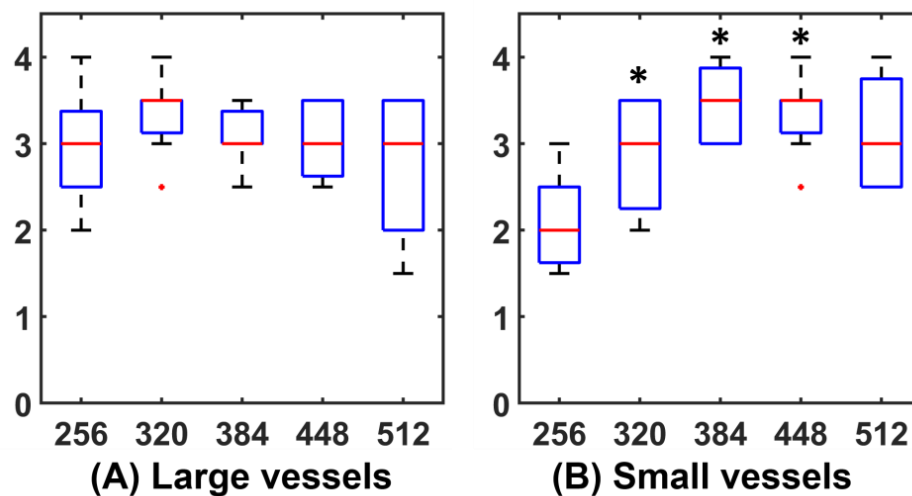


Figure 7.4 Box-plots of the subjective quality scores of FBI images with different resolutions in terms of the large vessel delineations (A) and small vessel delineations (B). The matrix sizes are the same in the x and y dimensions, increasing from 256 to 512. * denotes statistical significance between the high-resolution images and the standard-resolution images (256×256). (Wilcoxon signed-rank tests, $P < 0.05$).

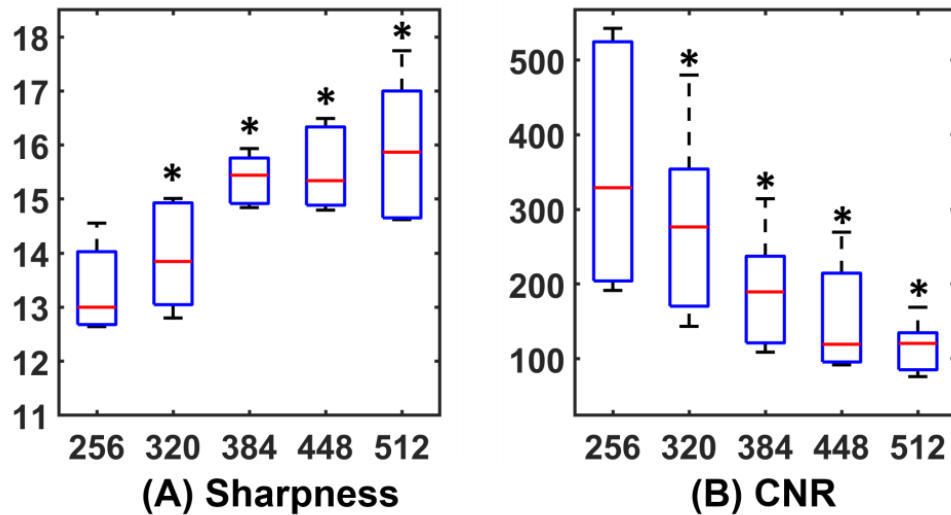


Figure 7.5 Box-plots of objective evaluation results of FBI images with different resolutions in terms of sharpness (A) and CNR of artery-to-background (B). The matrix sizes are the same in x and y dimensions, increasing from 256 to 512. * denotes statistical significance between the high-resolution images and the standard-resolution images (256×256). (paired t -tests, $P < 0.05$).

7.3.3 Effect of flow-compensation/spoiled gradients

Without our changes to flow-spoiled/compensation gradients, the increased readout gradient area would lead to an over-enhanced flow dephasing effect, causing arterial signal loss. Figure 7.6(A) shows an example of high-resolution FBI using a matrix size of 512×512×80 without flow-compensation gradients but with flow-spoiled gradients (strength +20%). Signal loss can be observed in the centre of arteries. The excessive flow dephasing can be compensated by introducing flow-compensation gradients (strength −60%) (Figure 7.6(B)).

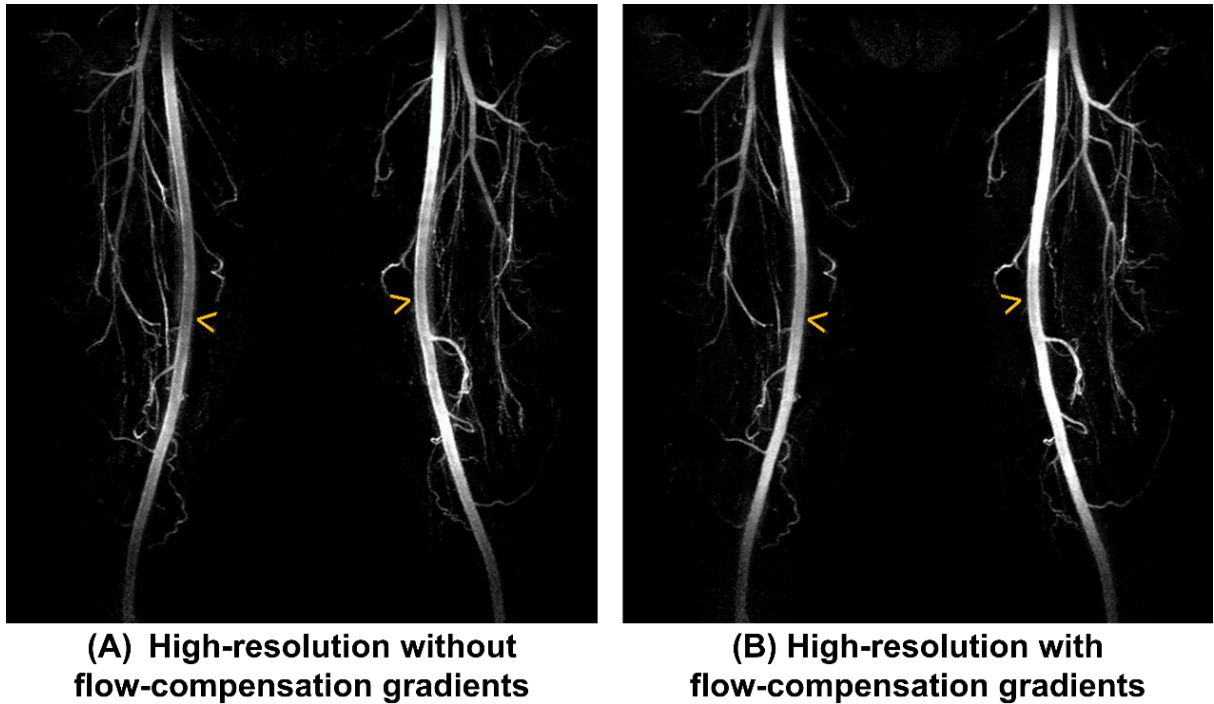


Figure 7.6 Importance of flow-compensation gradients in high-resolution FBI. A: A MIP of the high-resolution image without flow-compensation gradients (with flow-spoiled gradients, +20% of $\frac{1}{2}$ readout gradient area). B: A MIP of high-resolution images with flow-compensation gradients (-60% of $\frac{1}{2}$ readout gradient area). The matrix size for A and B is $512 \times 512 \times 80$. The yellow arrowheads denote arterial signal loss on A, which can be improved by flow-compensation gradients (B).

7.3.4 Effect of z -spoiler

Figure 7.7 shows the ripple-shaped artefacts on a high-resolution unsubtracted source image (384×384) acquired using the same z -spoiler as standard-resolution FBI (Figure 7.7A). The z -spoiler strength of 160% was not enough to suppress the refocused echo generated by the flow-compensation gradients. The artefacts almost disappear when increasing the z -spoiler strength to 240% (Figure 7.7B).

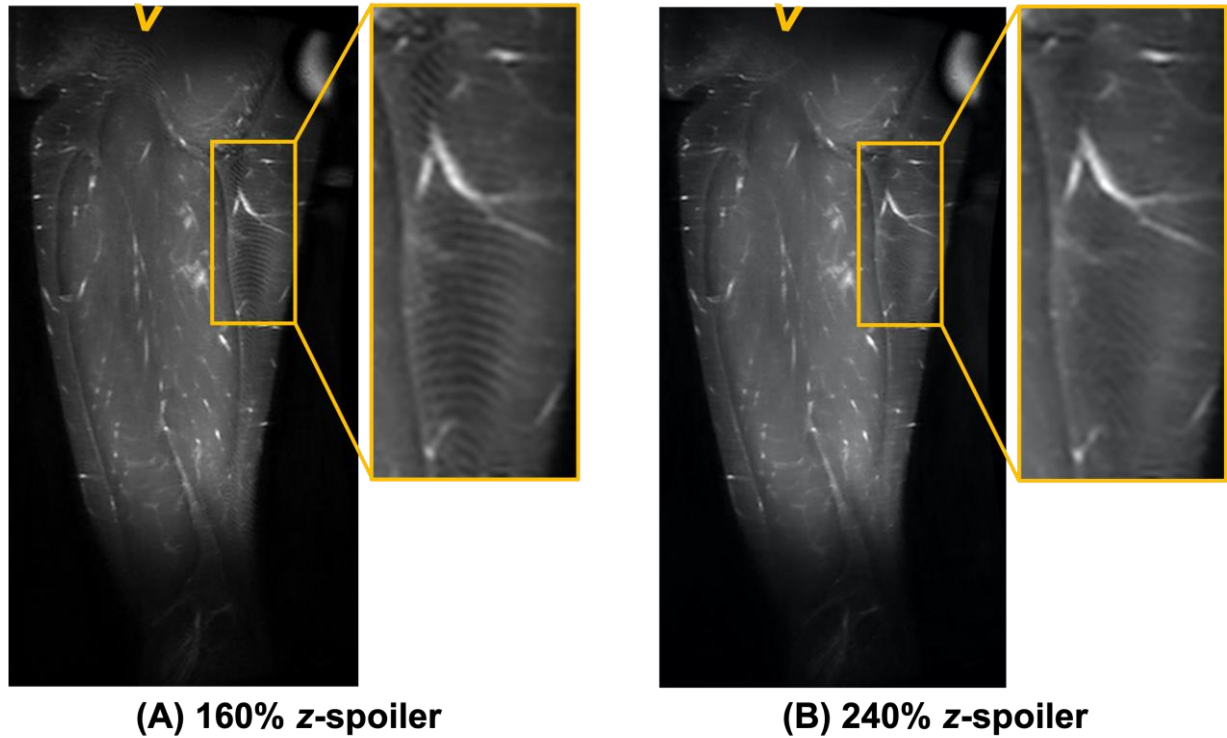


Figure 7.7 Artefacts on high-resolution unsubtracted single-slice source images (bright-artery) with a matrix size of $384 \times 384 \times 80$. A: High-resolution FBI using a z -spoiler with the strength of 160%, which is same as used for standard-resolution FBI. B: High-resolution FBI using a z -spoiler with an increased strength of 240%. The yellow arrowheads and zoomed-in views denote the ripple-shaped artefacts due to refocused FID echoes generated by the flow-compensation gradients.

7.4 Discussion

This study proposes a high-resolution 3D FBI approach, which increases the matrix sizes in both the readout (x) and in-plane phase-encoding (y) directions from 256 to larger values up to 512. The potentially increased acquisition time caused by the increased number of phase-encoding steps is compensated by employing the acceleration technique introduced in Chapters 5 and 6. This allows the higher resolution images to be obtained without increasing the overall acquisition time. The enhanced flow-dephasing effect is compensated by flow-compensation gradients using negative amplitudes.

The improved resolution can reduce partial volume effects and improve visualisation of the small vasculature. The quality evaluation results demonstrated that high-resolution FBI significantly improved the image sharpness and the delineation of small arterial branches. On the other hand, the small voxel sizes lead to lower signal-to-noise ratio (SNR). The CNR of

artery-to-background measured in this study decreased with increasing the matrix size. Although no significant difference was detected in the scores for the delineation of large vessels, slight central arterial signal loss could be found in several cases when the matrix size was increased to 512×512 . Moreover, a matrix size of 512×512 did not result in improved small vessel delineation compared with other matrix sizes. Therefore, matrix sizes between 320 and 448 are more appropriate for high-resolution 3D FBI in practice.

Although the refocusing flip angles were set to 180° for both systolic and diastolic acquisitions in this study, the actual flip angle was not accurate and varied across the body due to a non-uniform B_1^+ transmit field. The regrown longitudinal magnetisation is partially converted to the transverse plane by the refocusing RF pulses, and then dephased and refocused by the bipolar readout gradients (negative flow-compensation gradients plus positive readout gradients). The centre of the refocused echo does not locate in the centre of the k -space, unless the strength of the flow-compensation gradients is exactly -100% . The regrown longitudinal magnetisation is strongest for tissues with short T_1 relaxation times, such as fat. Therefore, as shown in Figure 7.7, ripple-shaped artefacts can be observed in fat regions on the high-resolution source images. The refocused echoes can be eliminated by using strong spoiler gradients in phase-encoding axes. In this study, the strength of the z -spoiler, which is also employed by standard FBI sequences, was increased from 160% to 240%. The main femoral arteries should be little influenced by the increased z -spoiler gradients since their principal flow direction is along the readout direction. However, increased z -spoiler gradients may affect the visualisation of the arterial branches flowing along the direction of z -spoiler (anterior-posterior), which will be investigated in future studies.

Increasing the acquired matrix size requires larger readout gradient areas, which can be achieved by increasing either the duration or the amplitude of the gradient. Increasing its duration causes a larger echo spacing, leading to a stronger T_2 -blurring effect in the phase-encoding directions. Increasing its amplitude does not change the echo spacing but would increase the receiver bandwidth, leading to the reduction of SNR. Considering the SNR has already been degraded by reducing the voxel size, we kept the amplitude unchanged and only increased the duration. The influence of increasing the duration and amplitude will be investigated and compared in our future work.

The resolution in the z (slice) direction was not evaluated in this study. A matrix size of 80 in z direction was used for all the acquisitions with different matrix sizes in x and y directions.

Although the resolution in the z direction might have less influence on the coronal MIP, increasing it may potentially further reduce partial volume effect and improve the artery visualisation in the anterior-posterior dimension. Also, the resolution increases in the readout and phase-encoding directions are achieved by different mechanisms—one by increasing the readout gradient area and another by increasing the number of acquired views—and should be investigated separately since they potentially have differing impacts on the image quality. Future work will evaluate the influence of increasing resolutions in different dimensions and explore each optimal resolution respectively.

As in Chapter 6, this study only involves femoral FBI datasets on healthy volunteers. Future work will assess the technique over the whole leg and acquire more datasets for assessment. Patient studies will also be needed to evaluate the diagnostic performance of high-resolution FBI.

7.5 Conclusion

A time efficient high-resolution 3D FBI MRA technique was developed in this chapter. Compared with standard-resolution FBI, high-resolution FBI significantly improved the delineation of small arterial branches and image sharpness at the cost of reducing CNR of artery-to-background. No significant difference was observed in the evaluation of the delineation of large arteries between high-resolution and standard-resolution acquisitions. The matrix sizes of 320×320 , 384×384 and 448×448 in x and y dimensions have the best overall performance. Increasing the matrix size to 512×512 did not further improve the delineation of small vessels but did further decrease the CNR and caused slight signal loss in the centre of large arteries for some subjects. This technique has the potential to improve image quality and diagnostic performance of peripheral MRA, but further investigations over the rest of the leg and in patient examinations are needed.

Chapter 8. Final remarks and future work

8.1 Summary

This thesis focuses on the improvement of subtractive NCE-MRA techniques, particularly in terms of imaging acceleration. The contributions of the thesis include:

- A reconstruction algorithm for solving the L1-SPIRiT problem was proposed in Section 3.4.3, which combines the Split-Bregman algorithm with POCS iterations.
- An automatic sharpness evaluation method was proposed in Section 3.5.4.
- An intensity correction method based on robust regression was proposed in Chapter 4, which improved background suppression of subtractive NCE-MRA techniques. Compared with simple regression methods such as OLS, it achieved more accurate and robust performance across the range of different NCE-MRA methods.
- A variable density Poisson-disk sampling pattern was designed for 3D MRI undersampling in Chapter 5. The influence of key parameters in sampling pattern designed was evaluated, and optimal sampling patterns for the 3D accelerated femoral artery FBI sequence were determined.
- In Chapter 6, a highly accelerated FBI pulse sequence using self-designed patterns was developed on GE's EPIC programming platform. A new reconstruction method based on k -space subtraction, KSPIC, was developed for accelerated subtractive NCE-MRA. The intensity correction method proposed in Chapter 4, together with a phase correction procedure, were incorporated in the reconstruction. Compared with conventional reconstruction methods, KSPIC has the best reconstruction performance in both the quantitative and qualitative measurements, enabling large acceleration factors and reduced examination times.
- Chapter 7 proposed a time-efficient high-resolution FBI technique. A highly accelerated FBI pulse sequence with high-resolution, partially flow-compensated readout gradients and large spoiler gradients was developed. KSPIC was used for undersampling reconstruction. Compared with standard-resolution FBI using the same examination times, it significantly improved the delineation of small arterial branches and image sharpness.

8.2 Limitations and future work

8.2.1 Patient examinations

One limitation of the studies in this thesis is the lack of patient examinations. Although the intensity correction method in Chapter 4 involved thoracic and iliac NCE-MRA patient data, the acceleration related studies in Chapter 5, 6 and 7 were only tested on healthy volunteers. Patient studies are needed in future work to evaluate the diagnostic performance of the proposed acceleration and high-resolution techniques.

8.2.2 Application in other body areas

The acceleration and high-resolution techniques were only implemented in femoral MRA. One whole leg FBI-MRA examination was performed with two stations to cover both thigh and calf. The high-resolution imaging method described in Chapter 7 was used. The matrix sizes for the two stations were both $352 \times 352 \times 80$. Imaging was accelerated by an AF of 11. The acquisition time for the FBI sequence of each station is around 4 minutes. Full evaluation of whole leg examinations is needed in future work.



Figure 8.1 High resolution whole leg examination with two stations (matrix size: 352×352×80).

Compared with other body areas, it is easier for patients to keep legs still during the examination of lower extremity MRA. Therefore, femoral MRA is less likely to be affected by motion-related problems. Future work could assess the performance of KSPIC in thoracic and abdominal MRA, where imaging speed is more crucial due to the presence of physiological motion related to respiration, the heart and gastro-intestinal tract. Breath-holding can prevent respiratory motion artefacts, but requires very rapid imaging which limits the achievable resolution and volumetric coverage. Another approach is to use either respiratory bellows or navigator signals to monitor the respiratory motion and to acquire data only at a specific respiratory state. However, gated data acquisition further reduces time-efficiency. The implementation of KSPIC could potentially reduce acquisition times for thoracic and abdominal MRA and improve image quality by suppressing motion-related artefacts and possibly increasing spatial resolution.

8.2.3 Application in other subtractive imaging techniques

The techniques developed in this thesis mostly focused on FBI. As described in Section 6.5, the acceleration and high-resolution techniques can be potentially applied to other imaging techniques involving image subtraction, such as FSD-MRA, CE-MRA and ASL for both MRA and perfusion imaging.

In addition to suppressing background signals, the intensity correction procedure in KSPIC can increase the sparsity of subtracted data. For example, in thoracic DANTE, the SI differences of background tissues between BBIs and DBIs are larger and more extensive. As evaluated in Chapter 4, the SIs of muscle and liver on DBIs are only 69.1% and 33.6% of that on BBIs.

8.2.4 Future direction of CS

Compressed sensing MRI techniques have been developed rapidly since they were proposed in 2007. A large number of studies have been carried out, which have proved the feasibility of reducing acquisition times for the examinations of different body areas and using different sequences. The translation of these methods into routine clinical practice has been in progress. Some CS accelerated protocols, such as CS-3D TOF and CS-3D FBI, are becoming available as commercial products from MR vendors.

The application of sparsity in MRI can go beyond pure acceleration of image acquisition in future research. Apart from increasing spatial resolution as described in Chapter 7, highly

accelerated imaging can be combined with continuous data acquisition to enhance information content and achieve previously inaccessible imaging performance ⁸⁷. For example, recent studies in developing retrospectively motion correction methods based on continuous data acquisition and CS reconstruction are of particular interest. By using the navigator signal, these methods extract groups of data (bins) with different motion states and then weight them differently ^{183,184} or correct the motion-corrupted data ^{185–187} in the reconstruction process. The processed data bins can be combined into a final result in a single motion state, or be reconstructed respectively to generate an image set with an extra motion-state dimension ¹⁸⁸. The techniques developed in this thesis can potentially be combined with these advanced motion-corrected/resolved techniques to improve free-breathing imaging techniques, especially for subtractive NCE-MRA.

8.2.5 Future direction of FBI

As discussed in Chapter 2, FBI has several drawbacks, which limit its wide clinical implementation. Apart from the time-efficiency and background suppression problem addressed in this thesis, image degradation caused by imperfect triggering is another important problem. FBI requires the systolic and diastolic data to be acquired in optimal cardiac phases, which is particularly difficult for patients with abnormal blood flow patterns or cardiac arrhythmia.

A potential future direction is to develop FBI techniques with a larger tolerance of acquisition triggering. Recently, a technique called ROMANCE-MRA was proposed, which generated robust angiograms even in the presence of cardiac arrhythmia ⁶⁷. Similar to the motion-resolved techniques, ROMANCE-MRA continuously acquires data over all cardiac phases, which is then sorted into multiple bins retrospectively, and reconstructs time-resolved angiograms with different cardiac phases. Reconstruction of each undersampled bin based on CS is an important part of this technique. Further development of multi-phase techniques could be one of the developing directions of FBI in future studies.

8.3 Conclusion

The work in this thesis has demonstrated the feasibility of highly accelerated subtractive NCE-MRA in lower extremities. A new reconstruction method based on complex subtraction, together with an intensity correction method, was developed to improve current subtractive NCE-MRA techniques in terms of background suppression, imaging speed and spatial

resolution. These developments can potentially help improve and make more practical non-invasive MR examinations for patients with vascular disease.

References

1. Barth M, Moser E. Proton NMR relaxation times of human blood samples at 1.5 T and implications for functional MRI. *Cell Mol Biol (Noisy-le-grand)*. 1997;43(5):783-791.
2. Varatorn R. Atlas of Vascular Anatomy An Angiographic Approach. *Bangkok Med J*. 2015;09(01):92-92. doi:10.31524/bkkmedj.2015.02.020
3. Miyazaki M, Lee VS. Nonenhanced MR Angiography. *Radiology*. 2008;248(1):20-43. doi:10.1148/radiol.2481071497
4. Kanda T, Nakamura E, Moritani T, Yamori Y. Arterial pulse wave velocity and risk factors for peripheral vascular disease. *Eur J Appl Physiol*. 2000;82(1-2):1-7. doi:10.1007/s004210050644
5. Rose SC. Noninvasive vascular laboratory for evaluation of peripheral arterial occlusive disease: Part II--clinical applications: chronic, usually atherosclerotic, lower extremity ischemia. *J Vasc Interv Radiol*. 2000;11(10):1257-1275. doi:10.1016/S1051-0443(07)61300-1
6. Toursarkissian B, Mejia A, Smilanich RP, Schoolfield J, Shireman PK, Sykes MT. Noninvasive Localization of Infrainguinal Arterial Occlusive Disease in Diabetics. *Ann Vasc Surg*. 2001;15(1):73-78. doi:10.1007/s100160010003
7. Varghese SS. Numerical Modeling of Pulsatile Turbulent Flow in Stenotic Vessels. *J Biomech Eng*. 2003;125(4):445. doi:10.1115/1.1589774
8. Jung EM, Kubale R, Ritter G, Gallegos MT, Jungius KP, Rupp N C DA. Diagnostics and characterisation of preocclusive stenoses and occlusions of the internal carotid artery with B-flow. *Eur Radiol*. 2007;17(2):439-447.
9. Cimminiello C. PAD: Epidemiology and pathophysiology. *Thromb Res*. 2002;106(6):V295-V301. doi:10.1016/S0049-3848(01)00400-5
10. Abdulhannan P, Russell DA, Homer-Vanniasinkam S. Peripheral arterial disease: A literature review. *Br Med Bull*. 2012;104(1):21-39. doi:10.1093/bmb/lds027
11. Hardman RL, Jazaeri O, Yi J, Smith M, Gupta R. Overview of classification systems in peripheral artery disease. *Semin Intervent Radiol*. 2014;31(4):378-388. doi:10.1055/s-0034-1393976
12. Norgren L, Hiatt WR, Dormandy JA, Nehler MR, Harris KA, Fowkes FGR. Inter-Society Consensus for the Management of Peripheral Arterial Disease (TASC II). *J Vasc Surg*. 2007;45(1):S5-S67. doi:10.1016/j.jvs.2006.12.037
13. Selvin E, Erlinger TP. Prevalence of and risk factors for peripheral arterial disease in the United States: Results from the National Health and Nutrition Examination Survey, 1999-2000. *Circulation*. 2004;110(6):738-743. doi:10.1161/01.CIR.0000137913.26087.F0
14. Prince MR. Gadolinium-enhanced MR aortography. *Radiology*. 1994;191(1):155-164. doi:10.1148/radiology.191.1.8134563
15. Hartung MP, Grist TM, François CJ. Magnetic resonance angiography: current status and future directions. *J Cardiovasc Magn Reson*. 2011;13(1):19. doi:10.1186/1532-429X-13-19
16. Hennig J, Scheffler K, Laubenberger J, Strecker R. Time-resolved projection

- angiography after bolus injection of contrast agent. *Magn Reson Med*. 1997;37(3):341-345. doi:10.1002/mrm.1910370306
17. Markl M, Hennig J. Phase contrast MRI with improved temporal resolution by view sharing: k-space related velocity mapping properties. *Magn Reson Imaging*. 2001;19(5):669-676. doi:10.1016/S0730-725X(01)00386-1
 18. Korosec FR, Frayne R, Grist TM, Mistretta CA. Time-resolved contrast-enhanced 3D MR angiography. *Magn Reson Med*. 1996;36(3):345-351. doi:10.1002/mrm.1910360304
 19. Saranathan M, Rettmann DW, Hargreaves BA, Clarke SE, Vasanawala SS. Differential Subsampling with Cartesian Ordering (DISCO): a high spatio-temporal resolution Dixon imaging sequence for multiphasic contrast enhanced abdominal imaging. *J Magn Reson Imaging*. 2012;35(6):1484-1492. doi:10.1002/jmri.23602
 20. Willinek WA, Hadizadeh DR, von Falkenhausen M, et al. 4D time-resolved MR angiography with keyhole (4D-TRAK): More than 60 times accelerated MRA using a combination of CENTRA, keyhole, and SENSE at 3.0T. *J Magn Reson Imaging*. 2008;27(6):1455-1460. doi:10.1002/jmri.21354
 21. Marckmann P. Nephrogenic Systemic Fibrosis: Suspected Causative Role of Gadodiamide Used for Contrast-Enhanced Magnetic Resonance Imaging. *J Am Soc Nephrol*. 2006;17(9):2359-2362. doi:10.1681/ASN.2006060601
 22. Kanda T, Ishii K, Kawaguchi H, Kitajima K, Takenaka D. High signal intensity in the dentate nucleus and globus pallidus on unenhanced T1-weighted MR images: relationship with increasing cumulative dose of a gadolinium-based contrast material. *Radiology*. 2014;270(3):834-841. doi:10.1148/radiol.13131669
 23. Errante Y, Cirimele V, Mallio CA, Di Lazzaro V, Zobel BB, Quattrocchi CC. Progressive Increase of T1 Signal Intensity of the Dentate Nucleus on Unenhanced Magnetic Resonance Images Is Associated With Cumulative Doses of Intravenously Administered Gadodiamide in Patients With Normal Renal Function, Suggesting Dechelation. *Invest Radiol*. 2014;49(10):685-690. doi:10.1097/RLI.0000000000000072
 24. Quattrocchi CC, Mallio CA, Errante Y, et al. Gadodiamide and Dentate Nucleus T1 Hyperintensity in Patients With Meningioma Evaluated by Multiple Follow-Up Contrast-Enhanced Magnetic Resonance Examinations With No Systemic Interval Therapy. *Invest Radiol*. 2015;50(7):470-472. doi:10.1097/RLI.0000000000000154
 25. Kanda T, Fukusato T, Matsuda M, et al. Gadolinium-based Contrast Agent Accumulates in the Brain Even in Subjects without Severe Renal Dysfunction: Evaluation of Autopsy Brain Specimens with Inductively Coupled Plasma Mass Spectroscopy. *Radiology*. 2015;276(1):228-232. doi:10.1148/radiol.2015142690
 26. McDonald RJ, McDonald JS, Kallmes DF, et al. Intracranial Gadolinium Deposition after Contrast-enhanced MR Imaging. *Radiology*. 2015;275(3):772-782. doi:10.1148/radiol.15150025
 27. Lenkinski RE. Gadolinium Deposition and Retention in the Brain: Should We Be Concerned? *Radiol Cardiothorac Imaging*. 2019;1(3):e190104. doi:10.1148/ryct.2019190104
 28. Gulani V, Calamante F, Shellock FG, Kanal E, Reeder SB. Gadolinium deposition in the brain: summary of evidence and recommendations. *Lancet Neurol*. 2017;16(7):564-570. doi:10.1016/S1474-4422(17)30158-8

29. Administration USF and D. FDA warns that gadolinium- based contrast agents (GBCAs) are retained in the body; requires new class warnings. <https://www.fda.gov/downloads/Drugs/DrugSafety/UCM589442.pdf>.
30. Agency EM. Gadolinium-containing contrast agents. EMA's final opinion confirms restrictions on use of linear gadolinium agents in body scans. https://www.ema.europa.eu/docs/en_GB/document_library/Referrals_document/gadolinium_contrast_agents_31/Opinion_provided_by_Committee_for_Medicinal_Products_for_Human_Use/WC500231824.pdf.
31. Ghoshhajra B, Engel L-C, Walker TG. MR Angiography. In: *Magnetic Resonance Angiography: Basics to Future*. InTechOpen; 2012:23-38. doi:10.5772/47751.hancement
32. Stepansky F, Hecht EM, Rivera R, et al. Dynamic MR Angiography of Upper Extremity Vascular Disease: Pictorial Review. *RadioGraphics*. 2008;28(1):e28-e28. doi:10.1148/radiol.e28
33. Koktzoglou I, Lim RP, Oisin F, Edelman RR. Non-contrast Enhanced MRA. In: *Basic Principles of Cardiovascular MRI: Physics and Imaging Technique*. ; 2015:1-338. doi:10.1007/978-3-319-22141-0
34. Ray JG, Vermeulen MJ, Bharatha A, Montanera WJ, Park AL. Association between MRI exposure during pregnancy and fetal and childhood outcomes. *JAMA - J Am Med Assoc*. 2016. doi:10.1001/jama.2016.12126
35. Masaryk TJ, Modic MT, Ruggieri PM, et al. Three-dimensional (volume) gradient-echo imaging of the carotid bifurcation: preliminary clinical experience. *Radiology*. 1989;171(3):801-806. doi:10.1148/radiology.171.3.2717755
36. Masaryk TJ, Laub GA, Modic MT, Ross JS, Haacke EM. Carotid-CNS MR flow imaging. *Magn Reson Med*. 1990;14(2):308-314. doi:10.1002/mrm.1910140215
37. Laub GA. Time-of-flight method of MR angiography. *Magn Reson Imaging Clin N Am*. 1995;3:391-398.
38. Lohan DG, Saleh R, Nael K, Krishnam M, Finn JP. Contrast-enhanced MRA versus nonenhanced MRA: Pros and cons. *Appl Radiol*. 2007;36(5 SUPPL.):3-15.
39. Heiserman JE, Drayer BP, Fram EK, et al. Carotid artery stenosis: Clinical efficacy of two-dimensional time-of-flight MR angiography. *Radiology*. 1992;182(3):761-768. doi:10.1148/radiology.182.3.1535891
40. McCauley TR, Monib A, Dickey KW, et al. Peripheral vascular occlusive disease: accuracy and reliability of time-of-flight MR angiography. *Radiology*. 1994;192(2):351-357. doi:10.1148/radiology.192.2.8029396
41. Atkinson D, Brant-Zawadzki M, Gillan G, Purdy D, Laub G. Improved MR angiography: magnetization transfer suppression with variable flip angle excitation and increased resolution. *Radiology*. 1994;190(3):890-894. doi:10.1148/radiology.190.3.8115646
42. Blatter DD, Parker DL, Ahn SS, et al. Cerebral MR angiography with multiple overlapping thin slab acquisition. Part II. Early clinical experience. *Radiology*. 1992;183(2):379-389. doi:10.1148/radiology.183.2.1561338
43. Parker DL, Yuan C, Blatter DD. MR angiography by multiple thin slab 3D acquisition. *Magn Reson Med*. 1991;17(2):434-451. doi:10.1002/mrm.1910170215
44. Hutter J. Accelerated Non-contrast-enhanced Morphological and Functional Magnetic

Resonance Angiography. Doctoral dissertation. *Friedrich-Alexander-Universität Erlangen-nürnberg*. 2014. <http://www5.informatik.uni-erlangen.de/Forschung/Publikationen/2014/Hutter14-ANC.pdf>.

45. Katoh M, Buecker A, Stuber M, Günther RW, Spuentrup E. Free-breathing renal MR angiography with steady-state free-precession (SSFP) and slab-selective spin inversion: Initial results. *Kidney Int*. 2004;66(3):1272-1278. doi:10.1111/j.1523-1755.2004.00882.x
46. Edelman RR, Sheehan JJ, Dunkle E, Schindler N, Carr J, Koktzoglou I. Quiescent-interval single-shot unenhanced magnetic resonance angiography of peripheral vascular disease: Technical considerations and clinical feasibility. *Magn Reson Med*. 2010;63(4):951-958. doi:10.1002/mrm.22287
47. Edelman RR, Siewert B, Adamis M, Gaa J, Laub G, Wielopolski P. Signal targeting with alternating radiofrequency (STAR) sequences: Application to MR angiography. *Magn Reson Med*. 1994;31(2):233-238. doi:10.1002/mrm.1910310219
48. Kim SG. Quantification of Relative Cerebral Blood-Flow Change by Flow-Sensitive Alternating Inversion-Recovery (FAIR) Technique - Application to Functional Mapping. *Magn Reson Med*. 1995;34(3):293-301. doi:DOI 10.1002/mrm.1910340303
49. Koktzoglou I, Edelman RR. STAR and STARFIRE for flow-dependent and flow-independent noncontrast carotid angiography. *Magn Reson Med*. 2009;61(1):117-124. doi:10.1002/mrm.21769
50. Edelman RR, Chen Q. EPISTAR MRI: multislice mapping of cerebral blood flow. *Magn Reson Med*. 1998;40(6):800-805. doi:10.1002/mrm.1910400603
51. Dumoulin CL, Souza SP, Walker MF, Wagle W. Three-dimensional phase contrast angiography. *Magn Reson Med*. 1989;9(1):139-149. doi:10.1002/mrm.1910090117
52. Hausmann R, Lewin JS, Laub G. Phase-contrast MR angiography with reduced acquisition time: new concepts in sequence design. *J Magn Reson Imaging*. 1991;1(4):415-422. doi:10.1002/jmri.1880010405
53. Wheaton AJ, Miyazaki M. Non-contrast enhanced MR angiography: Physical principles. *J Magn Reson Imaging*. 2012;36(2):286-304. doi:10.1002/jmri.23641
54. Markl M, Kilner PJ, Ebbers T, et al. Comprehensive 4D velocity mapping of the heart and great vessels by cardiovascular magnetic resonance. *J Cardiovasc Magn Reson*. 2011;13(1):7. doi:10.1186/1532-429X-13-7
55. Markl M, Wallis W, Brendecke S, Simon J, Frydrychowicz A, Harloff A. Estimation of global aortic pulse wave velocity by flow-sensitive 4D MRI. *Magn Reson Med*. 2010;63(6):1575-1582. doi:10.1002/mrm.22353
56. Harloff A, Nußbaumer A, Bauer S, et al. In vivo assessment of wall shear stress in the atherosclerotic aorta using flow-sensitive 4D MRI. *Magn Reson Med*. 2010;63(6):1529-1536. doi:10.1002/mrm.22383
57. Harloff A, Simon J, Brendecke S, et al. Complex plaques in the proximal descending aorta: An underestimated embolic source of stroke. *Stroke*. 2010;41(6):1145-1150. doi:10.1161/STROKEAHA.109.577775
58. Fan Z, Hodnett PA, Davarpanah AH, et al. 3D Noncontrast MR Angiography of the Distal Lower Extremities Using Flow-Sensitive Dephasing (FSD)- Prepared Balanced SSFP.

Invest Radiol. 2011;46(8):515-523. doi:10.1097/RLI.0b013e318217daee

59. Priest AN, Graves MJ, Lomas DJ. Non-contrast-enhanced vascular magnetic resonance imaging using flow-dependent preparation with subtraction. *Magn Reson Med.* 2012;67(3):628-637. doi:10.1002/mrm.23040
60. Priest AN, Taviani V, Graves MJ, Lomas DJ. Improved artery-vein separation with acceleration-dependent preparation for non-contrast-enhanced magnetic resonance angiography. *Magn Reson Med.* 2014;72(3):699-706. doi:10.1002/mrm.24981
61. Wedeen VJ, Meuli R a, Edelman RR, et al. Projective imaging of pulsatile flow with magnetic resonance. *Science.* 1985;230(4728):946-948. doi:10.1126/science.4059917
62. Meuli RA, Wedeen VJ, Geller SC, et al. MR gated subtraction angiography: evaluation of lower extremities. *Radiology.* 1986;159(2):411-418. doi:10.1148/radiology.159.2.3961174
63. Priest AN, Mortensen KH, Lomas DJ. Comparison of DANTE- and iMSDE-based methods for subtractive NCE-MRA of the central thoracic vein. In: *Proceedings of the 23rd Annual Meeting of ISMRM, Toronto, Canada.* ; 2015:2662.
64. Liu X, Fan Z, Zhang N, et al. Unenhanced MR Angiography of the Foot: Initial Experience of Using Flow-Sensitive Dephasing-prepared Steady-State Free Precession in Patients with Diabetes. *Radiology.* 2014;272(3):885-894. doi:10.1148/radiol.14132284
65. Sheehan JJ, Fan Z, Davarpanah AH, et al. Nonenhanced MR Angiography of the Hand with Flow-Sensitive Dephasing-prepared Balanced SSFP Sequence: Initial Experience with Systemic Sclerosis. *Radiology.* 2011;259(1):248-256. doi:10.1148/radiol.10100851
66. Priest AN, Low G, Graves MJ, Lomas DJ. Non-contrast-enhanced MR angiography of the thoracic central veins. In: *Proceedings of the Joint Annual Meeting ISMRM-ESMRMB, Milan, Italy.* ; 2014:5597.
67. Kim H, Park S, Kim EY, Park J. Retrospective multi-phase non-contrast-enhanced magnetic resonance angiography (ROMANCE MRA) for robust angiogram separation in the presence of cardiac arrhythmia. *Magn Reson Med.* 2018;80(3):976-989. doi:10.1002/mrm.27099
68. Li H, Wang S, Priest AN, Graves MJ, Lomas DJ. An optimised subtraction approach for subtractive NCE-MRA techniques based on principal component analysis. In: *Proceedings of the Joint Annual Meeting ISMRM-ESMRMB, Paris, France.* ; 2018:922.
69. Li H, Wang S, Priest AN, Graves MJ, Lomas DJ. Background tissue suppression for subtractive NCE-MRA techniques based on robust regression using the deviation angle. In: *Proceedings of the 27th Annual Meeting of ISMRM, Montreal, Canada.* ; 2019:2094.
70. Shin T, Woters PW, Hu BS, Nishimura DG. Non-contrast-enhanced renal and abdominal MR angiography using velocity-selective inversion preparation. *Magn Reson Med.* 2013;69(5):1268-1275. doi:10.1002/mrm.24356
71. Shin T, Kligerman SJ, Crawford RS, Rajagopalan S, Gullapalli RP. Noncontrast-enhanced peripheral venography using velocity-selective magnetization preparation and transient balanced SSFP. *Magn Reson Med.* 2016;75(2):653-664. doi:10.1002/mrm.25623
72. Fuchs F, Laub G, Othomo K. TrueFISP - Technical considerations and cardiovascular

- applications. *Eur J Radiol.* 2003;46(1):28-32. doi:10.1016/S0720-048X(02)00330-3
73. Miyazaki M, Isoda H. Non-contrast-enhanced MR angiography of the abdomen. *Eur J Radiol.* 2011;80(1):9-23. doi:10.1016/j.ejrad.2011.01.093
 74. Brittain JH, Olcott EW, Szuba A, et al. Three-dimensional flow-independent peripheral angiography. *Magn Reson Med.* 1997;38(3):343-354. doi:10.1002/mrm.1910380302
 75. Brittain JH, Hu BS, Wright GA, Meyer CH, Macovski A, Nishimura DG. Coronary Angiography with Magnetization-Prepared T2 Contrast. *Magn Reson Med.* 1995;33(5):689-696. doi:10.1002/mrm.1910330515
 76. Stafford RB, Sabati M, Mahallati H, Frayne R. 3D non-contrast-enhanced MR angiography with balanced steady-state free precession dixon method. *Magn Reson Med.* 2008;59(2):430-433. doi:10.1002/mrm.21479
 77. Edelman RR, Koktzoglou I. Unenhanced flow-independent MR venography by using signal targeting alternative radiofrequency and flow-independent relaxation enhancement. *Radiology.* 2009;250(1):236-245. doi:10.1148/radiol.2493080496
 78. Fan Z, Sheehan J, Bi X, Liu X, Carr J, Li D. 3D noncontrast MR angiography of the distal lower extremities using flow-sensitive dephasing (FSD)-prepared balanced SSFP. *Magn Reson Med.* 2009;62(6):1523-1532. doi:10.1002/mrm.22142
 79. Miyazaki M, Sugiura S, Tateishi F, Wada H, Kassai Y, Abe H. Non-contrast-enhanced MR angiography using 3D ECG-synchronized half-Fourier fast spin echo. *J Magn Reson Imaging.* 2000;12(5):776-783. <http://www.ncbi.nlm.nih.gov/pubmed/11050650>.
 80. Miyazaki M, Takai H, Sugiura S, Wada H, Kuwahara R, Urata J. Peripheral MR angiography: separation of arteries from veins with flow-spoiled gradient pulses in electrocardiography-triggered three-dimensional half-Fourier fast spin-echo imaging. *Radiology.* 2003;227(3):890-896. doi:10.1148/radiol.2273020227
 81. Storey P, Atanasova IP, Lim RP, et al. Tailoring the flow sensitivity of fast spin-echo sequences for noncontrast peripheral MR angiography. *Magn Reson Med.* 2010;64(4):1098-1108. doi:10.1002/mrm.22510
 82. Urata J, Miyazaki M, Wada H, Nakaura T, Yamashita Y, Takahashi M. Clinical evaluation of aortic diseases using nonenhanced MRA with ECG-triggered 3D half-fourier FSE. *J Magn Reson Imaging.* 2001;14(2):113-119. doi:10.1002/jmri.1160
 83. Doi H, Ono A, Kawai A, et al. Magnetic resonance angiography without contrast enhancement medium in bone and soft tissue tumors. *Oncol Rep.* 2006;15(3):681-685.
 84. Ono, A., Miyazaki, M., Takata, S., Nakai, M., Takeishi, A., Kuriyama, M., ... & Ikeda M. Evaluation of arterial occlusive diseases in lower extremity using non-contrast-enhanced MR arteriography with ECG triggered 3D half-Fourier FSE: initial experience at 0.5 T. In: *Proceedings of the 21st Annual Meeting of ISMRM, Toronto, Canada.* ; 2003:1713.
 85. Ono A, Murase K, Taniguchi T, et al. Deep vein thrombosis using noncontrast-enhanced MR venography with electrocardiographically gated three - Dimensional half-fourier FSE: Preliminary experience. *Magn Reson Med.* 2009;61(4):907-917. doi:10.1002/mrm.21924
 86. Ono A, Murase K, Taniguchi T, et al. Deep venous thrombosis: Diagnostic value of non-contrast-enhanced MR venography using electrocardiography-triggered three-dimensional half-Fourier FSE. *Magn Reson Med.* 2010;64(1):88-97.

doi:10.1002/mrm.22374

87. Feng L, Benkert T, Block KT, Sodickson DK, Otazo R, Chandarana H. Compressed sensing for body MRI. *J Magn Reson Imaging*. 2017;45(4):966-987. doi:10.1002/jmri.25547
88. Yang ASC, Kretzler M, Sudarski S, Gulani V, Seiberlich N. Sparse reconstruction techniques in magnetic resonance imaging. *Invest Radiol*. 2016;51(6):349-364. doi:10.1097/RLI.0000000000000274
89. Jaspán ON, Fleysher R, Lipton ML. Compressed sensing MRI: a review of the clinical literature. *Br J Radiol*. 2015;88(1056):20150487. doi:10.1259/bjr.20150487
90. Lustig MS. Sparse MRI, Doctoral dissertation. *Stanford Univ*. 2008.
91. Hennig J, Nauerth A, Friedburg H. RARE imaging: a fast imaging method for clinical MR. *Magn Reson Med*. 1986;3(6):823-833. doi:10.1002/mrm.1910030602
92. Frahm J, Haase A, Matthaei D. Rapid NMR imaging of dynamic processes using the FLASH technique. *Magn Reson Med*. 1986;3(2):321-327. doi:10.1002/mrm.1910030217
93. Mansfield P. Real-time echo-planar imaging by NMR. *Br Med Bull*. 1984;40(2):187-190. doi:10.1093/oxfordjournals.bmb.a071970
94. Margosian PM, Seiberlich N, Takizawa M. Exploitation of Sparsity in MRI. In: *EMagRes*. Chichester, UK: John Wiley & Sons, Ltd; 1996:289-306. doi:10.1002/9780470034590.emrstm1308
95. Schmitt F. The gradient system. Understanding gradients from an EM perspective:(gradient linearity, eddy currents, maxwell terms & peripheral nerve stimulation). In: *Proceedings of the 21st Annual Meeting of ISMRM, Salt Lake City, USA*. ; 2013:7379.
96. Storey P, Otazo R, Lim RP, et al. Exploiting sparsity to accelerate noncontrast MR angiography in the context of parallel imaging. *Magn Reson Med*. 2012;67(5):1391-1400. doi:10.1002/mrm.23132
97. Jung H, Sung K, Nayak KS, Kim EY, Ye JC. k-t FOCUSS: A general compressed sensing framework for high resolution dynamic MRI. *Magn Reson Med*. 2009;61(1):103-116. doi:10.1002/mrm.21757
98. Tsao J, Boesiger P, Pruessmann KP. k-t BLAST and k-t SENSE: Dynamic MRI With High Frame Rate Exploiting Spatiotemporal Correlations. *Magn Reson Med*. 2003;50(5):1031-1042. doi:10.1002/mrm.10611
99. Pedersen H, Kozerke S, Ringgaard S, Nehrke K, Won YK. K-t PCA: Temporally constrained k-t BLAST reconstruction using principal component analysis. *Magn Reson Med*. 2009;62(3):706-716. doi:10.1002/mrm.22052
100. Liang D, DiBella EVR, Chen RR, Ying L. K-t ISD: Dynamic cardiac MR imaging using compressed sensing with iterative support detection. *Magn Reson Med*. 2012;68(1):41-53. doi:10.1002/mrm.23197
101. Lustig M, Donoho D, Pauly JM. Sparse MRI: The application of compressed sensing for rapid MR imaging. *Magn Reson Med*. 2007;58(6):1182-1195. doi:10.1002/mrm.21391
102. Rapacchi S, Han F, Natsuaki Y, et al. High spatial and temporal resolution dynamic contrast-enhanced magnetic resonance angiography using compressed sensing with

- magnitude image subtraction. *Magn Reson Med.* 2014;71(5):1771-1783. doi:10.1002/mrm.24842
103. Rapacchi S, Natsuaki Y, Plotnik A, et al. Reducing view-sharing using compressed sensing in time-resolved contrast-enhanced magnetic resonance angiography. *Magn Reson Med.* 2015;74(2):474-481. doi:10.1002/mrm.25414
 104. Trzasko JD, Haider CR, Borisch EA, et al. Sparse-CAPR: Highly accelerated 4D CE-MRA with parallel imaging and nonconvex compressive sensing. *Magn Reson Med.* 2011;66(4):1019-1032. doi:10.1002/mrm.22892
 105. Fushimi Y, Fujimoto K, Okada T, et al. Compressed Sensing 3-Dimensional Time-of-Flight Magnetic Resonance Angiography for Cerebral Aneurysms. *Invest Radiol.* 2016;51(4):228-235. doi:10.1097/RLI.0000000000000226
 106. Hutter J, Grimm R, Forman C, Hornegger J, Schmitt P. Highly undersampled peripheral Time-of-Flight magnetic resonance angiography: optimized data acquisition and iterative image reconstruction. *Magn Reson Mater Physics, Biol Med.* 2015;28(5):437-446. doi:10.1007/s10334-014-0477-9
 107. Li B, Li H, Dong L, Huang G. Fast carotid artery MR angiography with compressed sensing based three-dimensional time-of-flight sequence. *Magn Reson Imaging.* 2017;43:129-135. doi:10.1016/j.mri.2017.07.017
 108. Milles J, Versluis MJ, Webb AG, Reiber JHC. Quantitative evaluation of Compressed Sensing in MRI: Application to 7T time-of-flight angiography. In: *Proceedings of the 10th IEEE International Conference on Information Technology and Applications in Biomedicine.* IEEE; 2010:1-4. doi:10.1109/ITAB.2010.5687775
 109. Fushimi Y, Okada T, Kikuchi T, et al. Clinical evaluation of time-of-flight MR angiography with sparse undersampling and iterative reconstruction for cerebral aneurysms. *NMR Biomed.* 2017;30(11):1-9. doi:10.1002/nbm.3774
 110. Yamamoto T, Okada T, Fushimi Y, et al. Magnetic resonance angiography with compressed sensing: An evaluation of moyamoya disease. Meckel S, ed. *PLoS One.* 2018;13(1):e0189493. doi:10.1371/journal.pone.0189493
 111. Tao Y, Rilling G, Davies M, Marshall I. Carotid blood flow measurement accelerated by compressed sensing: Validation in healthy volunteers. *Magn Reson Imaging.* 2013;31(9):1485-1491. doi:10.1016/j.mri.2013.05.009
 112. Hsiao A, Lustig M, Alley MT, Murphy MJ, Vasanawala SS. Evaluation of valvular insufficiency and shunts with parallel-imaging compressed-sensing 4D phase-contrast MR imaging with stereoscopic 3D velocity-fusion volume-rendered visualization. *Radiology.* 2012;265(1):87-95. doi:10.1148/radiol.12120055
 113. Dyvorne H, Knight-Greenfield A, Jajamovich G, et al. Abdominal 4D Flow MR Imaging in a Breath Hold: Combination of Spiral Sampling and Dynamic Compressed Sensing for Highly Accelerated Acquisition. *Radiology.* 2015;275(1):245-254. doi:10.1148/radiol.14140973
 114. Çukur T, Lustig M, Nishimura DG. Improving non-contrast-enhanced steady-state free precession angiography with compressed sensing. *Magn Reson Med.* 2009;61(5):1122-1131. doi:10.1002/mrm.21907
 115. Zhou Z, Han F, Yu S, et al. Accelerated noncontrast-enhanced 4-dimensional intracranial MR angiography using golden-angle stack-of-stars trajectory and compressed sensing

- with magnitude subtraction. *Magn Reson Med.* 2018;79(2):867-878. doi:10.1002/mrm.26747
116. Candès EJ, Romberg J, Tao T. Robust uncertainty principles: Exact signal reconstruction from highly incomplete frequency information. *IEEE Trans Inf Theory.* 2006;52(2):489-509. doi:10.1109/TIT.2005.862083
 117. Donoho DL. Compressed sensing. *IEEE Trans Inf Theory.* 2006;52(4):1289-1306. doi:10.1109/TIT.2006.871582
 118. Lustig M, Donoho DL, Santos JM, Pauly JM. Compressed Sensing MRI. *IEEE Signal Process Mag.* 2008;25(2):72-82. doi:10.1109/MSP.2007.914728
 119. Knoll F, Bredies K, Pock T, Stollberger R. Second order total generalized variation (TGV) for MRI. *Magn Reson Med.* 2011;65(2):480-491. doi:10.1002/mrm.22595
 120. Guo W, Yin W. EdgeCS: edge guided compressive sensing reconstruction. In: Frossard P, Li H, Wu F, Girod B, Li S, Wei G, eds. *Visual Communications and Image Processing 2010.* ; 2010:77440L. doi:10.1117/12.863354
 121. Feng L, Benkert T, Block KT, Sodickson DK, Otazo R, Chandarana H. Compressed sensing for body MRI. *J Magn Reson Imaging.* 2017;45(4):966-987. doi:10.1002/jmri.25547
 122. Cook RL. Stochastic sampling in computer graphics. *ACM Trans Graph.* 1986;5(1):51-72. doi:10.1145/7529.8927
 123. McCool M, Fiume E. Hierarchical Poisson disk sampling distributions. *Proc - Graph Interface.* 1992:94-105.
 124. Stephen B, Vandenberghe L. *Convex Optimization.* Cambridge University Press; 2004.
 125. Kim SJ, Koh K, Lustig M, Boyd S. An efficient method for compressed sensing. In: *Proceedings - International Conference on Image Processing, ICIP.* ; 2006:Vol. 3, 111-117. doi:10.1109/ICIP.2007.4379260
 126. Goldstein T, Osher S. The Split Bregman Method for L1-Regularized Problems. *SIAM J Imaging Sci.* 2009;2(2):323-343. doi:10.1137/080725891
 127. Osher S, Burger M, Goldfarb D, Xu J, Yin W. An iterative regularization method for total variation-based image restoration. *Multiscale Model Simul.* 2005;4(2):460-489. doi:10.1137/040605412
 128. Bregman LM. The relaxation method of finding the common point of convex sets and its application to the solution of problems in convex programming. *USSR Comput Math Math Phys.* 1967;7(3):200-217. doi:10.1016/0041-5553(67)90040-7
 129. Yin W, Osher S, Goldfarb D, Darbon J. Bregman iterative algorithms for l1-minimization with applications to compressed sensing. *SIAM J Imaging Sci.* 2008;1(1):143-168. doi:10.1137/070703983
 130. Cai J-F, Osher S, Shen Z. Linearized Bregman iterations for compressed sensing. *Math Comput.* 2009;78(267):1515-1536. doi:10.1090/s0025-5718-08-02189-3
 131. Yin W, Osher S, Goldfarb D, Darbon J. Bregman iterative algorithms for ℓ_1 -minimization with applications to compressed sensing. *SIAM J Imaging Sci.* 2008. doi:10.1137/070703983
 132. Liu F, Duan Y, Peterson BS, Kangarlu A. Compressed sensing MRI combined with

SENSE in partial k -space. *Phys Med Biol*. 2012;57(21):N391-N403. doi:10.1088/0031-9155/57/21/N391

133. Sodickson DK, Manning WJ. Simultaneous acquisition of spatial harmonics (SMASH): Fast imaging with radiofrequency coil arrays. *Magn Reson Med*. 1997;38(4):591-603. doi:10.1002/mrm.1910380414
134. Pruessmann KP, Weiger M, Scheidegger MB, Boesiger P. SENSE: Sensitivity encoding for fast MRI. *Magn Reson Med*. 1999;42(5):952-962. doi:10.1002/(SICI)1522-2594(199911)42:5<952::AID-MRM16>3.0.CO;2-S
135. Shin PJ, Larson PEZ, Ohliger MA, et al. Calibrationless parallel imaging reconstruction based on structured low-rank matrix completion. *Magn Reson Med*. 2014;72(4):959-970. doi:10.1002/mrm.24997
136. Griswold MA, Jakob PM, Heidemann RM, et al. Generalized Autocalibrating Partially Parallel Acquisitions (GRAPPA). *Magn Reson Med*. 2002;47(6):1202-1210. doi:10.1002/mrm.10171
137. Beatty P, Brau A, Chang S. A method for autocalibrating 2-D accelerated volumetric parallel imaging with clinically practical reconstruction times. In: *Proceedings of the 15th Annual Meeting of ISMRM, Berlin, Germany*. Vol 15. ; 2007:1749. <http://cds.ismrm.org/ismrm-2007/files/01749.pdf>.
138. Jakob PM, Grisowld MA, Edelman RR, Sodickson DK. AUTO-SMASH: A self-calibrating technique for SMASH imaging. *Magma Magn Reson Mater Physics, Biol Med*. 1998;7(1):42-54. doi:10.1007/BF02592256
139. Lustig M, Pauly JM. SPIRiT: Iterative self-consistent parallel imaging reconstruction from arbitrary k-space. *Magn Reson Med*. 2010;64(2):457-471. doi:10.1002/mrm.22428
140. Lustig M, Alley M, Vasanawala S, Donoho D, Pauly J. L1 SPIR-iT: Autocalibrating Parallel Imaging Compressed Sensing. In: *Proceedings 17th Scientific Meeting, International Society for Magnetic Resonance in Medicine*. Vol Honolulu. ; 2009:379. /MyPathway2009/0379.
141. Noll DC, Nishimura DG, Macovski A. Homodyne Detection in Magnetic Resonance Imaging. *IEEE Trans Med Imaging*. 1991;10(2):154-163. doi:10.1109/42.79473
142. Kustner T, Wurslin C, Gatidis S, et al. MR Image Reconstruction Using a Combination of Compressed Sensing and Partial Fourier Acquisition: ESPReSSo. *IEEE Trans Med Imaging*. 2016;35(11):2447-2458. doi:10.1109/TMI.2016.2577642
143. Wang Z, Bovik AC, Sheikh HR, Simoncelli EP. Image quality assessment: From error visibility to structural similarity. In: *IEEE Transactions on Image Processing*. Vol 13. ; 2004:600-612. doi:10.1109/TIP.2003.819861
144. Horé A, Ziou D. Image quality metrics: PSNR vs. SSIM. In: *Proceedings - International Conference on Pattern Recognition*. ; 2010:2366-2369. doi:10.1109/ICPR.2010.579
145. Akasaka T, Fujimoto K, Yamamoto T, et al. Optimization of regularization parameters in compressed sensing of magnetic resonance angiography: Can statistical image metrics mimic radiologists' perception? *PLoS One*. 2016;11(1):1-14. doi:10.1371/journal.pone.0146548
146. Ahmad R, Ding Y, Simonetti OP. Edge sharpness assessment by parametric modeling: Application to magnetic resonance imaging. *Concepts Magn Reson Part A*.

2015;44(3):138-149. doi:10.1002/cmr.a.21339

147. Atherton TJ, Kerbyson DJ. Size invariant circle detection. *Image Vis Comput.* 1999;17(11):795-803. doi:10.1016/s0262-8856(98)00160-7
148. Coleman TF, Li Y. An interior trust region approach for nonlinear minimization subject to bounds. *SIAM J Optim.* 1996;6(2):418-445. doi:10.1137/0806023
149. Li H, Priest AN, Patterson I, Graves MJ, Lomas DJ. Subtractive non-contrast-enhanced MRI of lower limb veins using multiple flow-dependent preparation strategies. *Magn Reson Med.* 2019;81(3):1769-1783. doi:10.1002/mrm.27530
150. Lindley MD, Kim D, Morrell G, Heilbrun ME, Hanrahan CJ, Lee VS. Fat Saturation Improves Fresh Blood Imaging of Peripheral Vessels in the Calf Station. In: *Proceedings of the 23rd Annual Meeting of ISMRM, Toronto, Canada.* ; 2015:4512.
151. Atanasova IP, Kim D, Storey P, Rosenkrantz AB, Lim RP, Lee VS. Sagittal fresh blood imaging with interleaved acquisition of systolic and diastolic data for improved robustness to motion. *Magn Reson Med.* 2013;69(2):321-328. doi:10.1002/mrm.24576
152. Hoey ETD, Ganeshan A, Puni R, Henderson J, Crowe PM. Fresh blood imaging of the peripheral vasculature: An emerging unenhanced MR technique. *Am J Roentgenol.* 2010;195(6):1444-1448. doi:10.2214/AJR.09.4184
153. Foo TKF, Ho VB, Marcos HB, Hood MN, Choyke PL. MR angiography using steady-state free precession. *Magn Reson Med.* 2002;48(4):699-706. doi:10.1002/mrm.10278
154. Kimura T, Ikedo M, Takemoto S. Hybrid of opposite-contrast MR angiography (HOP-MRA) combining time-of-flight and flow-sensitive black-blood contrasts. *Magn Reson Med.* 2009;62(2):450-458. doi:10.1002/mrm.22021
155. Ye Y, Hu J, Wu D, Haacke EM. Noncontrast-enhanced magnetic resonance angiography and venography imaging with enhanced angiography. *J Magn Reson Imaging.* 2013;38(6):1539-1548. doi:10.1002/jmri.24128
156. Welsch RE. Robust regression using iteratively reweighted least-squares. *Commun Stat - Theory Methods.* 1977;6(9):813-827. doi:10.1080/03610927708827533
157. Rousseeuw PJ, Croux C. Alternatives to the Median Absolute Deviation. *J Am Stat Assoc.* 1993;88(424):1273-1283. doi:10.1080/01621459.1993.10476408
158. Priest AN, Murphy IG, Lomas DJ. Non-contrast-enhanced MRA using Velocity-sensitised , Acceleration-sensitised and Combined Sensitisation with Fast-Spin-Echo Readout. In: *Proceedings of the 24th Annual Meeting of ISMRM, Singapore.* ; 2016:2554.
159. Li L, Miller KL, Jezzard P. DANTE-prepared pulse trains: A novel approach to motion-sensitized and motion-suppressed quantitative magnetic resonance imaging. *Magn Reson Med.* 2012;68(5):1423-1438. doi:10.1002/mrm.24142
160. Morita S, Kojima S, Hirata M, et al. Unenhanced ECG-gated fast spin-echo MR digital subtraction angiography (MRDSA) using short echo-spacing three-dimensional sequence of femoral arteries: Initial experience. *J Magn Reson Imaging.* 2011;34(1):157-164. doi:10.1002/jmri.22595
161. Li H, Priest AN, Graves MJ, Lomas DJ. Highly Accelerated NCE-MRA Using Complex Subtraction with Intensity Correction: Improved Reconstruction Accuracy and Background Tissue Suppression. In: *Proceedings of the 27th Annual Meeting of ISMRM, Montreal, Canada.* ; 2019:2067.

162. Xu Y, Mark Haacke E. Partial fourier imaging in multi-dimensions: A means to save a full factor of two in time. *J Magn Reson Imaging*. 2001;14(5):628-635. doi:10.1002/jmri.1228
163. Lustig M, Donoho D, Pauly JM. Sparse MRI: The application of compressed sensing for rapid MR imaging. *Magn Reson Med*. 2007;58(6):1182-1195. doi:10.1002/mrm.21391
164. Zijlstra F, Viergever MA, Seevinck PR. Evaluation of variable density and data-driven K-space undersampling for compressed sensing magnetic resonance imaging. *Invest Radiol*. 2016;51(6):410-419. doi:10.1097/RLI.0000000000000231
165. Mitchell SA, Rand A, Ebeida MS, Bajaj C. Variable radii poisson-disk sampling. In: *Proceedings of the 24th Canadian Conference on Computational Geometry, CCCG 2012*. ; 2012:185-190.
166. Knoll F, Clason C, Diwoky C, Stollberger R. Adapted random sampling patterns for accelerated MRI. *Magn Reson Mater Physics, Biol Med*. 2011;24(1):43-50. doi:10.1007/s10334-010-0234-7
167. Vellagoundar J, Machireddy RR. A robust adaptive sampling method for faster acquisition of MR images. *Magn Reson Imaging*. 2015;33(5):635-643. doi:10.1016/j.mri.2015.01.008
168. Zhang Y, Peterson BS, Ji G, Dong Z. Energy Preserved Sampling for Compressed Sensing MRI. *Comput Math Methods Med*. 2014;2014:1-12. doi:10.1155/2014/546814
169. Gözcü B, Mahabadi RK, Li YH, et al. Learning-Based Compressive MRI. *IEEE Trans Med Imaging*. 2018. doi:10.1109/TMI.2018.2832540
170. Koktzoglou I, Sheehan JJ, Dunkle EE, Breuer FA, Edelman RR. Highly accelerated contrast-enhanced MR angiography: Improved reconstruction accuracy and reduced noise amplification with complex subtraction. *Magn Reson Med*. 2010;64(6):1843-1848. doi:10.1002/mrm.22567
171. Li H, Priest AN, Graves MJ, Lomas DJ. Highly accelerated NCE-MRA: Phase correction to remove background artefacts for complex subtraction. In: *Proceedings of the 27th Annual Meeting of ISMRM, Montreal, Canada*. ; 2019:2066.
172. Park HW, Cho MH, Cho ZH. Real-value representation in inversion-recovery NMR imaging by use of a phase-correction method. *Magn Reson Med*. 1986;3(1):15-23. doi:10.1002/mrm.1910030104
173. Gowland PA, Leach MO. A simple method for the restoration of signal polarity in multi-image inversion recovery sequences for measuring T1. *Magn Reson Med*. 1991;18(1):224-231. doi:10.1002/mrm.1910180123
174. Noll DC, Nishimura DG, Macovski A. Homodyne detection in magnetic resonance imaging. *IEEE Trans Med Imaging*. 1991;10(2):154-163. doi:10.1109/42.79473
175. Kellman P, Arai AE, Mcveigh ER, Aletras AH. Phase-Sensitive Inversion Recovery for Detecting Myocardial Infarction Using Gadolinium-Delayed Hyperenhancement. 2002;383:372-383. doi:10.1002/mrm.10051
176. Park HW, Cho MH, Cho ZH. Real-value representation in inversion-recovery NMR imaging by use of a phase-correction method. *Magn Reson Med*. 1986;3(1):15-23. doi:10.1002/mrm.1910030104
177. Zhang T, Pauly JM, Vasanawala SS, Lustig M. Coil compression for accelerated imaging

- with Cartesian sampling. *Magn Reson Med.* 2013;69(2):571-582. doi:10.1002/mrm.24267
178. Walsh DO, Gmitro AF, Marcellin MW. Adaptive reconstruction of phased array MR imagery. *Magn Reson Med.* 2000;43(5):682-690. doi:10.1002/(SICI)1522-2594(200005)43:5<682::AID-MRM10>3.0.CO;2-G
 179. Gowland PA, Leach MO. A simple method for the restoration of signal polarity in multi-image inversion recovery sequences for measuring T1. *Magn Reson Med.* 1991;18(1):224-231. doi:10.1002/mrm.1910180123
 180. Naganawa S, Ito T, Iwayama E, et al. Magnitude subtraction vs. complex subtraction in dynamic contrast-enhanced 3D-MR angiography: basic experiments and clinical evaluation. *J Magn Reson Imaging.* 1999;10(5):813-820. doi:10.1002/(sici)1522-2586(199911)10:5<813::aid-jmri28>3.0.co;2-5
 181. Zenge MO, Vogt FM, Brauck K, et al. High-resolution continuously acquired peripheral MR angiography featuring partial parallel imaging GRAPPA. *Magn Reson Med.* 2006;56(4):859-865. doi:10.1002/mrm.21033
 182. Mugler JP. Optimized three-dimensional fast-spin-echo MRI. *J Magn Reson Imaging.* 2014;39(4):745-767. doi:10.1002/jmri.24542
 183. Zhang T, Cheng JY, Potnick AG, et al. Fast pediatric 3D free-breathing abdominal dynamic contrast enhanced MRI with high spatiotemporal resolution. *J Magn Reson Imaging.* 2015;41(2):460-473. doi:10.1002/jmri.24551
 184. Johnson KM, Block WF, Reeder SB, Samsonov A. Improved least squares MR image reconstruction using estimates of k-Space data consistency. *Magn Reson Med.* 2012;67(6):1600-1608. doi:10.1002/mrm.23144
 185. Bhat H, Ge L, Nielles-Vallespin S, Zuehlsdorff S, Li D. 3D radial sampling and 3D affine transform-based respiratory motion correction technique for free-breathing whole-heart coronary MRA with 100% imaging efficiency. *Magn Reson Med.* 2011;65(5):1269-1277. doi:10.1002/mrm.22717
 186. Piccini D, Littmann A, Nielles-Vallespin S, Zenge MO. Respiratory self-navigation for whole-heart bright-blood coronary MRI: Methods for robust isolation and automatic segmentation of the blood pool. *Magn Reson Med.* 2012;68(2):571-579. doi:10.1002/mrm.23247
 187. Usman M, Atkinson D, Odille F, et al. Motion corrected compressed sensing for free-breathing dynamic cardiac MRI. *Magn Reson Med.* 2013;70(2):504-516. doi:10.1002/mrm.24463
 188. Feng L, Axel L, Chandarana H, Block KT, Sodickson DK, Otazo R. XD-GRASP: Golden-angle radial MRI with reconstruction of extra motion-state dimensions using compressed sensing. *Magn Reson Med.* 2016;75(2):775-788. doi:10.1002/mrm.25665